OCCURRENCE AND CAUSES OF F-REGION ECHOES FOR THE CANADIAN POLARDARN/SUPERDARN RADARS

A Thesis Submitted to the College of

Graduate Studies and Research

in Partial Fulfillment of the Requirements

for the Degree of Master of Science

in the Department of Physics and Engineering Physics

University of Saskatchewan

Saskatoon

By

Mohsen Ghezelbash

PERMISSION TO USE

In presenting this thesis in partial fulfillment of the requirements for a Post-graduate degree from the University of Saskatchewan, I agree that the Libraries of this University may make it freely available for inspection. I further agree that permission for copying of this thesis in any manner, in whole or in part, for scholarly purposes may be granted by the professor or professors who supervised my thesis work or, in their absence, by the Head of the Department or the Dean of the College in which my thesis work was done. It is understood that any copying or publication or use of this thesis or parts thereof for financial gain shall not be allowed without my written permission. It is also understood that due recognition shall be given to me and to the University of Saskatchewan in any scholarly use which may be made of any material in my thesis.

Requests for permission to copy or to make other use of material in this thesis in whole or part should be addressed to:

Head of the Department of Physics and Engineering Physics
Physics Building
116 Science Place
University of Saskatchewan
Saskatoon, SK S7N 5E2
Canada

ABSTRACT

This thesis has two major objectives. The first objective is to investigate the seasonal and diurnal variations in occurrence of HF coherent echoes. We assess F-region echo occurrence rates for the PolarDARN HF radars at Inuvik (INV) and Rankin Inlet (RKN) and the auroral zone SuperDARN radars at Saskatoon (SAS) and Prince George (PGR) for the period of 2007-2010. We show that the INV and RKN PolarDARN radars show comparable rates of echo occurrence all the time and they detect 1.5-2.5 times more echoes through ½-hop propagation mode (MLATs = 80°-85°) than the SAS and PGR SuperDARN radars through 1½-hope propagation mode (MLATs=75°-80°). For all four radars, the winter occurrence rates are about ∼2 times higher than the summer rates. For observations in the dusk, midnight and dawn sectors, equinoctial maxima are evident. The pattern of echo occurrence in terms of MLT/season is about the same for all radars with clear maxima near noon during winters and summers and enhanced (as compared to other time of the day) occurrence rates during equinoctial dusk and dawn hours. Additionally, to investigate the effect of solar cycle on occurrence of F-region echoes, we consider the near noon and near midnight echo occurrence rates for the Saskatoon radar over the period of 1994-2010. We show that there is a strong, by a factor of ∼10, increase in SAS night-side echo occurrence towards solar maximum. The effect does not exist for the dayside echoes; moreover, a decrease in number of echoes, by a factor of ∼2, was discovered for the declining phase of the solar cycle.

The second objective is to evaluate the electron density and the electric field as factors controlling the occurrence of F-region echoes. We use observations of these two ionospheric parameters measured by CADI ionosonde and RKN observations of echo occurrence rates over Resolute Bay (MLAT=83°). We show that there is a correlation in changes of echo occurrence and electron density changes for 3 years of radar-ionosonde joint operation (2008-2010). The comparison of radar-ionosonde data shows that the enhanced echo occurrence at near noon hours during summer months correlate with the enhanced electric field during these periods.

ACKNOWLEDGEMENTS

First and foremost, I would like to thank my supervisor Dr. Alexander Koustov for his continuous guidance and generous help throughout my Master's program. I am truly grateful for the opportunity he has given me to study under his supervision.

I would like to thank all current and past members in the Institute of Space and Atmospheric Studies (ISAS) at the University of Saskatchewan, including; Dr. George Sofko for his invaluable instruction; Dr. Robyn Fiori and Daniel Mori for their useful programing advice; Dr. Pavlo Ponomarenko for his helpful comments; and Gareth Perry for managing many Friday group meetings.

I would also like to thank Dr. Dieter André and Engineer Jan Wiid for the availability of the Polar/SuperDARN data used in this thesis. Many thanks to members of the CHAIN group at the University of New Brunswick; Dr. P. T. Jayachandran, Richard Chadwick and David Themens for the availability of the CADI data.

Finally, I am grateful for financial support received from the College of Graduate Studies and Research, the Department of Physics and Engineering Physics at the University of Saskatchewan, and Natural Sciences and Engineering Research Council of Canada.

TABLE OF CONTENTS

LIST OF TABLES

LIST OF FIGURES

LIST OF ABBREVIATIONS

ACF	Autocorrelation Function
CADI	Canadian Advanced Digital Ionosondes
CHAIN	Canadian High Arctic Ionospheric Network
CUTLESS	Co-operative UK Twin Auroral Sounding System
EISCAT	European Incoherent Scatter
e-POP	Enhanced Polar Outflow Probe
fEF2	Extraordinary F2 Peak Critical Frequency
fOF2	Ordinary F2 Peak Critical Frequency
FoV	Field of View
GDI	Gradient-Drift Instability
GLAT	Geographic Latitude
GSM	Geocentric Solar Magnetospheric
HAN	Hankasalmi
HF	High Frequency
IMAGE	Imager for Magnetopause-to-Aurora Global Exploration
IMF	Interplanetary Magnetic Field
INV	Inuvik
IRI	International Reference Ionosphere
ISR	Incoherent Scatter Radar
LoS	Line of Sight
LT	Local Time
MCM	McMurdo
MLAT	Magnetic Latitude
MLT	Magnetic Local Time
NmF2	F2 Peak Electron density
PC	Polar Cap
PGR	Prince George
Polar/SuperRDARN	Polar/Super Dual Auroral Radar Network
RB	Resolute Bay
R_E	Earth’s Radius
RISR-C	Resolute Bay Incoherent Scatter Radar – Canada
RKN	Rankin Inlet
SAS	Saskatoon
SW	Solar Wind
TALO	Taloyak
TIGER	Tasman International Geospace Environment Radar
UT	Universal Time
VHF	Very High Frequency

CHAPTER 1

INTRODUCTION

The Sun affects everything in the solar system, including the interplanetary space itself and the planets, by its variable magnetic field, electromagnetic radiation and charged particles continuously ejected from it. The planets respond differently to the Sun's influences, depending on their magnetic field, the structure of their atmosphere and, if available, current-conducting layer, ionosphere. The Earth is one of the planets whose electrodynamic environment is extremely sensitive to changes in the Sun's state. In this chapter we introduce major elements of the Sun-Earth system, describe their characteristics and discuss some ongoing processes relevant to this thesis. The description to follow is based on the books by *Kelley* (1989), *Hargreaves* (1992), *Kivelson and Russell* (1995), *Baumjohann and Treumann* (1997), *Schunk and Nagy* (2000) and *Hunsucker and Hargreaves* (2003).

1.1 The Sun

Under very hot temperatures of 1.5×10^7 K inside the Sun's core, continuous fusion supplies the thermal energy that is transferred through the radiative layer and the thermal convection zone into the outer regions of the Sun, the photosphere and chromosphere. The photosphere is the part of the Sun that we see with our eyes. This is a region where we also see dark sunspots that, as known for many years, characterize the level of Sun's activity. The photosphere has a temperature between 4500 and 6000 K. The temperature increases dramatically in the transition layer just above chromosphere where the solar corona begins; it stretches all the way to the solar system planets.

Energy flow in the Sun's environment is accompanied by emission of electromagnetic waves across most of the electromagnetic spectrum as well as a stream of charged particles, known as the solar wind. All Sun's parameters, such as temperature, density and material outflow speed, change on various time scales, from local area changes on a scale of minutes, for example as for solar flare events, to global changes on a scale of years, for example changes of the Sun's magnetic field polarity that occurs about every 22 years.

Variations in the Sun's activity modulate the strength of its electromagnetic radiation and the solar wind. Figure 1.1 illustrates the changes of sunspot numbers over many years of observations. Obvious increase (decrease) on sunspot numbers around 2001 (1997, 2008) are seen. Previous maximum of solar activity occurred about 11 years earlier. The activity within the cycle, though, is not uniform; it takes about 4 years to rise from a minimum (in 1997) to a maximum (in 2001) and about 7 years to fall to a minimum once again (in 2008).

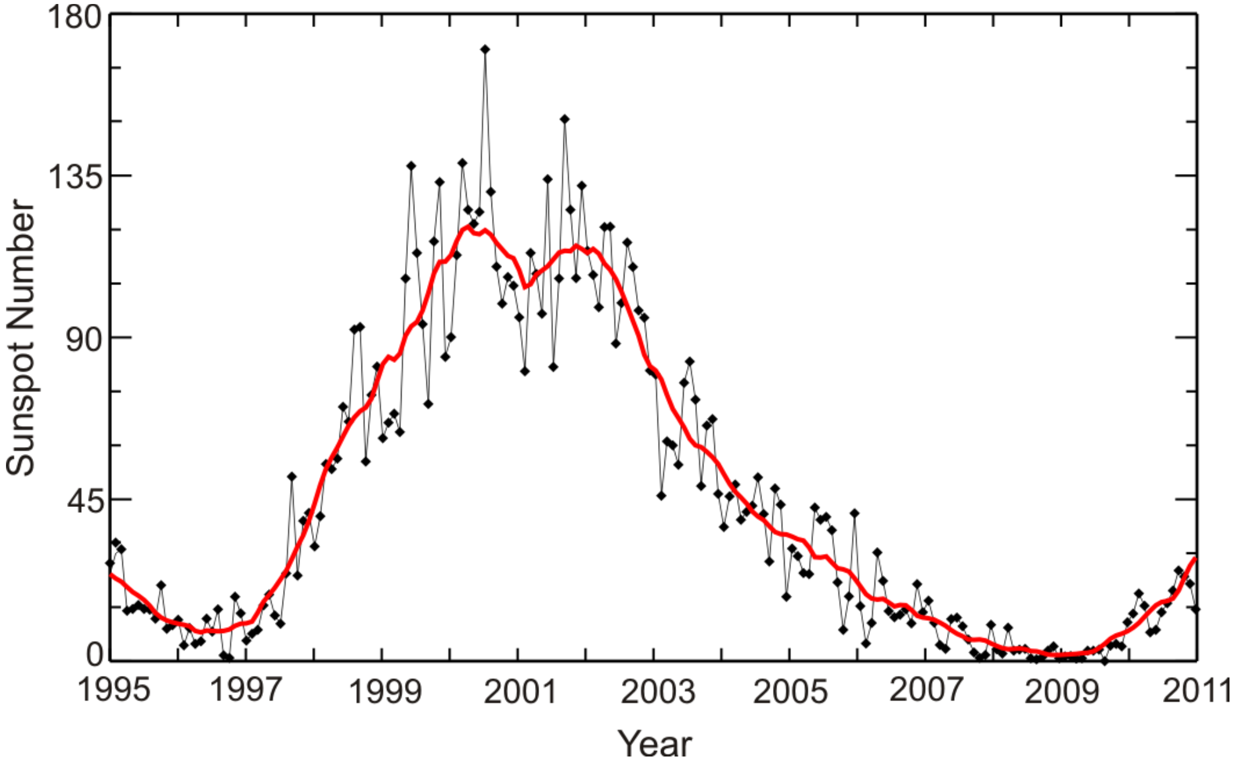

Figure 1.1: The monthly (black) and monthly smoothed (red) sunspot numbers for the period 1995-2011. The data were provided by the Solar Influences Data analysis Center.

1.2 The solar wind

The solar wind consists of electrons and positively charged ions of Hydrogen (95%), Helium (4%) and minor constituents ($\sim 1\%$) such as Carbon, Nitrogen, Oxygen, Neon, Magnesium, Silicon and Iron. The ions are created when the corresponding atoms lose electrons due to the high temperature of the Sun's corona ($\sim 3 \times 10^6$ K). The solar wind is electrically quasi-neutral; such a mixture of charged particles governed by electrodynamic forces is called plasma. The first successful theoretical model of the solar wind plasma suggested by *Parker* in 1958 predicted that the flow being subsonic at the start-out (the plasma flow velocity is below the ion-acoustic speed of the medium) quickly becomes supersonic (at a distance of about four solar radii away from the Sun's surface). Satellite observations have confirmed that the solar wind near the Earth's orbit is indeed supersonic (e.g., *Kivelson and Russel,* 1995).

The solar wind is not homogeneous in the radial direction; it is usually comprised of two types of flows, the slow one and the fast one. The slow solar wind originates from Helmet streamers, the Sun's regions with closed magnetic field lines which overlie the active regions on the photosphere. The slow solar wind has a velocity of 250-400 km/s, a density of $\sim 10^7$ m^{-3} and a temperature of (1.4-1.6) $\times 10^6$ K. The fast solar wind originates from coronal holes, the regions of open magnetic field lines in the Sun's corona. The fast solar wind has a velocity value of about 500-800 km/s, a density of $\sim 3 \times 10^7$ m^{-3} and a temperature of $\sim 8 \times 10^5$ K.

1.3 Interplanetary magnetic field and the frozen-in field lines concept

The Interplanetary Magnetic Field (IMF) is a part of the Sun's magnetic field that is carried into the interplanetary space by the solar wind. The IMF is a weak field, varying in strength near the Earth's orbit from 1 to 30 nT, with an average value of about 5 nT. The IMF is a vector quantity. The three components of the IMF can be presented in the Geocentric Solar Magnetospheric (GSM) system. The GSM has its x-axis from the Earth to the Sun. The y-axis is defined to be perpendicular to the Earth's magnetic dipole toward dusk, so that the x-z plane contains the dipole axis. The positive z-axis is chosen as $\hat{z} = \hat{x} \times \hat{y}$.

One of the most important properties of the IMF is that it is "frozen in" into the plasma, i.e. the magnetic flux is carried unchanged in a given parcel of the plasma moving with the solar wind speed. This means that the plasma particles are linked to a magnetic field line and always remain on that magnetic field line as the plasma moves. Therefore, one can say that the plasma and the magnetic field lines are stick together or, in other words, the magnetic field lines are frozen in the plasma. As a result, in highly conducting plasma (where no collisions occur) there is no electric field in the frame moving with the plasma. Electric field rises in respect to an observing frame such as the Earth. This electric field is given by

$$\boldsymbol{E} = -\boldsymbol{v}_{sw} \times \boldsymbol{B} \tag{1.1}$$

where $\boldsymbol{v}_{sw}$ is the velocity of the solar wind and $\boldsymbol{B}$ is the IMF. For negative IMF B_z, the electric field in the magnetosphere is oriented from dawn to dusk that is known as dawn-to-dusk magnetospheric electric field. Its strength varies over the time of day, season and solar cycle, but it is usually about 2-4 mV/m.

1.4 Magnetosphere

As the highly conducting plasma of the solar wind with frozen-in magnetic field lines reaches the Earth's magnetic dipole, it cannot penetrate through it. Instead, the flow is slowed down, deflected around the Earth, and a magnetic cavity is formed around the Earth. It is called the magnetosphere. The magnetosphere has a complex structure both in terms of particle population and electric and magnetic fields. Its formation involves a number of processes including interaction with the highly conducting upper part of the atmosphere called the ionosphere. In Sections to follow, we introduce main magnetospheric and ionospheric regions.

1.4.1 Magnetospheric regions

Since the solar wind approaches the Earth's with a supersonic speed, a shock wave is formed in front of the Earth; it is known as the bow shock. The bow shock is located at a distance of 12-14 R_E upstream from the Earth, depending on the strength of the solar wind flow. The plasma temperature and density of the stream increase as it crosses the bow shock while its speed decreases. This heated, compressed and subsonic plasma forms a region behind the bow shock called the magnetosheath. This is where the shocked solar wind plasma is deflected around the Earth's magnetic field. The boundary separating the magnetosheath from the magnetosphere is known as the magnetopause.

On the dayside, the magnetopause is usually located at a distance of about 10 R_E, but for the fast solar wind streams it can shrink to less than 6-7 R_E. The thickness of the magnetopause can be estimated from the ion-gyro radius as about 200-300 km. On the nightside of the Earth's dipole, the magnetosphere is stretched as a long cigar-like cavity (up to $\sim$1000 R_E) known as the magnetotail. The magnetotail is $\sim$40 R_E in diameter and is comprised of three main Sections, the plasma sheet, and northern and southern lobes.

The plasma sheet (light green area in Fig. 1.2) is a central region in the magnetotail with high temperature (5×10^5K) and low density plasma ($\sim 0.5\ \mathrm{cm}^{-3}$). The strength of the magnetic field in the plasma sheet is ~ 10 nT. The plasma sheet separates the northern and southern lobes of the magnetotail (light red area in Fig. 1.2). The plasma in these lobes has lower temperature (5×10^5 K) and density ($\sim 10^{-2}\ \mathrm{cm}^{-3}$) than the plasma sheet. However, the magnetic field is stronger in the lobes (~30 nT) than in the plasma sheet. The direction of the magnetic field changes from northern to southern lobes; in the northern lobe the magnetic field points towards the Earth while in the southern tail lobe it points away from the Earth.

Near the Earth at a distance of about $4\ R_E$, there is a torus-shaped region called the plasmasphere which co-rotates with the Earth (dark green area in Fig. 1.2). The plasmasphere contains dense ($\sim 10^2\ \mathrm{cm}^{-3}$) but cold ($\sim 5 \times 10^3$ K) plasma. Closer to the Earth the radiation belts lay between about 2-6 R_E, following the magnetic field lines (gray areas in Fig. 1.2). These belts consist of energetic electrons and ions which move along the field lines and oscillate back and forth between the mirror points in the southern and northern hemispheres. The typical values of the electron density and temperature in this region are $\sim 1\ \mathrm{cm}^{-3}$ and $\sim 5 \times 10^7$ K, respectively. Two other important regions of the near Earth magnetosphere are the southern and northern cusps (orange areas in Fig. 1.2). These are cone-shape regions which lay down between the closed dipole field lines on the dayside and the open field lines that are stretched all the way to the night side. The cusps are the only regions in the magnetosphere where the solar wind plasma from the magnetosheath can directly penetrate deep inside the magnetosphere and reach the ionosphere.

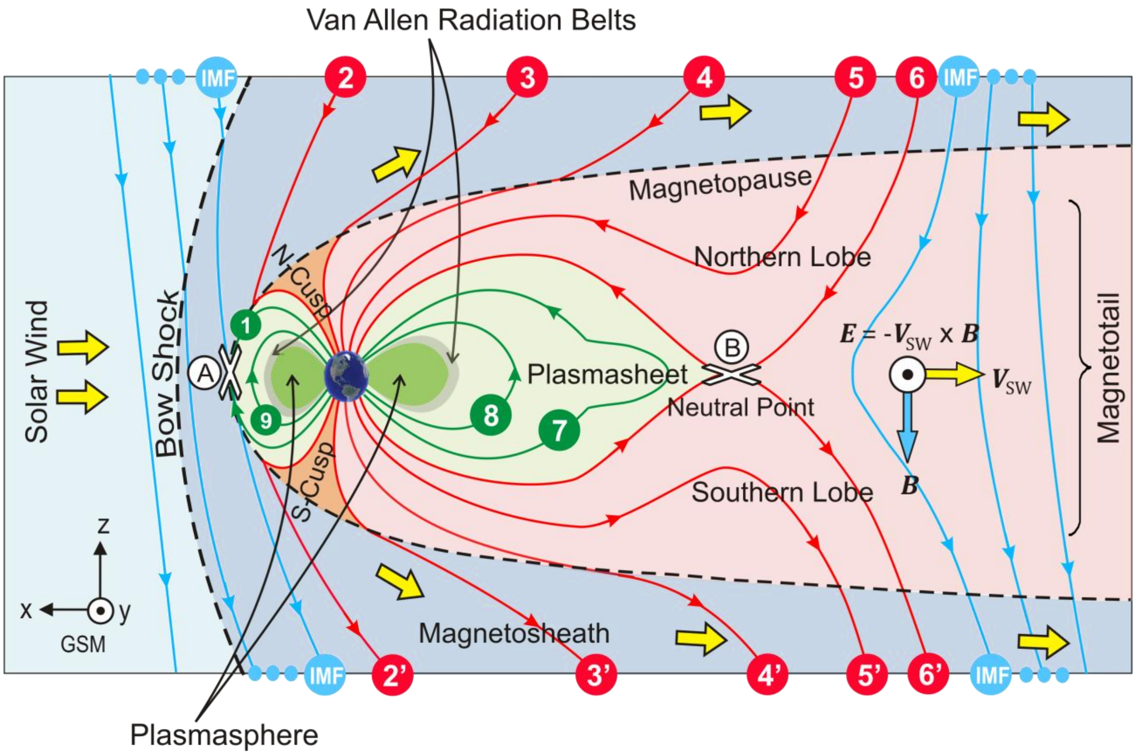

Figure 1.2: Cross section of the magnetosphere in the *x*-*z* GSM plane illustrating magnetospheric regions and reconnection processes between the IMF and Earth's magnetic field.

1.4.2 Magnetic reconnection and plasma convection cells

The merging and reconnection of magnetic field lines is a fundamental process in the solar and magnetospheric environments. The process explains plasma emissions in solar flares and coupling between the interplanetary magnetic field lines and the dipole geomagnetic field lines. The basic idea of reconnection is that when two oppositely-directed magnetic field lines meet one another, they can merge together and produce two different field lines, as suggested by *James Dungey* in 1961.

The two dimensional representation of Dungey's magnetospheric reconnection cycle for negative IMFB_z is illustrated in Fig. 1.2. The "open" southward IMF line merges with the closed northward geomagnetic field line 1 at point A (at the magnetopause front side) and forms the newly open field lines 2 (2´) in the northern (southern) lobe. These open field lines are carried downstream by the solar wind from position 3 (3´) to 5 (5´) in the northern (southern) lobe. Eventually, the two open magnetic field lines 6 and 6´ in the northern and southern lobes of the magnetotail reconnect at point B and form the new closed field line 7. The newly closed field lines (7 and 8) replace those ones that were merged to the IMF lines at point A (1 and 9), and this cycle repeats over and over again.

The plasma motion in the course of the reconnection cycle (but not immediately in the reconnection zone) can be projected into the high-latitude ionosphere. The footprints of the magnetic flux tubes are shown in Fig. 1.3a; the pattern has a form of two convection cells. The plasma moves according to these cells (or "convects") from noon sector to midnight sector (shown in Fig. 1.3a by field line numbers 2, 3, 4, 5 and 6) and returns to the merging point via dawn and dusk sectors (shown in Fig. 1.3a by field line numbers 7, 8, 9 and 1). The high-latitude region in the ionosphere that contains open (closed) magnetospheric field lines is known as the polar cap, light red area in Fig. 1.3a (auroral zone, light green area in Fig 1.3a). It was established that the transition boundary "open/closed field lines" corresponds to the poleward boundary of optical forms as observed with optical instruments detecting aurora borealis in visible light. Globally, this line is not symmetric with respect to the Pole. The region of aurora extends towards equator by several hundred kilometers. The region of most frequent occurrence of bright optical forms is known as auroral oval (yellow area in Fig. 1.3a). Figure 1.3b shows typical shape and location of the auroral oval as observed by the IMAGE satellite. It centers on geomagnetic pole and typically sits at geomagnetic latitudes of 72°-75° (60°-70°) on the dayside (nightside).

The plasma flow in the polar cap is powered by an electric field that originates from the dawn-to-dusk solar wind electric field in the magnetosphere, Eq. (1.1). The solar wind electric field maps along the magnetic field lines into the high-latitude ionosphere. In the polar cap, where the magnetic field lines are open, the mapping results in dawn-to-dusk directed electric field known as the polar cap electric field (E_{pc}) with typical strength of 20-30 mV/m. In the auroral zone, though, the direction of electric field is southward (northward) in the dawn (dusk) sector. The motion of charged particles in convection cells corresponds to the convection (Hall drift) $\boldsymbol{v_H} = \boldsymbol{E} \times \boldsymbol{B}/B^2$. The plasma motion in the high-latitude ionosphere due to the electric and magnetic fields will be discussed in Section 2.1 in more details.

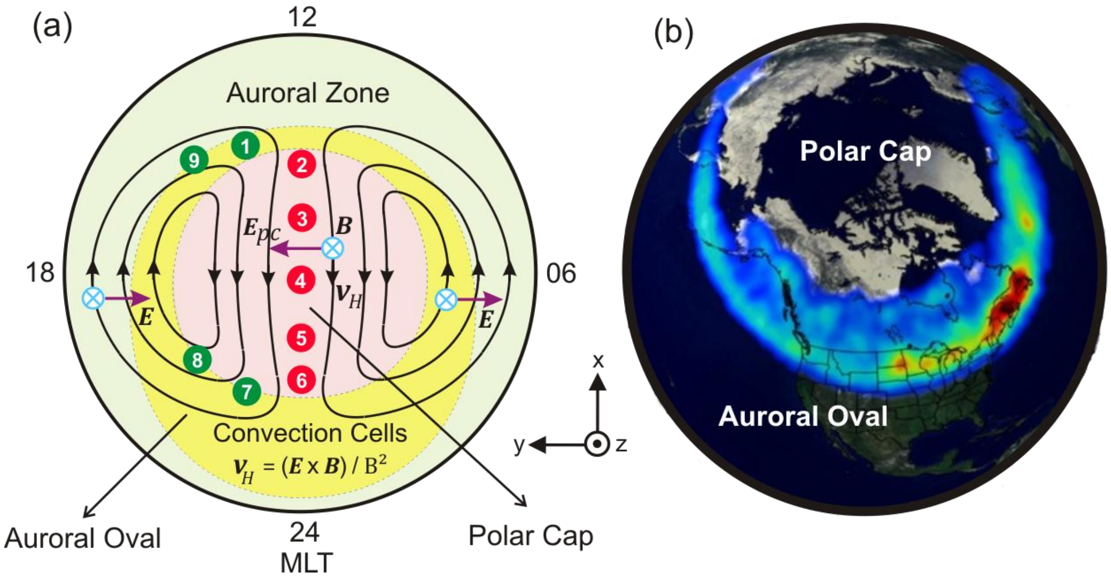

Figure 1.3: (a) High-latitude ionospheric regions and motion of plasma particles as a result of magnetospheric reconnection processes. (b) Example of auroral oval in the high-latitude ionosphere as observed by the IMAGE satellite. The false-color red (blue) indicates the brightest (dimmest) (Source: National Space Science Data Center).

1.5 Ionosphere

The upper part of the Earth's atmosphere, the ionosphere, is a layer where there are charged particles. The amount of charged particles is not significant here as compared to the amount of neutrals; the ionospheric plasma is said to be partially ionized. Thus the ionosphere is a transition region from the fully ionized magnetosphere to the electrically neutral low-altitude atmosphere.

1.5.1 Electron and ion distribution in the ionosphere

The Earth's ionosphere is known to consist of three main layers termed D, E and F regions. The F region is the highest region of the ionosphere at altitudes ~150 to 600 km. It has the greatest concentration of electrons (typically $\sim 10^{6}$ cm^{-3}) that peaks at ~270 km. During daylight hours F region can be distinguished as two layers: F1 layer that peaks at ~170 km and F2 layer that peaks at ~300 km. At night they become one at about the level of the F2 layer. The F1 layer is comprised of molecular and atomic ions O_2^+, NO^+ and O^+. In the F2 layer the atomic oxygen becomes the dominant ion.

The middle ionospheric region, E region, extends from ∼95 to ∼150 km above the ground. The E-region peak of electron density occurs at altitude ∼120 km with a typical value of ∼10^5 cm^{-3} during the day. The molecular ions NO^+ and O_2^+ have the majority of ions population in the E region, though the concentration of NO^+ is greater than O_2^+. Due to the lack of photoionization during night hours and recombination of ions and electrons, the E region is significantly diminished at night.

The D region is the lowest region of the ionosphere existing at altitudes between 70 and 95 km. The D region has a typical electron density of ∼10^4 cm^{-3}, but the peak of the electron density usually is not distinct. The D region completely disappears at night when there is no photoionization. The ion-electron pair production and the recombination processes in the D region are complicated and will not be reviewed here.

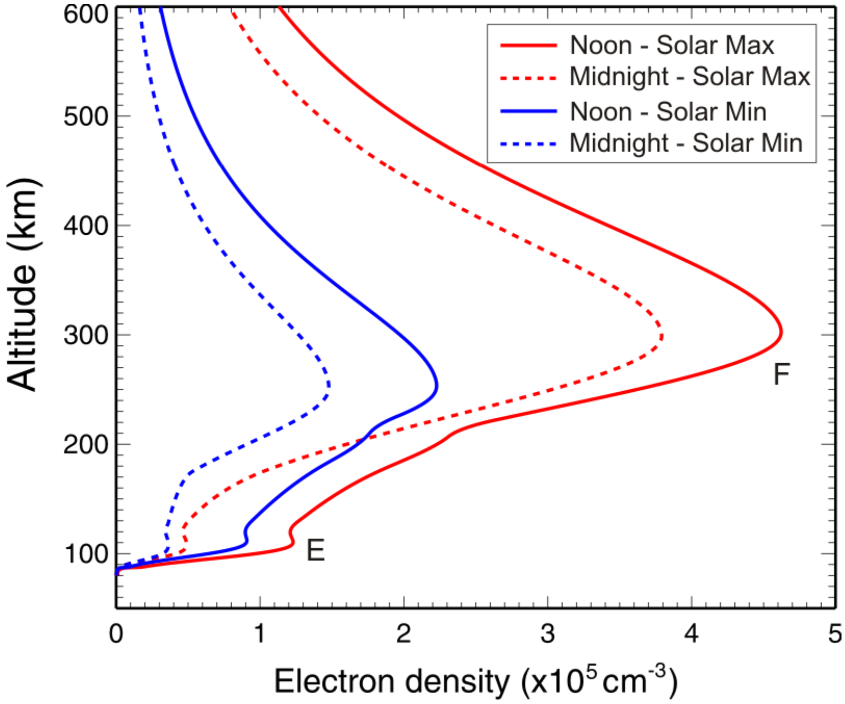

Figure 1.4: IRI electron density profile over Resolute Bay at Λ = 83° on 15 March of 2002 (red) and 2008 (blue) at 12:00 LT (solid) and 24:00 LT (dashed).

Most of our knowledge about these ionospheric regions has been learned through observations. A number of empirical models have been proposed. Currently, the most popular one is the International Reference Ionosphere (IRI) model. The IRI is based on all available worldwide data sources such as ionosondes, incoherent scatter radars and instruments on the satellites and rockets. Figure 1.4 illustrates the electron density profile for one spot of the high-latitude ionosphere, Resolute Bay (RB), Canada, magnetic latitude (MLAT) of $\Lambda = 83°$. This is a point of special interest in this thesis. The plot shows the structure of the ionospheric regions at noon and midnight hours on 15 March of the year of minimum (2008) and maximum (2002) of solar activity. Although the IRI data are available at altitudes starting from 80 km, the D-region peak cannot be seen for this month.

1.5.2 Seasonal and solar cycle variations of the F-region electron density

Numerous studies have shown that electron density profiles change significantly with height and time. Besides generally chaotic and unpredictable local changes, smoother and relatively definite temporal variations have been identified. Among well-established sources of "regular" variability of the ionosphere are the solar cycle and seasonal variations. The role of the first one can be understood from the fact that both the composition of the atmosphere and solar irradiation change within the 11-year cycle. In addition, enhanced reconnection rates during solar maximum periods lead to an increase of particle precipitation to the high-latitude ionosphere. One can expect seasonal variations by recalling that the maximum electron density depends on the solar zenith angle which changes over a season for a specific point in the ionosphere. The global-scale and smooth variations of the Earth's ionosphere are probably reasonably captured by the IRI model. Here we prefer to go on actual measurements as we consider high latitudes where IRI performs much less reliably.

To illustrate variations in the ionospheric electron density, we attracted data from the ionosonde operated at the Sodankyla Geophysical Observatory, Finland (Source: http://www.sgo.fi). The observatory is located close to the auroral zone at magnetic latitude of $\Lambda = 64.1°$ and thus is very relevant to the work done in this thesis. The advantage of this station is in the fact that long-term data, since the International Geophysical Year - 2 (1957), are available. We consider here monthly medians of the maximum electron density of the F2 layer.

Figure 1.5 considers the maximum F2-layer electron density for three separate months of 2004, March, June and December. These months are representative ones for equinox, summer and winter, respectively. The density in Fig. 1.5 is plotted versus universal time (UT). For Sodankyla, the universal time is related to local time (LT) through LT=UT+2 hours.

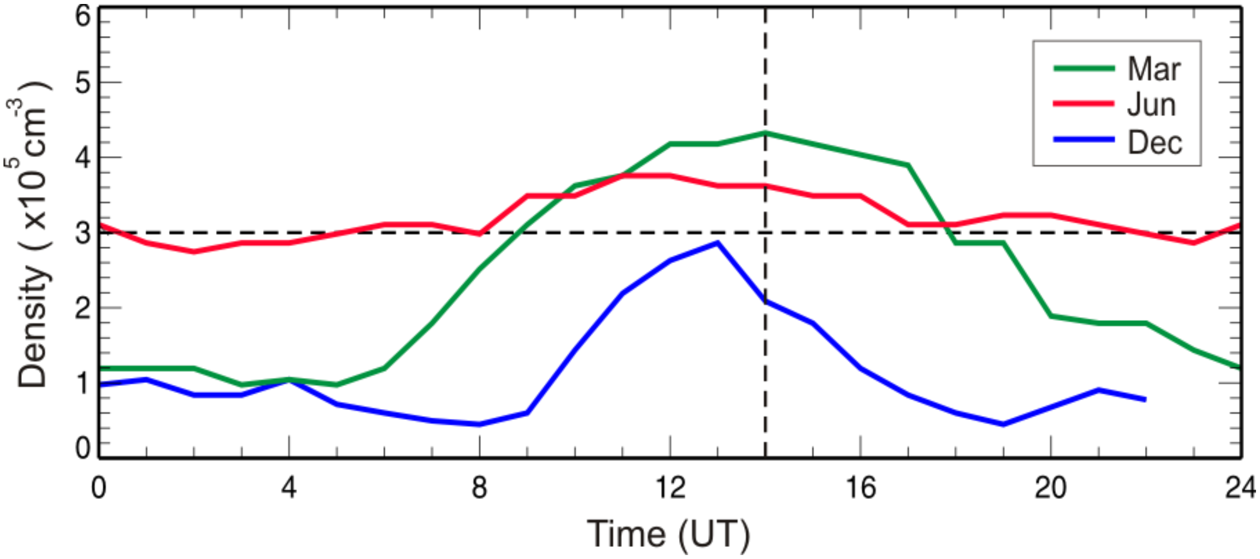

Figure 1.5: Median values of the electron density at the maximum of F2 layer according to Sodankyla ionosonde measurements in 2004.

Clear trends in Fig. 1.5 are obvious; the density increases towards local noon and then decreases back to the night-time values. The variation is strongest for March, where span is (1-4) $\times 10^5$ cm^{-3}. This is perhaps just slightly stronger variation than in December where density has barely reached 3×10^5 cm^{-3} at near noon hours. However, the enhanced densities existed for much shorter time interval than in March (about 6 hours versus 14 hours). In June, the density was relatively high all the time varying in (3.0-3.5) $\times 10^5$ cm^{-3}. Clear maxima in the electron density at near noon hours are consistent with the maximum solar zenith angle.

Figure 1.5 shows that the electron density experiences variations with the season. To illustrate this dependence in a more clear way, we present in Fig. 1.6 the monthly median values of the electron density during near noon maxima versus month for 2001 (the year of maximum in solar activity), 2004 (declining phase of the solar cycle) and 2008 (minimum of solar activity). The curve for the 2004 data is located in between the curves for solar maximum (larger values) and solar minimum (lower values). One obvious conclusion from Fig. 1.6 is that the seasonal variation is rather weak (strong) during solar minimum (maximum) period. The solar cycle effect is much stronger for winter conditions.

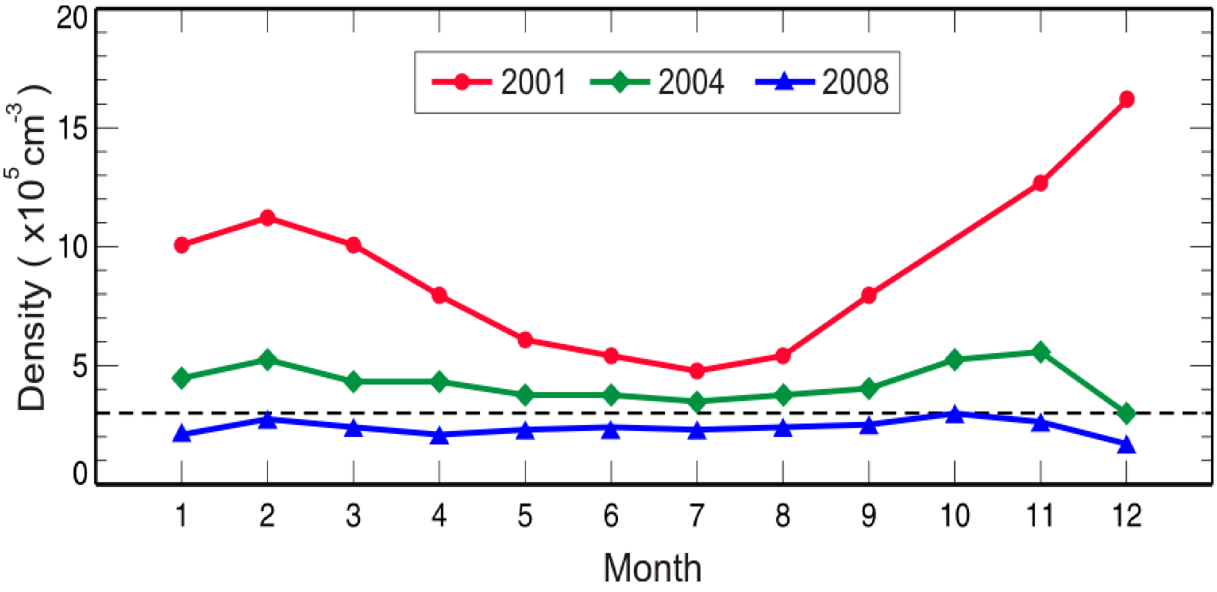

Figure 1.6: Median (monthly) values of the electron density at the maximum of F2 layer at near noon hours according to Sodankyla ionosonde measurements in 2001, 2004 and 2008.

Figure 1.7 presents electron density data (again monthly medians for near noon maxima) for the month of December but for the entire period of Sodankyla operation. Clear solar cycle variation is seen with largest values during the solar maximum periods when the density can be as high as 15×10^5 cm^{-3}. During the solar minima, the density is $\sim 2 \times 10^5$ cm^{-3}.

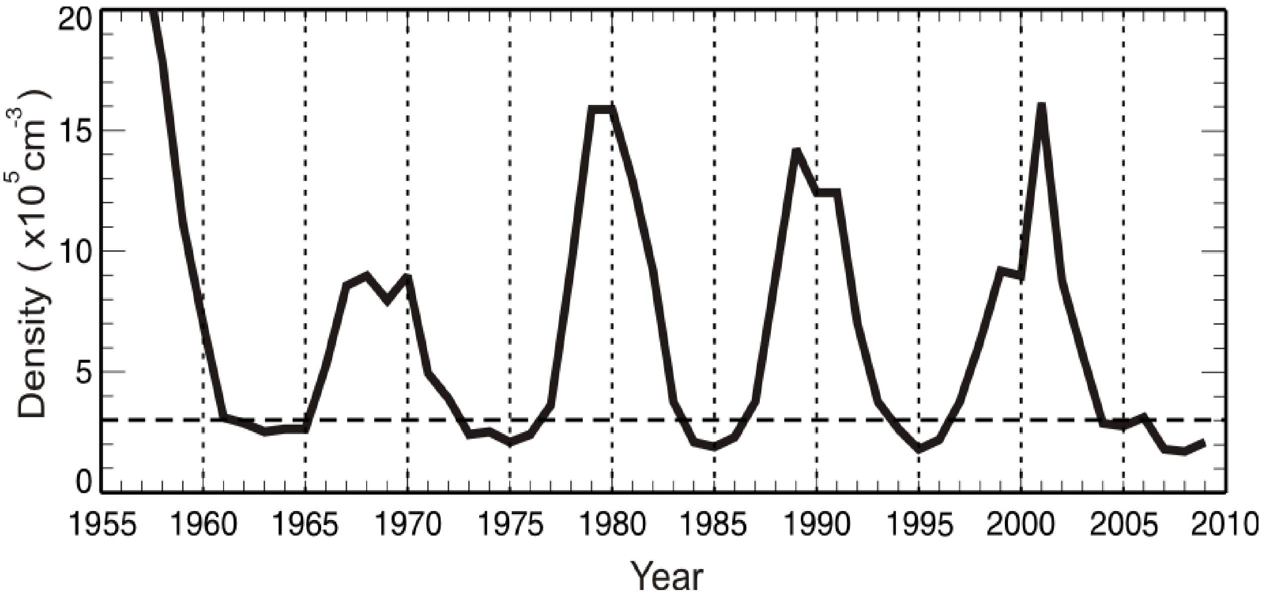

Figure 1.7: Median (monthly, December) values of the electron density at the maximum of near noon F2 layer according to Sodankyla ionosonde measurements in the period of 1957-2008.

1.5.3 Ionospheric fine structures - irregularities

The presented above data show temporal variability of the ionosphere due to changes in the global external factors such as the Sun's radiation. Numerous studies have shown that the ionosphere is strongly non-uniform spatially; at a fixed time, besides vertical layering, there is also strong horizontal inhomogeneity. The large-scale features (~1000s km in size), for example the mid-latitude trough of decreased F-region density, have been identified. At high latitudes, occurrence of areas with enhanced density due to energetic particle precipitation from the magnetosphere is an everyday phenomenon. In the polar cap, drifting patches of increased density were discovered. These are dynamical features; after onset on the dayside, they propagate through the entire polar cap, over the pole, to the nightside. Studies also showed occurrence smaller features, such as sporadic E layers (100-300 km in size). Rocket measurements showed occurrence of structure with about a kilometer and smaller sizes. Radar experiments indicate existence of very small-scale ionospheric structures, with sizes up to about centimeters. In this thesis, of special interest will be 10-20 m structures in the ionosphere. It is believed that these can be excited in trains of quasi-periodic wave-like packets and they are often called decameter irregularities.

The nature of ionospheric irregularities has been a subject of numerous studies (e.g., *Kelley*, 1989). It is believed that they occur due to plasma instabilities in the ionosphere, a growth of spontaneous plasma density fluctuations from thermal level to much larger amplitudes. For the irregularities of interest in this thesis, the so called Gradient-Drift Instability (GDI) is important. The GDI occurs in the presence of strong background plasma density gradient in the direction of plasma motion driven by the background electric field. The GDI will be discussed in Section 2.2 in more details. Here it is important to emphasize that it occurs when the electric field is sufficiently strong and there is a plasma gradient of proper direction. It is also important to know that the decameter irregularities are highly-aligned with (stretched along) the Earth magnetic field. This can be understood from the fact that electron and ion mobility along the magnetic field is much larger than across it.

1.5.4 Coherent radars as instruments for studying ionospheric structure

In situ measurement of decameter irregularities is a difficult experimental task. This is coupled with the fact that rocket flights are expensive and thus very infrequent. The large body of information on ionospheric decameter irregularities has been obtained through observations with the ionospheric coherent radars.

Figure 1.8a illustrates the typical geometry of ionospheric irregularity studies with a coherent radar. The radar is located on the ground; it transmits radio waves into the ionosphere. If the radio waves meet the Earth's magnetic field at a ∼90° angle, as shown, the radio waves can be scattered back by ionospheric irregularities. Orthogonality condition is needed because the irregularities are stretched along the magnetic field.

The scattering process is analogous to the Bragg scatter of X-rays from a crystal. The geometry of the radar wave scatter is shown in Fig. 1.8b in which $\boldsymbol{k}_t(\boldsymbol{k}_s)$ is the wave vector of the transmitted (scattered) wave and $\boldsymbol{k}_p$ is the wave vector of the plasma wave irregularities produced by the GDI. The conservation law of linear momentum $(\boldsymbol{p}_t + \boldsymbol{p}_p = \boldsymbol{p}_s)$ yields an important property of the coherent scatter

$$\lambda_p = \frac{\lambda}{2\,|\cos\psi|} \tag{1.2}$$

where λ_p is the wavelength of the plasma irregularities, λ is the wavelength of the transmitted signal and ψ is the off orthogonality angle. For $\psi = \pi$, i.e. a radar with the transmitter and receiver at the same location, Eq. (1.2) reduces to $\lambda_p = \lambda/2$. Thus the scale of plasma irregularities in the ionosphere causing the coherent backscatter is half of the transmitted wavelength. This is referred to as the Bragg condition. Backscatter signals are amplified under the Bragg condition to produce a signal strong enough to be detected by the receiver. The term "coherent" comes from the fact that a returned signal originates from constructive interference of signals scattered from fronts of a quasi-periodic structure with spatial periodicity of half the radar wavelength. Experiments showed that coherent radars can successfully detect echoes at frequencies between 3 and 3000 MHz. In this thesis we use coherent radars operating at HF frequencies of ∼10 MHz (irregularity wavelength of ∼15 m).

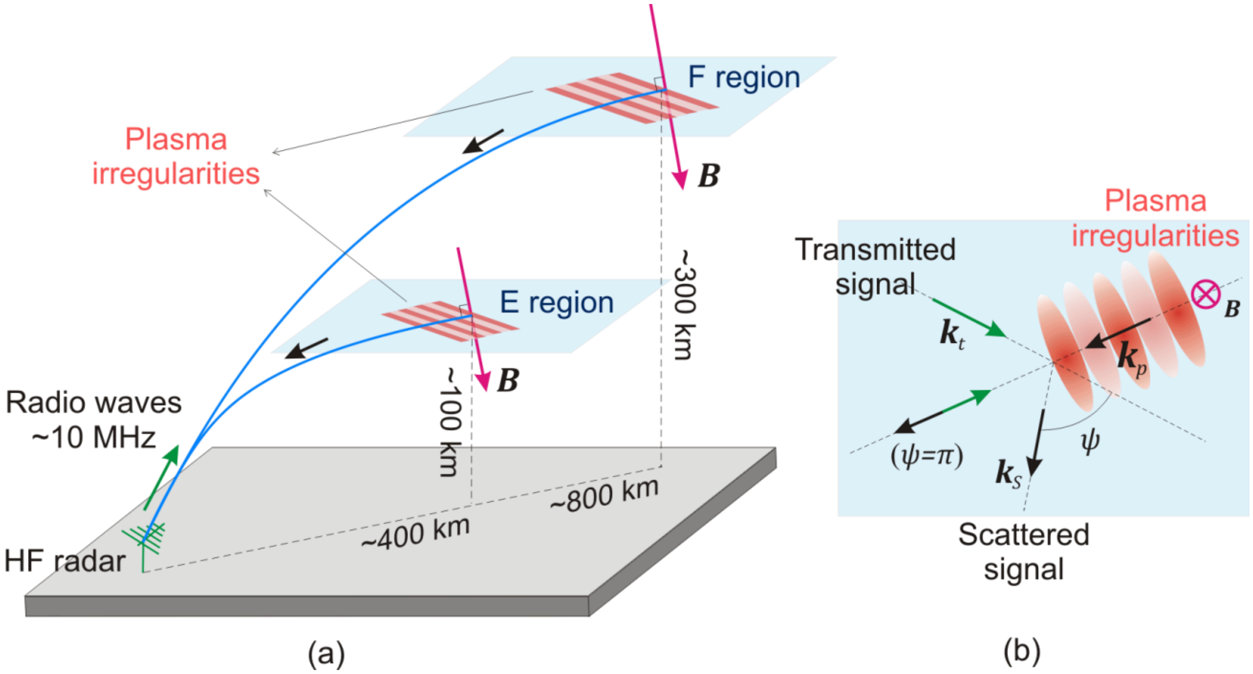

Figure 1.8: (a) Geometry of simultaneous detection through direct scatter from E and F regions using a coherent HF radar (b) Scattering of HF radio waves from plasma irregularities.

1.5.5 Use of ionospheric irregularities for studying the ionosphere

Investigation of coherent echo parameters in their relationship to background conditions, for example electric field, is a well-developed branch of space physics (*Kelley*, 1989). Efforts in this area are aimed at understanding the plasma processes leading to the development of structures in the ionosphere. However, coherent echoes are useful for the opposite task – inferring and continuous monitoring of the background conditions in the ionosphere using the parameters of echoes from the ionospheric structures. A good example of such an approach is the Super Dual Auroral Radar Network (SuperDARN) experiment (*Greenwald et al*., 1995). The SuperDARN network consists of a number of coherent HF radars that measure Doppler velocity of coherent echoes and infer background electric field in the ionosphere. Such information is highly desirable as the electric field distribution in the ionosphere depends strongly on the character of interaction between the solar wind and magnetosphere. We discussed earlier that the magnetospheric plasma circulation leaves its imprint in the ionosphere in the form of a two-cell convection pattern for negative IMF B_z. Studying temporal and spatial variations of such patterns allows one to assess quantitatively the location and intensity of magnetospheric merging processes. Thus information on coherent echoes can be used to investigate magnetospheric processes of interaction between the solar wind and magnetosphere by means of the magnetospheric coupling to the ionosphere.

SuperDARN radar experiment

SuperDARN is a multi-national experiment aimed at studying electrodynamical processes in the Earth's ionosphere and magnetosphere. The first radar of the SuperDARN network was installed in Goose Bay in 1983, and later in Halley (Antarctica) but the real networking has begun in 1993 with almost simultaneous installation of 3 additional radars in Saskatoon (Canada), Kapuskasing (Canada), and Stokkseyri (Iceland). The SuperDARN network is currently comprised of 21 radars in the northern hemisphere and 12 radars in the southern hemisphere and more radars are under construction.

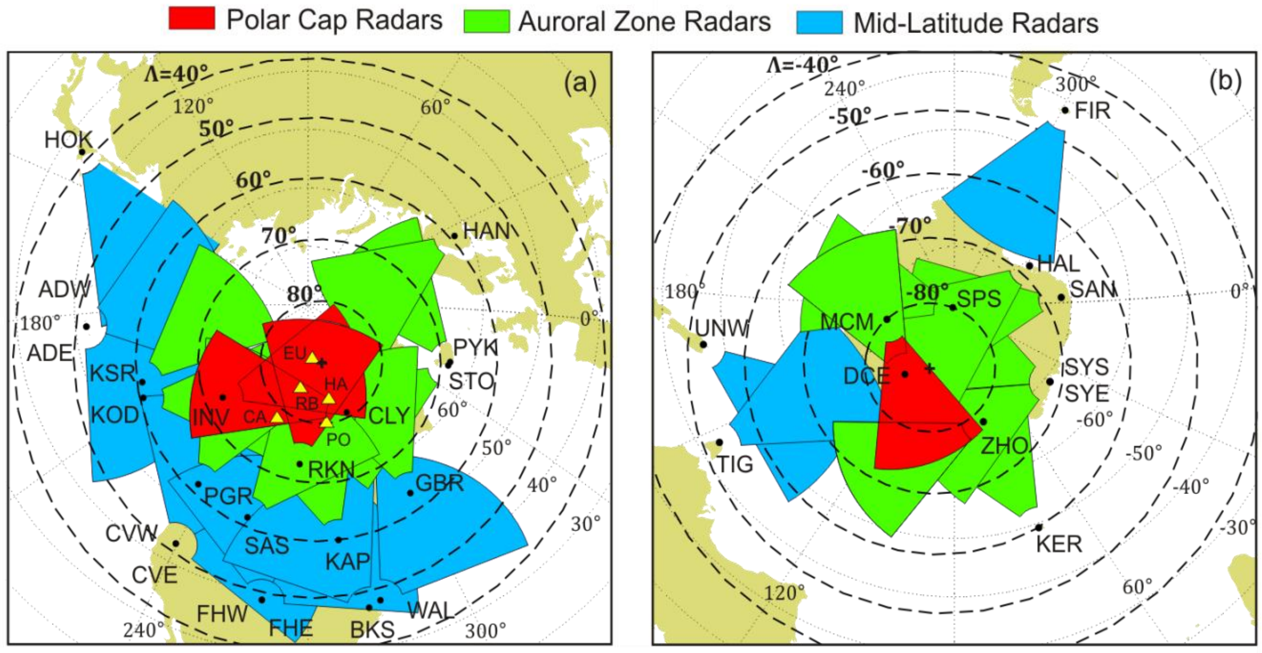

Figure 1.9: Fields of view of the SuperDARN radars in (a) northern hemisphere and (b) southern hemisphere. The yellow triangles show the location of CHAIN CADI ionosondes.

The Fields of View (FoVs) of the operating SuperDARN radars in the both hemispheres are shown in Fig. 1.9. In terms of location and viewing zone, the radars can be categorized into three groups: mid-latitude, auroral zone and polar cap radars (shown in Fig. 1.9 by blue, green and red, respectively). The radars are synchronized and use the same principle of operation. The majority of the data available so far were collected using the auroral zone radars. Over the last several years, much more data became available from the mid-latitude and polar cap radars. In this thesis, special attention will be paid to two polar cap radars in the northern hemisphere at Rankin Inlet (RKN) and Inuvik (INV) (called the PolarDARN radars).

The SuperDARN radars transmit a series of pulses and measure the amplitude and phase of the backscattered signal for number of range gates and beam positions. From raw data, the backscattered echo power, the Doppler velocity and the spectral width are measured. Details on principle of SuperDARN radar operation will be given in Chapter 3.

The SuperDARN radars are versatile instruments. They are used for studying the nature of ionospheric irregularities. But the main target of the SuperDARN effort, as already mentioned, is production of global-scale maps of electric field (or equivalently plasma circulation) in the ionosphere with temporal resolution of about a minute. Figure 1.10 gives an example of the convection pattern produced using map potential technique (*Ruohoniemi and Baker,* 1998). On this map, the vectors represent the measured SuperDARN Line-of-Sight (LoS) velocities. The blue solid and red dashed lines represent the fitted equipotentials based on the map potential technique with a total cross polar cap potential of Φ_{pc}= 87 kV (between the cross and plus in Fig. 1.10).

Figure 1.10 is one of the examples of reasonable radar coverage. Often not too many vectors are present on the map due to the lack of echoes even if as many as ~30 radars operate simultaneously. Moreover, on the map presented, one can notice absence of echoes in many important places, for example, the Russian sector where there are no operational SuperDARN radars.

Clearly, successful SuperDARN radar convection mapping relies on high occurrence of coherent echoes. Studying of the trends in the SuperDARN echo occurrence is important for planning and proper installation of future HF radars within the network. Assessing occurrence of HF echoes thus is an important task. Such work will certainly not improve the radar echo detection rates but the results might be important for understanding the processes leading to the irregularity formation and for assessing long-term periodicities in these phenomena.

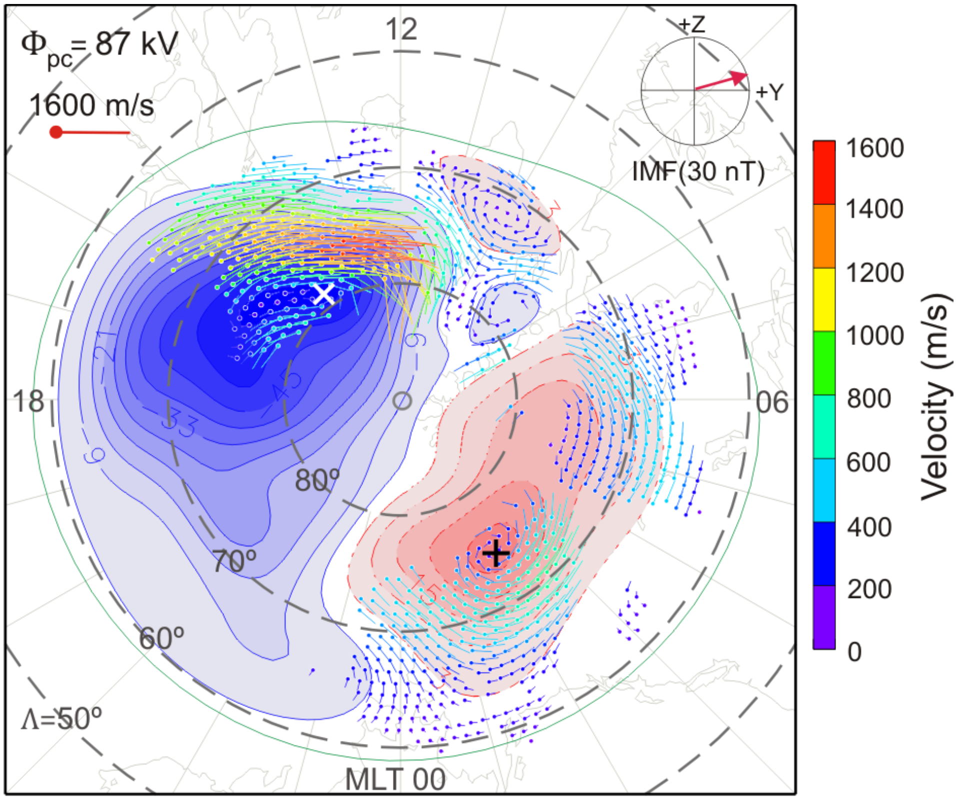

Figure 1.10: SuperDARN convection pattern determined on 19 December 2002 at 12:00 UT (Source: http://vt.superdarn.org).

1.6 Objectives of the undertaken research

This thesis is aimed at investigation of factors affecting occurrence of HF coherent echoes detected by the SuperDARN radars. We focus on F-region echoes received at relatively far ranges of above ~700 km. There are several reasons for limiting the scope and ignoring echoes at shorter ranges. One reason is that occurrence of E-region SuperDARN echoes has been a subject of several papers and theses (*Makarevich et al*., 2002; *Makarevich*, 2003; *Carter and Makarevich*, 2010; *Carter*, 2011). It has been shown that the diurnal, seasonal and solar cycle occurrence of such echoes is very much similar to what is known from VHF studies carried out over the last 50 years. The E-region echoes are less interesting in terms of assessing the SuperDARN capabilities in monitoring plasma circulation pattern because it has been established that the Doppler velocity of such echoes is related to the plasma drift in a complicated way so that more work is needed to understand how to extract information of plasma drifts from Doppler velocities of E-region echoes. To make further progress in this respect, independent instrument routinely measuring plasma drifts at short SuperDARN radar ranges is required. One of such instrument could be an incoherent scatter radar (ISR). Unfortunately, all currently existing ISR radars are separated from appropriate SuperDARN radars by at least 900 km, implying that E-region echoes cannot be observed regularly, and diligent work is required to recognize them within a body of echoes dominated by the F-region returns.

There is another reason for considering F-region echoes in this thesis. Over the past several years of the solar cycle 23 minimum, the PolarDARN radars at Rankin Inlet and Inuvik, monitoring echoes in polar cap, detect significantly more echoes than the auroral zone radars detecting F-region echoes at these latitudes (e.g., *Fiori et al*., 2009; *Liu*, 2010). This highly unexpected result needs to be understood. In addition, both PolarDARN radars can detect echoes over Resolute Bay (RB) where measurements of background ionospheric parameters are continuously carried out by the Canadian Advanced Digital Ionosonde (CADI) within the Canadian High Arctic Ionospheric Network (CHAIN) as described by *Jayachandran et al*. (2009). This provides opportunity to compare parameters of PolarDARN F-region echoes and the electron density and the electric field in a radar scattering volume.

More specific scientific goals being addressed in the thesis are as follows:

1) Long-term variations in occurrence of F-region SuperDARN echoes as seen by the radars at various geographic and geomagnetic locations. For this kind of study, data from radars operating for more than 10 years are required so that both the solar cycle minimum and the solar cycle maximum are covered. Although some SuperDARN work in this direction has been done in the past (earlier results will be reviewed in Chapter 2), we address issues that have not been considered so far. These include:

a) differences in the solar cycle effect for observations in the midnight sector and other sectors, with a special emphasis on the near noon echoes;

b) changes in the intensity of the seasonal variation of echo occurrence in various magnetic local time (MLT) sectors.

2) Occurrence of F-region ionospheric echoes in the polar cap as observed by the PolarDARN radars. In the study, the polar cap is simply associated with MLATs $>$ 80°. At the

time the work had been started the PolarDARN radar data were available for 2007-2010. The questions we asked ourselves are as follows.

a) What is the difference in echo occurrence between the auroral zone radars (Saskatoon and Prince George) and polar cap radars (Rankin Inlet and Inuvik) operating in the Canadian sector of Arctic? Our target is to compare echo detection while all radars look at about the same band of MLATs between 80° and 85° or to consider the bands of latitudes for best echo detection for each radar separately. We wanted to know if even slight enhancement in the solar activity towards 2011 would bring some changes in the echo detection rate for each of the radars.

b) Is there any seasonal variation in echo occurrence for observations in the polar cap? If yes, how strong is it as compared to the auroral zone radars? We also wanted to know how strong the seasonal effect for observations away from the midnight sector is.

c) What is the pattern of echo occurrence in terms of MLT for various seasons? Does it depend on whether echoes are received with a direct ½-hop propagation mode or with 1½-hop propagation mode?

3) Finally, the third thrust of the thesis is on assessing the factors affecting echo occurrence, the F-region electron density and electric field in the polar cap. Here we compare CADI ionosonde measurements of F-region critical frequencies (maximum electron density) with echo occurrence rate to see if more echoes occur for enhanced electron density that changes a) over the day and b) over the season. The electron density can affect echo detection through improving propagation conditions or affect the power of echoes directly (*Uspensky et al.*, 1994; *Ponomarenko et al*., 2009). The echo power is also affected by the level of electron density fluctuations in the ionospheric irregularities. The irregularity density might depend on the electric field magnitude, one of the factors crucial for starting out the gradient-drift instability and creation of irregularities themselves. Previous works (*Milan et al.*, 1997; *Danskinet al*., 2002; *Danskin*, 2003) where echo occurrence was compared with E field magnitude were done in the auroral zone at relatively short radar ranges of 900 km. For the RKN-RB comparison, the range is ~1350 km.

1.7 Thesis outline

The thesis is organized as follows. In Chapter 2 we consider details of the GDI excitation in the F region. To accomplish this, we describe plasma motions in the ionosphere and explain why the electric field, that drives the plasma, is a potentially important parameter for understanding the reasons for occurrence of F-region coherent echoes. We then present a theoretical formulation of the relationship between the power of coherent echoes and the electron density in the scattering volume. Finally, we review the current knowledge on occurrence of F-region echoes and factors that control it. In Chapter 3 we describe the instruments to be used in the thesis. These are Polar/SuperDARN radars and CADI ionosondes. The focus is on technical aspects of their operation. In Chapter 4 we present original data on the general trends in occurrence of F-region echoes according to the PolarDARN radars in the polar cap and SuperDARN radars in Saskatoon and Prince George (auroral zone radars). At the end of Chapter 4 we focus on long-term, 11-year periodicity of SuperDARN echoes as seen by the auroral zone radars in Saskatoon, Prince George and Hankasalmi (Finland). In Chapter 5 we investigate the relationship between occurrence of F-region echoes observed by RKN PolarDARN radar over RB and the electron density and the electric field measured at RB with the CADI instrument. Finally, in Chapter 6 we summarize the results and suggest possible future research in the area of thesis work.

CHAPTER 2

CURRENT UNDERSTANDING OF THE REASONS FOR OCCURRENCE OF COHERENT ECHOES

In this Chapter, we first explain how the GDI gets excited in the high-latitude F region. To accomplish this, we describe the motion of ions and electrons in crossed electric and magnetic fields in the F region. These motions are an energy source for a number of ionospheric instabilities, including the GDI. We then summarize the current knowledge on factors that control the power of coherent echoes. Finally, we review previous publications on the occurrence of F-region HF echoes.

2.1 Plasma motion in the F region due to the electric and magnetic fields

In the following discussion, we consider the motion of ions and electrons in the F region due to the large-scale electric field and the downward magnetic field. Considering all forces acting on the plasma particles, the equations of motion can be written as

$$m_\alpha \frac{d\boldsymbol{v_\alpha}}{dt} = q_\alpha(\boldsymbol{E}_0 + \boldsymbol{v}_\alpha \times \boldsymbol{B}) - m_\alpha \nu_{\alpha n}(\boldsymbol{v}_\alpha - \boldsymbol{u}_n) \pm m_e \nu_{ei}(\boldsymbol{v}_e - \boldsymbol{v}_i) - \frac{\boldsymbol{\nabla} P_\alpha}{n_\alpha} \qquad (2.1)$$

where $\alpha \equiv i, e$ stands for either the ions or electrons, m_α is the particle mass, q_α is the particle charge, $\boldsymbol{v}_\alpha$ is the particle drift, $\nu_{\alpha n}$ is the collision frequency of the particle with neutrals, ν_{ei} is electron-ion collision frequency, $\boldsymbol{u}_n$ is the velocity of neutrals, n_α is the particle density, $P_\alpha = n_\alpha \kappa_B T_\alpha$ is the particle pressure, κ_B is the Boltzmann constant and T_α is the particle temperature. The first term on the right hand side is the Lorentz force due to electric and magnetic fields. The second term is the frictional force due to the collisions of the plasma particles with neutrals. The third term is friction force due to ion-electron collisions where the positive (negative) sign applies to ions (electrons). Finally, the forth term presents the force due to pressure gradients in the plasma. To simplify the equation of motion we assume that the neutrals are at steady state with $\boldsymbol{u}_n = 0$. Secondly, we neglect the collisions between ions and electrons, and finally we consider a cold ionosphere where $T_\alpha = 0$. Then Eq. (2.1) becomes

$$m_\alpha \frac{d\boldsymbol{v}_{\boldsymbol{\alpha}}}{dt} = q_\alpha(\boldsymbol{E}_0 + \boldsymbol{v}_\alpha \times \boldsymbol{B}) - m_\alpha \nu_{\alpha n} \boldsymbol{v}_\alpha \tag{2.2}$$

Now we define a coordinate system in the ionosphere with the electric field directed along the positive *x*-axis ($\boldsymbol{E}_0 = E_{0x}\hat{x}$) and magnetic field directed along the negative *z*-axis ($\boldsymbol{B} = -B\hat{z}$). One can associate the *x*-axis direction with the line "dawn-dusk" in the polar cap. Then one can solve Eq. (2.2) at quasi-steady state ($d\boldsymbol{v}_{\boldsymbol{\alpha}}/dt = 0$) and obtain the particle drifts as

$$\boldsymbol{v}_{0\alpha} = \frac{\nu_{\alpha n}}{\Omega_\alpha^2 + \nu_{\alpha n}^2} \cdot \frac{q_\alpha E_{0x}}{m_\alpha} \hat{x} + \frac{\Omega_\alpha}{\Omega_\alpha^2 + \nu_{\alpha n}^2} \cdot \frac{q_\alpha E_{0x}}{m_\alpha} \hat{y} \tag{2.3}$$

where $\Omega_\alpha = |q_\alpha| B / m_\alpha$ is the particle gyrofrequency. The ion (electron) gyrofrequency in the ionosphere with $B \approx 0.5$ G has a value of ~ 160 (10^7) rad $\cdot$ s^{-1}.

At the F-region heights ($h > 150$ km), the collision frequency of both ions and electrons with neutrals is smaller than gyrofrequency ($\nu_{\alpha n} \ll \Omega_\alpha$). For instance, at the F-region height of $h \approx 300$ km, the ion (electron) collision frequency with neutrals is about 0.2 (40) s^{-1}. Therefore, from Eq. (2.3) the particle drifts perpendicular to the electric field are given by

$$\boldsymbol{v}_{0ye} = \boldsymbol{v}_{0yi} = v_H \hat{y} \tag{2.4}$$

where $v_H = E_{0x}/B$ is the strength of the vector $\boldsymbol{v}_{\boldsymbol{H}} = (\boldsymbol{E}_0 \times \boldsymbol{B})/B^2$ known as Hall drift, convection or $\boldsymbol{E} \times \boldsymbol{B}$ drift. On the other hand, the ion and electron drifts parallel to the electric field are given by

$$\boldsymbol{v}_{0xe} = -\frac{\nu_{en}}{\Omega_e} v_H \hat{x} \tag{2.5}$$

$$\boldsymbol{v}_{0xi} = \frac{\nu_{in}}{\Omega_i} v_H \hat{x} \tag{2.6}$$

Particle drift along the electric field is called the Pedersen drift. Figure 2.1 illustrates the relative strength of the Hall and Pedersen drifts of ions and electrons in the F region. As shown, the ions and electrons move together with the same Hall drift in the "*y*" direction. Thus the relative velocity between ions and electrons perpendicular to the electric field is zero ($\boldsymbol{v}_{0yi} -$

$\boldsymbol{v}_{0ye} = 0$). In the "x" direction, though, the ions move with the Pedersen drift while the electrons have a very small Pedersen drift in the negative "x" direction. This implies that there is an ion-electron relative drift along the direction of the electric field as

$$\boldsymbol{v}_{0xi} - \boldsymbol{v}_{0xe} \approx \frac{\nu_{in}}{\Omega_i} v_H \hat{x} \tag{2.7}$$

This relative Pedersen drift of ions and electrons plays a crucial role in the formation of the GDI in the F region.

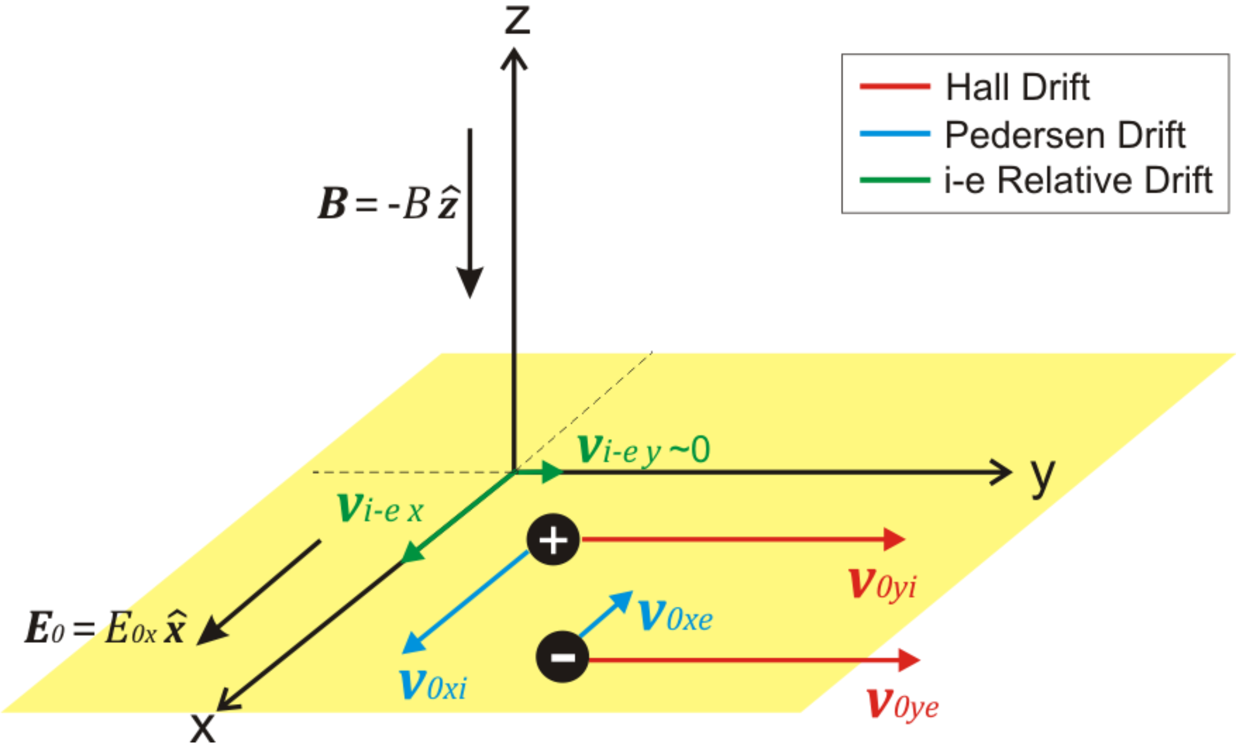

Figure 2.1: Background electric and magnetic fields and vector components of plasma motion in the high-latitude F-region ionosphere.

2.2 Formation of the GDI in the F region

The GDI in the F-region plasma occurs when there is $\boldsymbol{\nabla} n_{0\alpha}$ preferably in the direction of the $\boldsymbol{E}_0 \times \boldsymbol{B}$ drift. To explain the reason for the instability we can consider two blob-shape regions; one with enhanced electron density and another with depleted density, Fig. 2.2a. Due to the difference between Pedersen drift of ions and electrons, a charge separation can occur in the blobs as shown in Fig. 2.2a. This charge separation would lead to a polarization electric field $\delta\boldsymbol{E}$

that causes a $\delta\boldsymbol{E} \times \boldsymbol{B}$ drift. This drift moves the enhanced (depleted) blob of the plasma in the negative (positive) direction of $\boldsymbol{\nabla} n_{0\alpha}$ toward regions with lower (higher) background plasma density. These oppositely-directed motions of enhanced and depleted density blobs create a finger-like structure of the electron density. Because the instability is driven by relative ion-electron Pedersen drift, it is often called Pedersen mode of the GDI to distinguish it from similar instability in the E region known as Hall mode. The growth of GDI is well presented in the results from the three-dimensional nonlinear simulations of the GDI, published by *Gondarenko et al.* (2004), Fig. 2.2b.

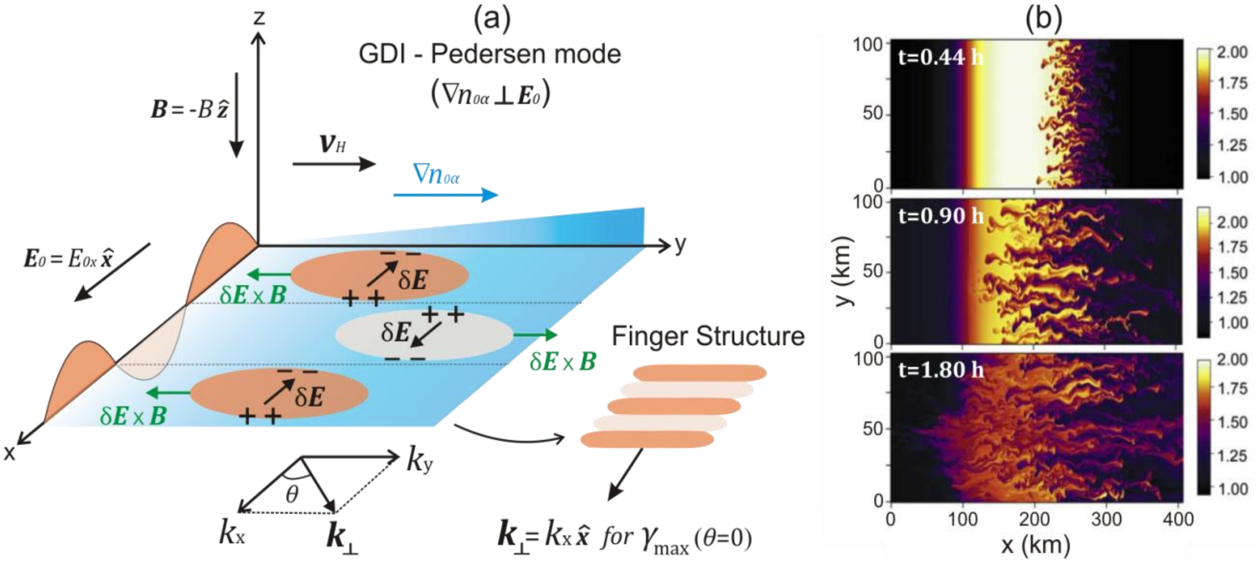

Figure 2.2: (a) Ionospheric configuration for the formation of the gradient-drift instability (GDI) in the F region where dark (light) orange indicates density enhancement (depletion) and blue indicates the background electron density (b) Simulated density contours illustrating the finger structure and the growth of the GDI (*Gondarenko et al.*, 2004).

To compute the growth rate of the GDI, we consider linear perturbation in the plasma density and the electric field ($n_\alpha = n_{0\alpha} + \delta n_\alpha$, $\boldsymbol{E} = \boldsymbol{E}_0 + \delta\boldsymbol{E}$) and neglect non-linear Fourier components of the perturbation. The linear perturbation in the plasma density and the electric field can be written as

$$\delta n_\alpha = e^{\gamma t} \cdot e^{i(\boldsymbol{k}\cdot\boldsymbol{r} - \omega_R t)} \tag{2.8}$$

$$\delta\boldsymbol{E} = -\boldsymbol{\nabla}\varphi = -i\boldsymbol{k}_\perp \delta\varphi \tag{2.9}$$

where ω_R and γ (components of complex angular frequency, $\omega = \omega_R + \gamma i$) are the angular frequency and the growth rate of the perturbation, $\boldsymbol{k}_\perp = k_x \hat{x} + k_y \hat{y}$ is two-dimensional wave vector of the perturbation and φ is the electrostatic potential. The equation of motion, Eq. (2.1), for the perturbed quantities δn_α, $\delta \boldsymbol{E}$ and unknown $\delta \boldsymbol{v}_\alpha$, in absence of neutral wind flows ($\boldsymbol{u}_n = 0$) and collisions between charged particles ($\nu_{ei} = 0$), is given by

$$m_\alpha \frac{d(\delta \boldsymbol{v}_\alpha)}{dt} = -q_\alpha (i\boldsymbol{k}_\perp \delta\varphi + \boldsymbol{\delta v}_\alpha \times B\hat{z}) - m_\alpha \nu_{\alpha n} \delta \boldsymbol{v}_\alpha - i\boldsymbol{k}_\perp \kappa_B T_\alpha \frac{\delta n_\alpha}{n_{0\alpha}} \tag{2.10}$$

where we assumed no perturbation in plasma temperature ($\delta T_\alpha = 0$). Solving the above equation for $\boldsymbol{\delta v}_\alpha$ at quasi-steady state and considering the condition $\nu_{\alpha n} \ll \Omega_\alpha$ yields

$$\delta \boldsymbol{v}_\alpha = -\frac{i\Gamma}{\Omega_\alpha^2}\left[\left(\nu_{\alpha n} k_x + \Omega_\alpha k_y\right)\hat{x} + \left(\nu_{\alpha n} k_y - \Omega_\alpha k_x\right)\hat{y}\right] \tag{2.11}$$

where $\Gamma = -q_\alpha \delta\varphi / m_\alpha + (\kappa_B T_\alpha / m_\alpha)(\delta n_\alpha / n_{0\alpha})$.

Linearizing the continuity equation ($\partial n_\alpha / \partial t + \nabla \cdot (n_\alpha \boldsymbol{v}_\alpha) = 0$) and substituting $\delta \boldsymbol{v}_\alpha$ from Eq. (2.11) gives

$$\mathrm{A}_\alpha \frac{\delta n_\alpha}{n_{0\alpha}} - \mathrm{B}_\alpha \frac{q_\alpha \delta\varphi}{m_\alpha} = 0 \tag{2.12}$$

where $\mathrm{A}_\alpha = i(\boldsymbol{k}_\perp \cdot \boldsymbol{v}_{0\alpha} - \omega) + \frac{\nu_{\alpha n}}{\Omega_\alpha^2}\frac{\kappa_B T_\alpha}{m_\alpha} k_\perp^2$, $\mathrm{B}_\alpha = \frac{\nu_{\alpha n}}{\Omega_\alpha^2} k_\perp^2 + \frac{1}{L}\frac{i}{\Omega_\alpha} k_x$, $k_\perp^2 = k_x^2 + k_y^2$ and $1/L = \boldsymbol{\nabla} n_{0\alpha} / n_{0\alpha}$ is the scale of the plasma density gradient.

One can consider Eq. (2.12) for ions ($q_i = +e$) and electrons ($q_e = -e$)to form a system of equations. Assuming $\delta n_i / n_{0i} = \delta n_e / n_{0e}$, the resulting system of equations has a non-trivial solution when its determinant is zero. This leads us to the following dispersion equation

$$\mathrm{A}_e \mathrm{B}_i + \frac{m_i}{m_e} \mathrm{A}_i \mathrm{B}_e = 0 \tag{2.13}$$

We assume that the growth rate is small as compared to the frequency of the perturbation wave ($\gamma \ll \omega_R$). Then solving real part of Eq. (2.13) for γ yields (after substituting the values for A_α and B_α)

$$\gamma = \frac{1}{L}\frac{k_x}{k_\perp^2}\frac{\Omega_i}{\nu_{in}}\boldsymbol{k}_\perp \cdot (\boldsymbol{v}_{0i} - \boldsymbol{v}_{0e}) - \frac{\nu_{en}}{\Omega_e \Omega_i}\frac{\kappa_B (T_i + T_e)}{m_i} k_\perp^2 \tag{2.14}$$

where the conditions $\Omega_\alpha \gg \nu_{\alpha n}$ and $m_i \gg m_e$ have been taken into account.

In Section 2.1 it was shown that in the F region, the ion-electron relative Hall drift is zero while the ion-electron relative Pedersen drift is given by Eq. (2.7). This means $\boldsymbol{k}_\perp \cdot (\boldsymbol{v}_{0i} - \boldsymbol{v}_{0e}) = (\nu_{in}/\Omega_i)\, k_x v_H$ and the above equation for γ reduces to

$$\gamma = \frac{v_H}{L}\cos^2\theta - D_\perp k_\perp^2 \tag{2.15}$$

where $\theta = \cos^{-1}(k_x/k_\perp)$ is the azimuthal angle between the wave vector $\boldsymbol{k}$ and the electric field $\boldsymbol{E}_0$, $D_\perp = (\nu_{en}/\Omega_e\Omega_i)\, C_s^2$ is the cross-field diffusion coefficient and $C_s = \sqrt{\kappa_B(T_i + T_e)/m_i}$ is the ion-acoustic speed.

Equation (2.15) shows that the growth rate of the GDI is proportional to the magnitude of the Hall drift and plasma density gradient. It also implies that the GDI has its maximum growth rate along the direction of electric field where $\theta = 0$ ($\boldsymbol{k}_\perp \equiv \boldsymbol{k}_x$).

An important aspect of GDI is the fact that the conditions for the instability becomes impossible to satisfy as the perturbation wave vector goes off the perpendicular to the magnetic field. Calculations, similar to shown above, but for three-dimensional wave vector of the perturbation $\boldsymbol{k} = \boldsymbol{k}_\perp + \boldsymbol{k}_\parallel$ ($\boldsymbol{k}_\parallel \equiv k_z\,\hat{z}$) and two-dimensional electric field $\boldsymbol{E}_0 = E_0\cos\zeta\,\hat{x} + E_0\sin\zeta\,\hat{y}$ give the following three-dimensional expression for the growth rate (*Keskinen and Ossakow*, 1982)

$$\gamma = \frac{-\cos\theta\,\frac{\nu_{ei}}{\Omega_e}\frac{1}{L}\left(\frac{\nu_{in}}{\Omega_i}\frac{E_0}{B}\cos(\theta - \zeta) - \frac{k_\parallel}{k_\perp}v_d\right)}{\left(\frac{k_\parallel}{k_x}\right)^2 + \frac{\nu_{ei}\nu_{in}}{\Omega_e\Omega_i}} - D_\perp k_\perp^2 - D_\parallel k_\parallel^2 \tag{2.16}$$

where $D_\parallel = C_s^2/\nu_{in}\{1 + [(\nu_{in}/\Omega_i)^2/((\nu_{ei}\nu_{in}/\Omega_e\Omega_i) + (k_\parallel/k_\perp)^2)]\}$ is the field-aligned diffusion coefficient and $\boldsymbol{v}_d$ is the relative ion-electron velocity along the magnetic field. One can notice that in absence of field-aligned component of perturbations ($\boldsymbol{k}_z = 0$) and parallel component of electric field along the density gradient ($\zeta = 0$), Eq. (2.16) reduces to Eq. (2.15). For the electric field perpendicular to the density gradient, the maximum growth rate occurs for $\theta = 0$ ($\boldsymbol{k}_\perp \equiv \boldsymbol{k}_x$) and Eq. (2.16) reduces to

$$\gamma_{max} = \frac{-\frac{\nu_{ei}}{\Omega_e}\frac{1}{L}\left(\frac{\nu_{in}}{\Omega_i}v_H - \xi v_d\right)}{\xi^2 + \frac{\nu_{ei}\nu_{in}}{\Omega_e\Omega_i}} - D_\perp k_x^2 - D_\parallel k_\parallel^2 \tag{2.17}$$

where $\xi \equiv k_\parallel/k_x$. Equation (2.17) shows that growth rate is a function of ξ. Using $(\partial\gamma_{max}/\partial\xi)_{\xi=\xi_{max}} = 0$, one can obtain the value of ξ for γ_{max} as follows

$$\xi_{max} = \frac{\nu_{in}v_H}{\Omega_i v_d} \pm \sqrt{\left(\frac{\nu_{in}v_H}{\Omega_i v_d}\right)^2 + \left(\frac{\nu_{ei}\nu_{in}}{\Omega_e\Omega_i}\right)} \tag{2.18}$$

Substituting typical F-region parameters $\nu_{in}/\Omega_i \approx 10^{-4}$, $\nu_{en}/\Omega_e \approx 10^{-4}$,$E_{0x} \approx 10$ mV/m, $B \approx 0.5$ G, $j_\parallel = en_0 v_d \approx 1$ μA/m^2 and $n_0 \approx 10^5$cm^{-3} into Eq. (2.18) gives $|\xi_{max}| \approx 10^{-4}$, i.e. $k_\parallel \ll k_x$. This means that plasma irregularities are well-oriented along the magnetic field lines.

The growth of plasma perturbations governed by the GDI will eventually stop when nonlinear effects emerge. It is accepted that as the perturbation increases its amplitude, the energy can be transferred to those perturbations that are linearly stable. This process is called the mode coupling. Computer simulations showed that this is indeed an efficient process allowing co-existence of numerous wave trains in the plasma. These are the irregularities that can be detected by HF radars.

2.3 Power of echoes scattered from ionospheric irregularities

The theory of radio wave scattering by the ionospheric plasma irregularities was developed by *H. Booker* in 1956. In general case, he assumed a linearly polarized radiation from a transmitter of power P is scattered from a volume V of the medium where there are irregularities. He calculated the backscattered power per unit solid angle, per unit incident power density, and per unit volume (σ) as

$$\sigma = \langle\left|\frac{\delta\varepsilon}{\varepsilon}\right|^2\rangle \frac{\pi^2 \sin^2\Theta}{\lambda^4}\ \mathrm{P}(l,m,n) \tag{2.19}$$

where ε is the permittivity of the medium, Θ is the angle between the direction of scattering and the direction of the electric field at the point of scattering, λ is the transmitted radio wavelength and $\mathrm{P}(l,m,n)$ is the Fourier transform of the autocorrelation function of $\delta\varepsilon/\varepsilon$.

Equation (2.19) implies that backscattered power is proportional to mean square fractional deviation of ε. For the radio waves in the ionosphere, the dielectric constant is related to the refractive index as $n = \sqrt{\varepsilon/\varepsilon_0}$. The refractive index for radio waves to a first approximation is

$$n^2 = 1 - \left(\frac{\omega_p}{\omega}\right)^2 \tag{2.20}$$

where $\omega_p = \sqrt{n_{0e}e^2/\varepsilon_0 m_e}$ is angular plasma frequency and ω is the angular frequency of the incident radio wave. Applying this expression to Eq. (2.20), gives

$$\langle|\delta\varepsilon/\varepsilon|^2\rangle = (1/\pi^2)\, r_e^2\lambda^4\langle|\delta n_e|^2\rangle \tag{2.21}$$

and expression for σ

$$\sigma = \langle|\delta n_e|^2\rangle\, r_e^2 \sin^2\Theta\, \mathrm{P}[2\pi/\lambda\,(l, m, n)] \tag{2.22}$$

where $r_e = \mu_0 e^2/4\pi m_e$ is the classical electron radius and δn_e is the perturbation in electron density associated with the plasma irregularities.

Equation 2.22 indicates that the power of coherent echoes is proportional to mean square of δn_e or fluctuation level of ionospheric irregularities. There are other factors. For example, the term P depends on wavelength of irregularities and geometry of measurements, such as the angle with respect to the plasma flow and the aspect angle. These dependencies are very difficult to assess both theoretically, by looking at the development of the GDI, or experimentally. This lack of knowledge limits progress in the field.

The fact that the power of echoes depends on the intensity of electron density fluctuations has a very important implication. A number of rocket measurements (e.g., *Kelley et al.*, 1973; *Ogawa et al.*, 1976; *Schlegel*, 1992) indicated that under typical ionospheric conditions, the quantity $\delta n_e/n_{0e}$ is about several percent. If this is true in the entire range of ionospheric parameters, then one can conclude that the power of coherent echoes is proportional to the square of the mean electron density in the scattering volume because sigma can be written as

$$\sigma \propto n_{0e}^2 \cdot \langle\left|\frac{\delta n_e}{n_{0e}}\right|^2\rangle \tag{2.23}$$

This conclusion implies that the power of echoes would increase whenever the ionosphere is more dense. This means that one can infer the absolute values of density from the coherent radar data. Such an attempt was successful for VHF E-region echoes (e.g., *Williams et al.*, 1999; *Uspensky et al.*, 1988). For HF echoes that are to be considered in this thesis, the conclusion should be treated as a hypothesis that requires experimental confirmation.

2.4 Occurrence of F-region HF coherent echoes: A journey to history

The fact that coherent echoes can be received not only from the E region, but from the F region as well has been known since early 1950s (*Peterson et al.*, 1955). However, the work on F-region echoes has not been as intense as on the E-region echoes. Perhaps one reason is that, to detect F-region echoes, the radio waves need to undergo significant ionospheric refraction to achieve orthogonality with the Earth's magnetic field and thus be scattered by field-aligned irregularities. This can only be done with radars operating at HF frequencies (5-30 MHz) so that relatively cheap, and more widely used for the airplane detection, VHF radars cannot be used. This Section gives historical overview of the major steps in acquiring knowledge on the F-region HF echo occurrence.

2.4.1 Pre-SuperDARN work

Since the first HF radar systems were located at middle latitudes, earlier reports were on observations at these latitudes.

Mid-latitude HF radars

Weaver (1965) used a 14 MHz radar located at Ithaca, N.Y. He reported maximum of echo occurrence in March (75% of the time in the evening sector). Minimum of occurrence was during summer time; the echoes also showed up later in the day during summer months. These results are in accord with the pioneering report by *Peterson et al.* (1955). It was noticed that with an electron density increase, the echoes appear at shorter ranges. *Hower et al.* (1966) noted a decrease in echo occurrence during the declining phase of the solar cycle. While looking from Washington, D.C. area at 12 and 18 MHz, they reported 80% of evening echo detection in

December 1958 and only 35% in December 1963. The data though were contaminated with E-region echoes. *Baggaley* (1970) used 17.3 MHz radar near Sheffield, UK and found that F-region echoes occur mostly during local evening hours, near the sunset time, and last on average 4 hours (his Fig. 2). The echo occurrence rates were found to be smaller than in other reports. This was attributed to the fact that the observations covered 1964-1966 which is the period of the minimum in solar activity.

Möller (1974) used two frequency-sweeping sounders (2.8-45 MHz) at Lindau, Germany (MLAT = 52.4°) and Alsbjerg (MLAT = 57.5°). He reported F-region echo occurrence in 2 latitudinal belts, one corresponding to the poleward edge of mid-latitude trough and the other to the auroral oval. The first belt exists only in the midnight sector, while the second covers all MLTs. The auroral zone belt is centered at higher MLATs during near noon hours (up to 78°) as compared to the midnight hours (68°-70°). The belt shifts towards smaller latitudes summer time. With magnetic activity increase, the auroral zone belt expands to the lower latitudes: for example, during winter near noon hours, the magnetic latitudes of echo detection shifts from $\sim$78° to $\sim$74° as K_p magnetic index changes from 1 to 4.

Auroral zone radars

One of the best cited papers on high-latitude F-region coherent HF echoes is the study by *Bates* (1960) who investigated records of sweep-frequency (1-25 MHz) sounder at College, Alaska and identified directly-detected signals from the F region that were common during winter time. Their occurrence favored magnetically quiet time when the radio wave absorption was minimized. The author noticed that with sunrise the echoes disappear. *Bates* was one of the first researchers who hypothesized that the solar radiation eliminates the irregularities. *Bates and Albee* (1970) estimated that the power of auroral zone HF echoes decreases with the magnetic aspect angle with a rate of $\sim$5 dB per degree indicating that the echoes have high magnetic aspect sensitivity. The result means that HF echoes are detected limited in range/latitude for a particular radar because the propagation must lead to good magnetic aspect sensitivity and the better occurrence over a limited range (or latitude) interval.

Turunen and Oksman (1979) employed a frequency-sweep sounder similar to the one of *Möller* (1974) but located at Nurmijarvi, Finland (GLAT=60.5°). The frequency ranges were from 2 to 32 MHz. They noticed predominant echo occurrence during evening hours and an astonishingly rare echo occurrence during morning hours. The authors related the effect to strong radio wave absorption during these hours. The authors compared their F-region data with the data on E-region irregularities observed by a 144 MHz radar at a close location. The similarity in general morphology of occurrence of E- and F-region echoes was noticed for the latitudes of the auroral oval.

2.4.2 SuperDARN era

Introduction of the SuperDARN radars in early 1990s provided opportunity to study echo occurrence rates at various latitudes and various longitudinal sectors. From the beginning of operation, it was clear that occurrence rates depend strongly on the latitude of monitoring and the magnetic local time (Fig. 18 of *Greenwald et al.*, 1995).

Mid-latitude radars

Detection rates of F-region SuperDARN echoes at middle latitudes are small; this is easily recognizable by considering data of the SuperDARN website. So far, no systematic study of their occurrence has been done.

Hosokawa and Nishitani (2010) presented MLAT-MLT distribution for the Hokkaido radar echo detection in April 2008. Their plots (e.g., Fig. 4) give reasonable sense of the echo occurrence at MLATs=45°-65°. It should be mentioned that this was an exceptional month in terms of echo occurrence; numbers for other months are typically smaller (*Koustov et al.*, 2008b). The plots show that the echoes occur mostly during pre-midnight hours equatorward of the auroral oval. The rates are as high as 10% near the oval and decrease to below 5% at MLATs $< 55°$. The echoes near the oval correlate with the sunset and this sense the data fully agree with earlier findings by *Baggaley* (1970). We note that rates of echo occurrence at MLATs $< 55°$ are often difficult to assess because all the echoes have low velocities and some ionospheric echoes often misidentified by the currently employed data processing technique as ground scatter (*Greenwald et al.*, 2006).

Auroral zone radars

Milan et al. (1997) investigated 20 months (March 1995 - October 1996) of data from the CUTLASS HF radars in Finland. They found that during winter, the Hankasalmi radar echoes at MLAT=80° are mostly detected during day time with two local maxima, one during pre-noon hours and another one during post noon hours. The maxima appear to become more separated in terms of time towards summer time. These echoes were thought to be received through one and half hop propagation mode. During summer, F-region echoes were mostly observed during daytime through the direct mode and at lower latitudes. Enhanced echo occurrence rate was shown to be consistent with increased ionospheric electron density that is suggested to be a key factor for echo detection.

Ruohoniemi and Greenwald (1997) considered echo occurrence rates for the Goose Bay SuperDARN radar in the period of 1988-1993. They presented magnetic local time-magnetic latitude diagrams of echo occurrence for various months and seasons over a half of the solar cycle. The clear conclusion was that the auroral zone echoes occur more frequently at solar cycle maximum and during winter. The lack of echoes during the summer was interpreted as the result of solar radiation (for the sunlit ionosphere) smoothing out the plasma gradients necessary for the production of irregularities (exciting the GDI).

Huber (1999) explored Saskatoon radar data for 1997 and reported that F-region echoes in winter are mostly detected in two time sectors, one at near noon hours and the other one later in the afternoon, close to the dusk (18 MLT) sector. The near noon echoes virtually disappear during other seasons while pre-dusk echoes show up at later MLTs during equinox and even later time during summer.

Ballatore et al. (2001) considered multiple SuperDARN radars and found that for the period of 1997-1998 (close to the solar cycle 22 minimum), echoes were more frequently seen at magnetic latitudes of 65°-80° with the rates of ∼7% during winter, ∼5% during equinox, and ∼3% during summer. They also found that there is a statistically significant correlation between northern hemisphere SuperDARN radar echo occurrence and negative IMF B_z values, independent of season.

Danskin (2003) focused on the midnight F-region echoes and found that these echoes are more frequent during winter for the solar activity maximum periods. For the solar cycle minimum, echo occurrence was higher during the summer months. This feature was interpreted as a consequence of low typical density in the F region leading to unsatisfactory conditions for the ray bending.

More systematic investigation of auroral zone F-region echo occurrence has been undertaken by *Hosokawa et al.* (2001) who considered data from six Northern hemisphere radars operated in 1996-1998 (again, close to the solar cycle 22 minimum) and showed that echoes mostly occur on the dayside at magnetic latitudes of 70°-75° corresponding to the poleward edge of the auroral oval or even poleward of it. In other MLT sectors, echoes were collocated with the auroral oval. It is interesting to note (this was not mentioned in the original paper) that the two Iceland radars (Pikkvibaer and Stokkseyri), whose FoVs are oriented azimuthally, detected a significant amount of echoes not only at the auroral oval latitudes but also from within the polar cap, at MLATs=70°-80°. Such echoes were preferentially seen in the afternoon sector all the way until early morning. *Hosokawa et al.* (2001) focused on dusk echoes seen well equatorward of the auroral oval. These were related to the mid-latitude trough.

Koustov et al. (2004) considered near midnight F-region echo detection rates by a number of radars in both southern and northern hemispheres. The authors showed that for many radars there is a strong seasonal variation with clear maxima near equinoxes. The effect was very evident for the southern hemisphere radars. It was suggested that stronger electric fields, on average, over equinoctial time are the main factor for the equinoctial echo occurrence maxima, which is consistent with the preferential conditions for IMF merging with the Earth’s magnetic field as suggested by *Russel and McPherron* (1973).

Parkinson et al. (2003) considered one year (1999-2000) of echo statistics for the Australian SuperDARN radar at Bruny Island. The echoes were found to dominate in the midnight sector at somewhat poleward of the auroral oval. With the K_p index increase, more echoes were seen equatorward of the auroral oval. It was noticed existence of a March (fall) maximum though the overall seasonal variation was apparently not significant. *Koustov et al.* (2006) investigated occurrence of King Salmon HF radar echoes near the equatorward edge of the auroral oval and reported preferential occurrence in the dusk-midnight sector. The Hokkaido mid-latitude radar also detects this sort of echoes (*Koustov et al.*, 2008).

Another interesting class of echoes occurring equatorward of the auroral oval, and this sense classifiable as mid-latitude echoes, are the ones first reported by *Ruohonimei et al.* (1988)

during afternoon hours. These were related to the onset of mid-latitude through with its highly inhomogeneous distribution of F-region electron density. *Hosokawa et al.* (2002) found that similar type of echoes can be seen during morning hours.

SuperDARN echoes from within the polar cap

SuperDARN echo occurrence at extreme high latitudes, say MLATs $>$ 80°, has been of interest from the very beginning of SuperDARN project. With earlier radars, echoes here can only be received through 1½-hop propagation mode (the HF propagation mode nomenclature is given in Subsection 3.1.6). This means that propagation conditions would be a major factor in echo detection. The situation changed with installation of two PolarDARN radars. The radars showed echo occurrence rates much higher than the concurrently operating auroral zone radars.

Fiori et al. (2009) reported that PolarDARN echoes occur predominantly at relatively short ranges, with MLATs $<$ 85°. It was clear that consideration of the electron density and propagation conditions is very important in understanding reasons for echo detection at these latitudes. *Liu* (2010) assessed PolarDARN echo occurrence with respect to the Saskatoon radar echo detection. He showed that echo detection rates for RKN are ∼5-30%, depending on season and magnetic latitude, while for the Saskatoon radar the rates are ∼1%-10%. Overall, for the respective most favourable echo detection latitudes (these are different due to significant separation of the radars in latitude) the RKN detects ∼3 time more echoes than Saskatoon radar. Another finding was a strong decrease of RKN echo during summer. Seasonal effect in RKN echo detection is also recognizable in the data presented by *Prikryl et al.* (2010). *Ponomarenko et al.* (2010) presented data on RKN scatter for beams 0, 7 and 15. The data indicate that fewer echoes are detected in beam 15 while there are comparable number of echoes in beams 0 and 7. The effect has not been discussed and investigated further.

Recently, a new extreme high-latitude radar was installed by the University of Alaska at Antarctic McMurdo station (*Bristow et al.*, 2011). Its magnetic latitude is $\Lambda = 80°$, so that this radar can detect echoes over the south magnetic pole. The radar shows very high echo occurrence rates, perhaps even higher than those for the RKN and INV radars. The data show that over the southern magnetic Pole the number of echoes drops down dramatically once the radar moves into the dark ionosphere. This finding is consistent with very early HF work by *Baggaley* (1970) emphasizing the role of sunlight on the propagation of radio waves.

2.5 Factors controlling occurrence of F-region HF echoes from previous studies

Ionospheric conditions that lead to creation of ionospheric decameter irregularities and their detection with HF radars were a subject of limited number of publications. Work in this direction is significantly hampered by the fact that there are no means to continuously monitor ionospheric parameters within the FoV of SuperDARN radars.

Milan et al. (1997) compared Hankasalmi echo occurrence with critical frequencies recorded by the Sodankyla ionosonde located about 600 km away in the radar position. They concluded that the electron density of $2 \times 10^5\ \mathrm{cm}^{-3}$ is needed to detect echoes at F-region ranges. *Milan et al.* (1999) had data on the electron density and electric field (from the EISCAT incoherent scatter radar) within the Hankasalmi radar scattering volume at ~ 900 km. The authors, not surprisingly, reported that echoes occur for non-zero electric field, and as a general rule, a 5-mV/m threshold was mentioned. They also indicated that after the substorm onset, when very strong ionization is created in the E region, the blanketing effect is responsible for the F-region echo disappearance. Finally, they considered the potential effect of enhanced diffusion in the F region due to enhanced conductance of the E-region plasma. They showed that the factor $M = 1 + \Sigma_{\mathrm{P-F}}/\Sigma_{\mathrm{P-E}}$ (a measure of the relative contributions of the F and E regions to the Pedersen height-integrated conductance) controls the echo power. This is expected as the GDI development in the F region can be slowed down (or even prevented) when perturbation electric field of unstable modes gets shorted out through the highly conducting E region (*Vickrey et al.*, 1982). Finally, the authors emphasized the fact that enhanced D-region absorption can lead to disappearance of echoes.

Danskin et al. (2002) had more extensive Hanksalmi HF radar – EISCAT data set. They concluded that most of echoes occur for electric field > 10 mV/m and electron density of $2.5 \times 10^5\ \mathrm{cm}^{-3}$ is indeed a typical value for echo detection over the EISCAT spot. The data also supported the conclusion by *Milan et al.* (1999) that the effect of E-region conductance might be an important factor. Very recently *Kumar et al.* (2011) considered data of the Australian TIGER radar and electron density of Macquarie Island ionosonde located about 1600 km away from the radar. Although the target of the study was the occurrence of echoes at various stages of magnetic storm, the data clearly indicate that F-region electron density enhancements correlate with significant enhancement of echo occurrence at the main phase of the storm.

Conclusion

No study has achieved a global synthesis of the effects of latitudinal, magnetic local time, seasonal and solar cycle variations on the radar scattering process.

CHAPTER 3

INSTRUMENTS

In this Chapter we describe operation principles of two types of radar systems to be used in this thesis, a coherent SuperDARN radar and a CADI digital ionosonde.

3.1 SuperDARN radars

3.1.1 General characteristics

A SuperDARN backscatter radar is a system transmitting a sequence of radio pulses and receiving them on the same antennae. It operates at HF frequencies of 8-20 MHz with a peak power of 10 kW. The pulse sequence is designed in such a way that echo detection from multiple ranges, including over the horizon distances, is possible. Currently used an 8-pulse sequence is shown in Fig. 3.1. The numbers in the diagram (0, 14, 22, 24, 27, 31, 42, 43) are multiplies of the pulse lag time of $\tau = 2.4$ ms. The length of each pulse is 0.3 ms providing range/gate resolution of 45 km. an antenna array of 16 antennas is phased to radiate in 16 "beam" directions with angular spacing of 3.24° in azimuth between successive beam positions. The first returned signals are received from the range gate of 180 km; this initial range gate is assigned gate number zero (R_0). Since the length of each range gate is 45 km, the gate number n corresponds to the range of $R_n = 180 + n \cdot 45$ (km) away from the radar. Typically, the radars cover 75 range gates along each beam position. Then the last range gate is located at $R_{74} = 3510$ km away from the radar. For each beam position, the ~ 36 (or ~ 72) computed complex autocorrelation functions (ACFs) are integrated and averaged to increase the signal-to-noise ratio. Typically, there are about 60 pulse sequences averaged for each beam position for a 2-minute scan of the 16 beams, or 30 pulse sequences for a 1-minute scan. The amplitude and phase of the scattered signal are measured so that the ACF can be determined. The parameters of a radio echo such as the backscattered power, the Doppler velocity and the spectral width are then inferred from collected ACFs.

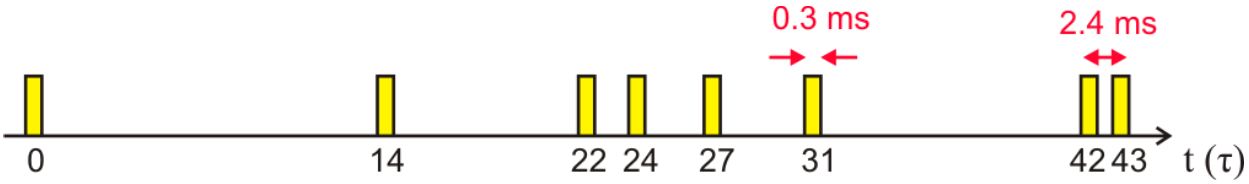

Figure 3.1: SuperDARN normal 8-pulse scheme.

3.1.2 ACF Technique

To explain the concept of the ACF technique to measure Doppler velocity, we consider a 2-pulse sequence with the pulse lag time τ, as shown in Fig. 3.2. We want to measure how much the scattering plasma at desired distance d_0 has moved during lag time τ. We assume that the first (second) pulse is transmitted at time t_0 ($t_0 + \tau$). The pulse 1 is scattered at the distance $d_0$with amplitude of $A_1(d_0)$and returned to the receiver at time $t_1 = t_0 + 2d_0/c$. The pulse 2 is scattered back at the distance d_- with amplitude of $A_2(d_-)$ and arrived to the receiver at the same time t_1. Therefore, the total echo amplitude measured at t_1 is given by

$$A(t_1) = A_1(d_0) + A_2(d_-) \tag{3.1}$$

On the other hand, at the time $t_1 + \tau$ the pulse 1 arrived from a distance d_+ with the amplitude of $A_1(d_+)$ and the pulse 2 arrived from a distance d_0 with amplitude of $A_2(d_0)$. Then the amplitude of total received signal at $t_1 + \tau$ is given by

$$A(t_1 + \tau) = A_1(d_+) + A_2(d_0) \tag{3.2}$$

Therefore, the mean ACF of the signals at lag τ can be written as

$$\begin{aligned}\langle A(t_1) \cdot A(t_1 + \tau)\rangle = \langle A_1(d_0) \cdot A_2(d_0)\rangle + \langle A_1(d_0) \cdot A_1(d_+)\rangle +\\ \langle A_2(d_-) \cdot A_1(d_+)\rangle + \langle A_2(d_-) \cdot A_2(d_0)\rangle\end{aligned} \tag{3.3}$$

The above equation shows that the ACF for lag τ contains four terms, but only the first term originates from the same distance d_0. Terms 2, 3 and 4 include signals received from different ranges; such signals are expected to not correlate, which means that in Eq. (3.3) the terms 2, 3 and 4 should average to zero. In order to minimize the effect of uncorrelated terms on the resultant ACF measurements, the SuperDARN radars transmit the pulse sequence many times and compute the mean ACF of received signals. Since terms 2, 3 and 4 are contributions of uncorrelated signals from different distances, they can be neglected in the mean ACF. Equation (3.3) then reduces to

$$\langle A(t_1)\cdot\ A(t_1+\tau)\rangle\ \approx \langle A_1(d_0)\cdot A_2(d_0)\rangle \tag{3.4}$$

The ACF from above equation can be written in terms of its amplitude A_m and phase φ as follows

$$\langle A(t_1)\cdot\ A(t_1+\tau)\rangle\ \approx A_m e^{i\varphi} \tag{3.5}$$

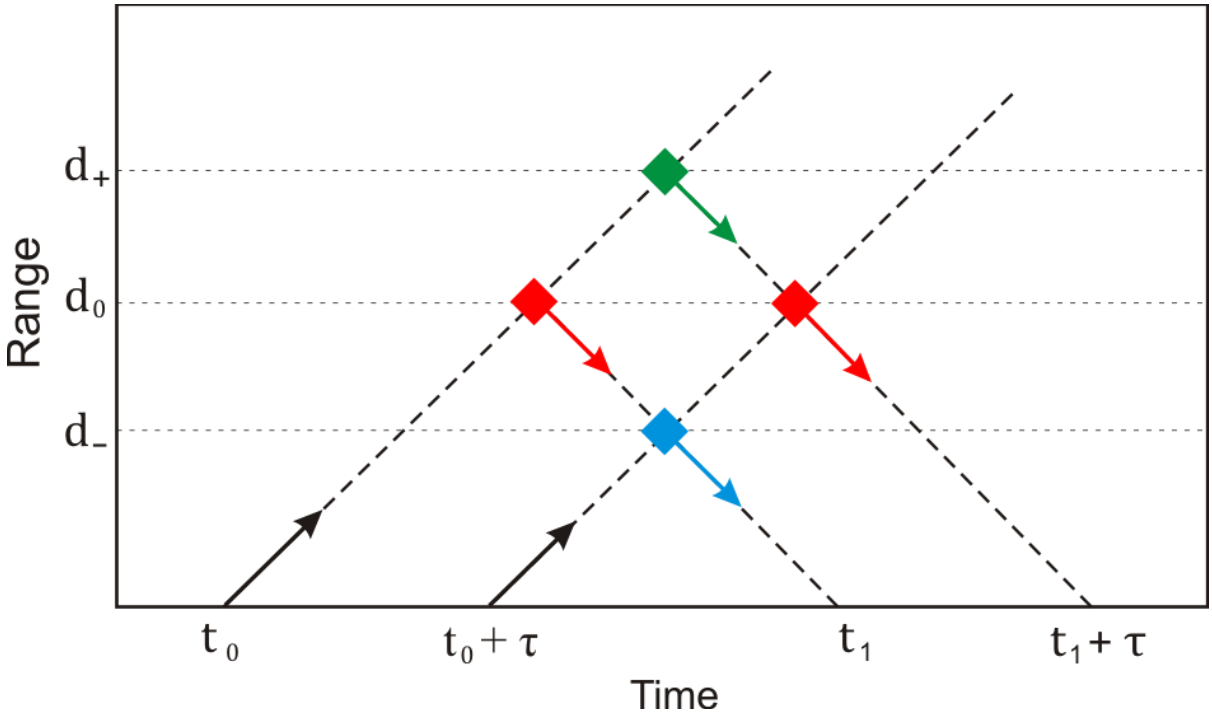

Figure 3.2: Range-time diagram for the 2-pulse sequence.

The measurements of the phase when a radar transmits a 2-pulse sequence are not as precise as compared to a multiple-pulse sequence transmission. In addition, it is impossible to determine the spectral width of backscattered signal by transmitting 2-pulse sequence. That is why the SuperDARN radars use a multiple-pulse sequence (currently 8-pulse) with different values of τ (Fig. 3.1). Then, as it is shown in Fig. 3.3a, the ACF can be determined at a sufficient number of time lags and the phase of the ACF at each time lag can be is given by

$$\varphi = \tan^{-1}\left(\frac{Im(ACF)}{Re(ACF)}\right) \tag{3.6}$$

An example of a plot for the phase as a function of time lag is presented in Fig.3.3b. As shown, the phase varies linearly with time lag between 4π. This information is sufficient for inferring the Doppler shift of the echo.

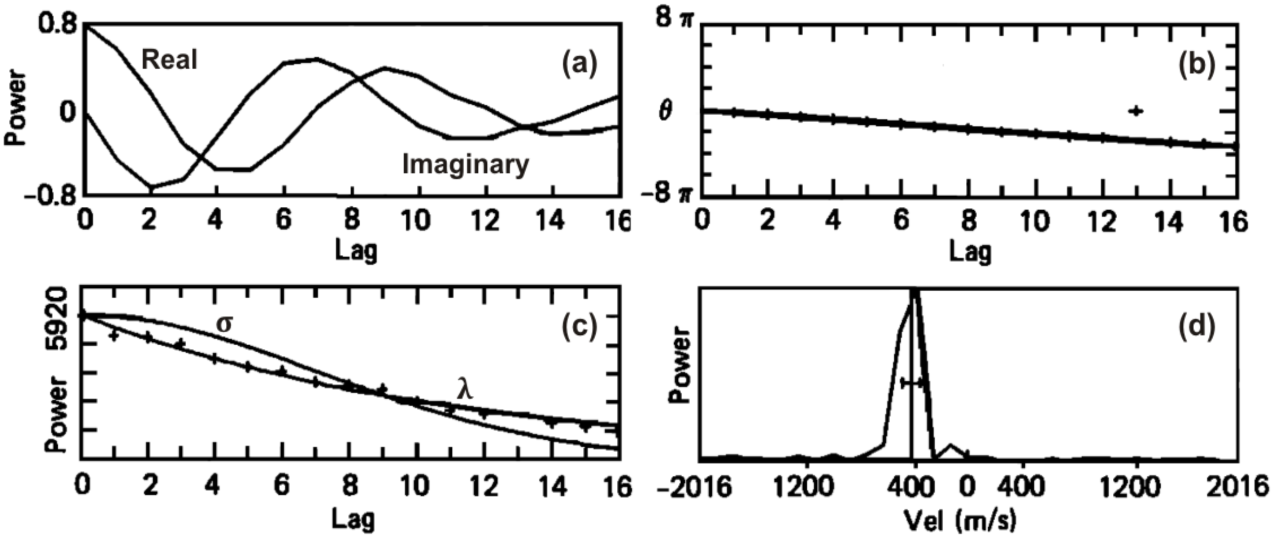

Figure 3.3: (a) The real and imaginary parts of the ACF versus time lag (b)The phase of the ACF versus lag number (c) FITACF power in the Lorentzian $P_{\lambda}(\tau) = P_{\lambda m}e^{-\lambda k\tau}$ and Gaussian $P_{\sigma}(\tau) = P_{\sigma m}e^{-(\sigma k\tau)^2}$ least-square fits (d) Fourier transform of the ACF with velocity (vertical line) and spectral width (horizontal line) obtained using Lorentzian FITACF (*Villain et al.*, 1987).

3.1.3 Doppler shift measurements and computing the Line-of-Sight velocity

Principle of the LoS Doppler velocity derivation from the measurements of phase of the ACF is illustrated in Fig. 3.3c. The mean Doppler shift in terms of the phase of the ACF at the time $m\tau$ (where k is the set of integers) can be written as

$$\langle \omega_D \rangle = \frac{\varphi_k}{m\tau} \tag{3.7}$$

where φ is given by Eq. (3.6). The Doppler velocity in terms of the Doppler shift frequency can be written as (*Schiffler,* 1996)

$$v_P = \pm \frac{c\langle \omega_D \rangle}{4\pi\, f_T} \tag{3.8}$$

where $\langle \omega_D \rangle = 2\pi f_D = 2\pi(f_R - f_T)$ is the mean Doppler shift angular frequency that is inferred from ACF slope analysis, Eq. (3.6). We note that since the motion of plasma irregularities at high latitudes is close to the convection (Hall drift) $\boldsymbol{v}_H$, the SuperDARN radars detect the LoS component of $\boldsymbol{v}_H$.

3.1.4 Fitting technique to compute the backscattered power and spectral width

Figure 3.3a shows that the real part of the ACF is maximized at lag number zero and as lag number increases, the ACF decays. This is because as the time lag between signals increases, the signals become less correlated. Considering measured amplitude at lag number zero (where the Imaginary part of the ACF is zero) is one of the possible ways to determine the backscattered power (P_0). We can also use the Lorentzian or Gaussian least-square fits of the ACF (Fig. 3.3c) to determine the backscattered power. The Lorentzian FITACF is presented by a Lorentzian function with the decay constant λ as follows

$$P_\lambda(\tau) = P_{\lambda m}\, e^{-\lambda k \tau} \tag{3.9}$$

where $P_{\lambda m}$ (maximum power) specifies the maximum Lorentzian backscattered power (P_λ). This is the power of the Lorentzian FITACF at time lag $\tau = 0$. On the other hand, the Gaussian FITACF is presented by a Gaussian function with the decay constant σ as follows

$$P_\sigma(\tau) = P_{\sigma m} e^{-(\sigma k \tau)^2} \tag{3.10}$$

where $P_{\sigma m}$ (maximum amplitude) specifies the maximum Gaussian backscattered power (P_σ). This is the power of the Gaussian FITACF at time lag $\tau = 0$. Therefore we have three approaches to determine the backscattered power: 1) Measuring the power of real part of the ACF at $\tau = 0$ where Imaginary part is zero, 2) Measuring the Maximum power of the Lorentzian

FITACF (P_λ) at time lag $\tau = 0$ and 3) Measuring the Maximum power of the Gaussian FITACF (P_σ) at time lag $\tau = 0$. In this thesis, P_λ is used to present the Polar/SuperDARN backscattered power.

The spectral width of backscattered signal can be obtained by using the Wiener-Khinchin theorem. According to this theorem, the Fourier transform of the ACF yields the power spectrum of the backscattered signal in terms of the velocity. Then the full width at the half maximum power specifies the spectral width of the backscattered signal. In the case of the Lorentzian FITACF, Eq. (3.9), the Lorentzian spectral width (Δv_λ) obtained from the Wiener-Khinchin theorem can be written as

$$\Delta v_\lambda = \frac{\lambda c}{2\pi f_T} \tag{3.11}$$

For the Gaussian FITACF, Eq. (3.10), the Gaussian spectral width ($\Delta \omega_\sigma$) is given by

$$\Delta v_\sigma = 2\sqrt{\ln 2}\,\frac{\sigma c}{2\pi f_T} \tag{3.12}$$

Figure 3.3d shows an example of the Fourier transform of the ACF with velocity (vertical line) and spectral width (horizontal line) where the Lorentzian least-square fit is considered. Experimentally, it is established that the F-region (E-region) ACF is well represented by the Lorentzian (Gaussian) function (*Villain et al.*, 1996).

3.1.5 Interferometry technique to measure elevation angle of echo arrival

The elevation angle is the angle of arrival of the returned signal with respect to the ground. The knowledge of the elevation angle is important for determination of the ionospheric region where the backscattered signal comes from. *Ponomarenko et al.* (2011) applied the elevation angle data to determine the critical plasma frequency of the F layer and then the background electron density of the ionospheric F region where the signal is scattered from.

In order to measure the elevation angle, the SuperDARN radars use an additional interferometry array in combination with the main array. The main array is comprised of 16 antennas that transmit and receive the radio signals while the interferometer array consists of only 4 receiving antennas. The method of the elevation angle measurements is explained in Fig.

3.4. At elevation angle ϕ the backscattered signals received by the main and interferometer arrays have a path length difference of $\Delta x = d\cos\theta$, where d ≈100 m is the distance between the two arrays. Since the phase shift due to this path length difference is $\Delta\varphi = (2\pi/\lambda)\,\Delta x$, then ϕ can be written as

$$\phi = \cos^{-1}(\frac{\lambda}{2\pi d}\Delta\varphi) \tag{3.13}$$

The phase shift can be determined by measuring the time difference between backscattered signals received by the main and interferometer arrays. Then the elevation angle can be obtained from Eq. (3.13).

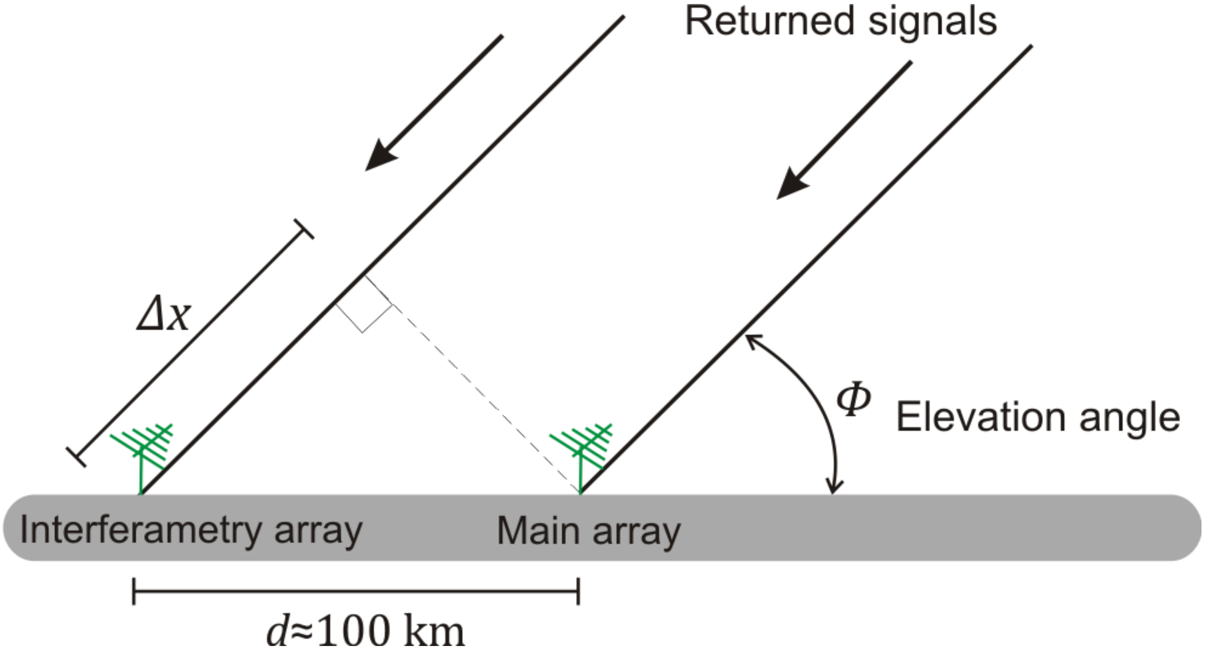

Figure 3.4: The geometry of interferometry technique to measure the elevation angle.

3.1.6 Propagation modes of SuperDARN radio waves in the ionosphere

Radio waves in the HF band can propagate for long distances in the Earth ionosphere. This is possible due to the effect of refraction that causes bending of the radio waves propagating through the ionosphere. In a simplest approximation the ionosphere can be considered as comprised of several thin layers with different refractive index (Fig. 3.5). Since the electron density increases with height up to the F region, plasma frequency also increases and as a result the refractive index, given by Eq. (2.20), becomes smaller. Therefore the path of the radio wave becomes more horizontal to the earth's surface and the reflection of the radio wave can eventually occur. At this level, applying the Snell's law to the boundary of layers, results $n = \sin i_0$ (where i_0 is the angle of the incident wave from the zenith as it enters the ionosphere). Substituting this equation into the Eq. (2.20) yields the required condition for reflection as

$$\omega_p = \omega \cos i_0 \tag{3.14}$$

For vertical incidence $i_0 = 0$, the plasma frequency of the medium equals the radio frequency of the wave at the reflection level. For $\omega_p > \omega$, the refractive index becomes imaginary and the wave is vanished. Therefore, the reflection occurs where $n = 0$.

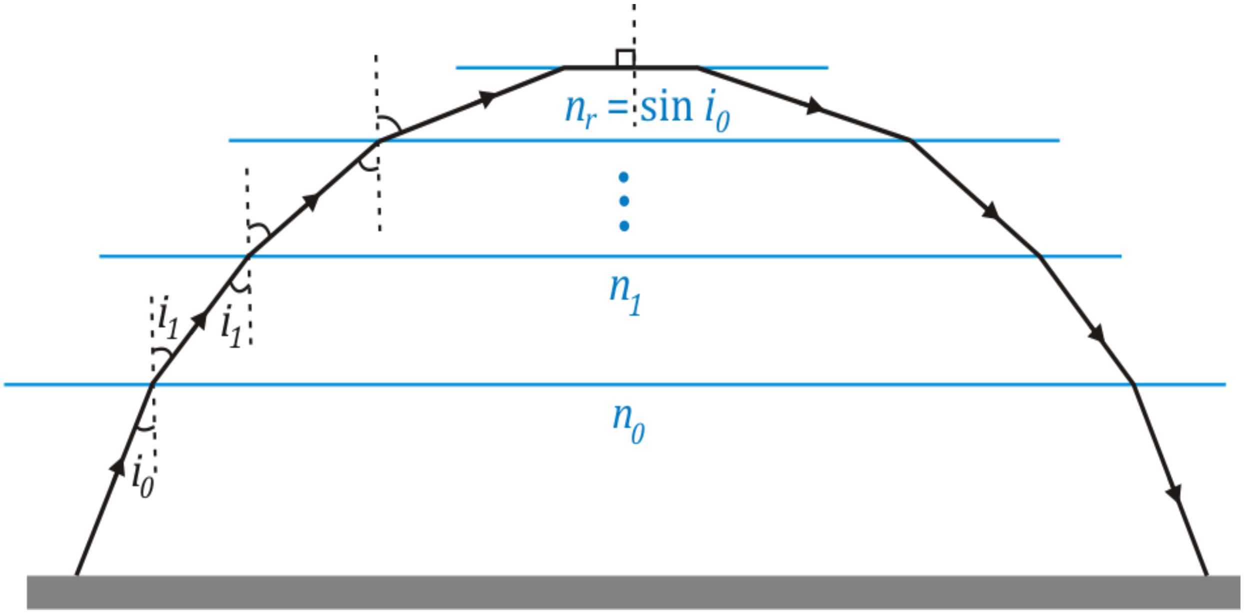

Figure 3.5: A cartoon explaining reasons for strong bending of HF radio waves in the ionosphere.

Figure 3.6 shows possible trajectories of radio HF waves in the ionosphere and their classification. The ½E- and ½F-hop propagation modes are direct ionospheric backscatter from the E and F regions. Ionospheric echoes can also be received through the 1½E- and 1½F-hop propagation modes where the radio waves are reflected by the ground before and after scattering from the E and F regions. The ground scattered signals can be detected through the 1E-, 2E-, 1F- and 2F-hop propagation modes as they are shown in Fig. 3.6.

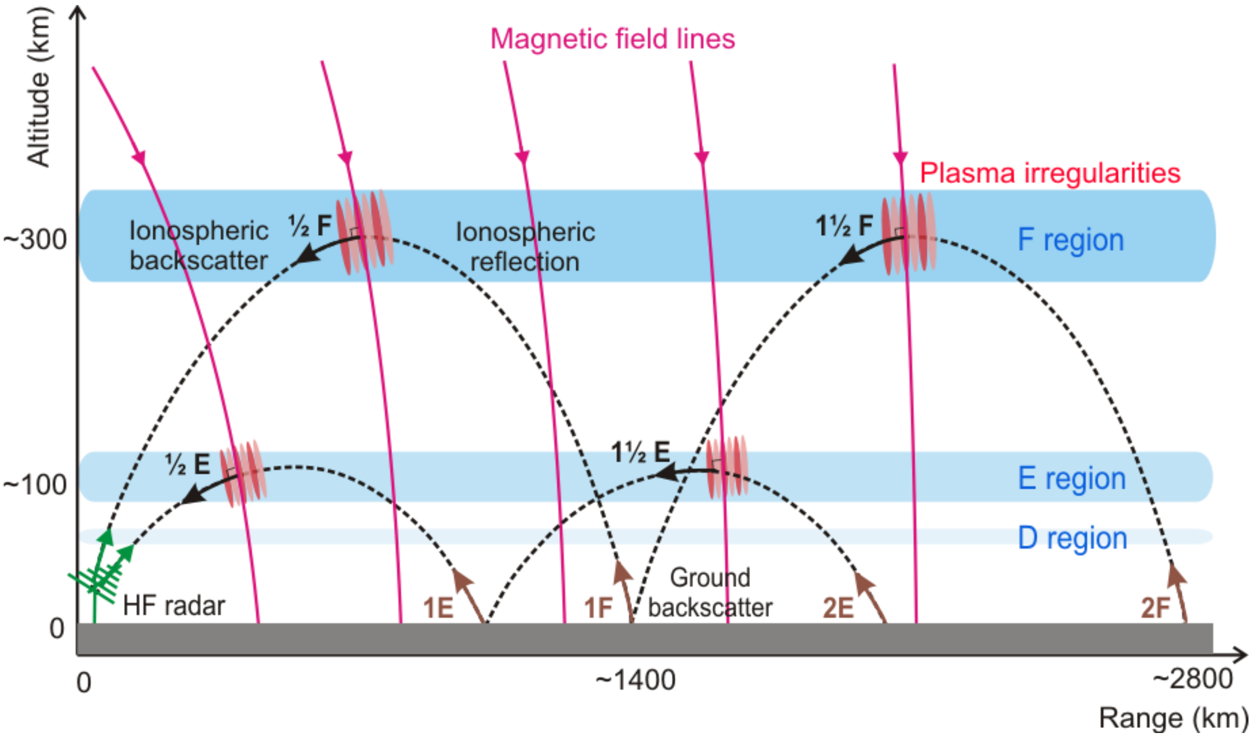

Figure 3.6: Propagation modes of the HF radio waves in the ionosphere.

3.2 CHAIN CADI operation

The CADI instruments are designed to measure electron density profiles in the ionosphere and plasma flow vector in the zenith of a station. The CHAIN network is currently comprised of the five operational digital ionosondes that are at very high latitudes, mostly within the polar cap. The location of CADIs is shown by yellow triangles on the map in Fig. 1.9. The network was established for collaborative experiments with other instruments such as the SuperDARN radars and optical imagers.

CADI consists of one transmitter and four receivers. The transmitting antenna is a delta antenna, and the receiver antenna array consists of four dipoles along the centres of the four sides of a square. The peak pulse power of the transmitter is 600 W. The pulse coding for CADI is a 7/13-bit Barker code. CADI operates in the HF band of 1-20 MHz and has a height coverage range of 90-1024 km with 6-km resolution. The primary CADI products are the ionograms with up to 1-min resolution and the electric field (plasma convection) vector with 30-s resolution. In the following, we describe how the electron density of the F2 peak and the electric field at F-region heights can be determined from CADI observations.

3.2.1 Ionograms: critical frequency and computing maximum electron density

An ionosonde operates on the principle of total reflection of radio waves from ionospheric layers. It transmits radio wave pulses vertically into the ionosphere and measures the echo delay time Δt. Therefore the height of reflection, by assuming that the pulse travels at the speed of light c, equals to $h = c\Delta t/2$. This height is called the virtual height. In reality, for the high-frequency approximation the pulse travels with the group velocity of $u_g = nc$. Since the refractive index is smaller than one, the pulse travels more slowly than speed c. Therefore, the real height of reflection is lower than the virtual height.

In the absence of the magnetic field, the refractive index is given by Eq. (2.20) where the plasma frequency ω_p^2 is proportional to the background electron density n_{0e}. From the typical density profile in the ionosphere (Fig. 1.4) we know that the electron density increases with height and reaches its peaks in the E- and F-region heights. Therefore the plasma frequency increases and the refractive index becomes smaller as height increases. For $\omega_p > \omega$, the refractive index is imaginary and the radio wave cannot penetrate deeper into the ionosphere. Thus the total reflection of the radio wave occurs where the plasma frequency equals the frequency of the transmitted signal, i.e. $\omega_p = \omega$. The maximum of the frequency at which the reflection occurs is called the critical frequency of the layer. The ionosonde sweeps in the frequency between 1 and 20 MHz, but only signals with the frequency less than the critical frequency of the reflecting layer are detected by the receiver. At each transmitted frequency, the virtual height of a reflecting layer can be found from the delay time of the echoes. The result of these two measurements is represented on an ionogram where the virtual height is displayed as a function of the transmitted frequency. The real height profile can be inferred by taking the refraction index into account.

An example of Resolute Bay CADI ionogram that illustrates the critical frequency of the F2 layer is shown in Fig. 3.7. One interesting feature of this ionogram is that there are two close traces of echo and two corresponding values for the critical frequency. This is due to the existence of the magnetic field. Considering the presence of magnetic field in the Appleton-

Hartree equation (*Hargreaves*, 1992) yields two values for the refractive index. Therefore, the radio waves propagate at two different speeds and there are two different modes called ordinary (*O*) and extraordinary (*E*) modes. Further calculation gives simple relation between the critical frequency and the electron density for these two modes as follows

O-mode: $$f_{cr} = 8.98\sqrt{n_{0e}} \qquad (3.15)$$

E-mode: $$f_{cr} = 8.98\sqrt{n_{0e}} + 0.5\,\Omega_e \qquad (3.16)$$

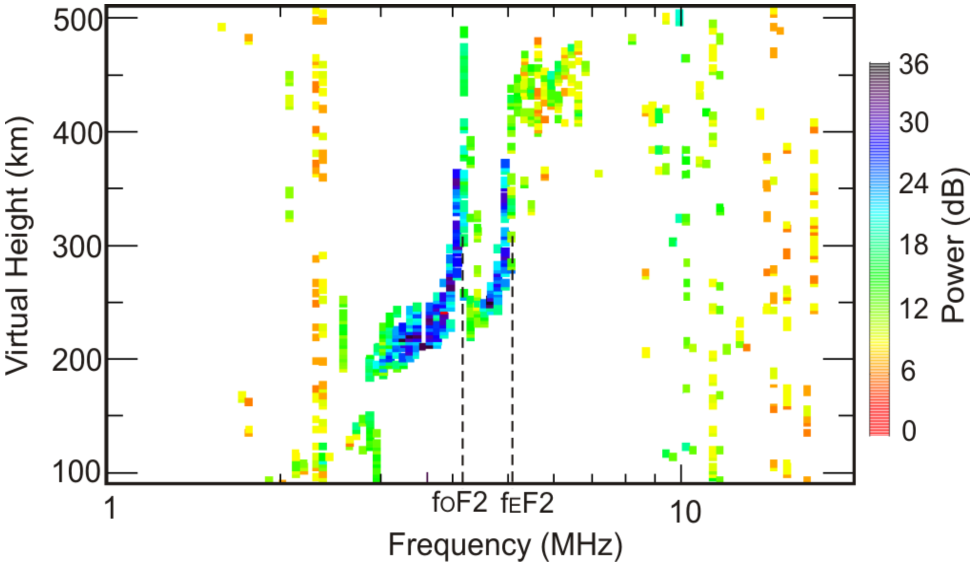

Figure 3.7: RB CADI ionogram on 01 July 2010 at 18:00 UT. The symbols foF2 and fEF2 denote the ordinary and extraordinary critical frequencies of the F2 layer.

The CADIs produce one minute resolution ionograms and determine the critical frequency of the reflecting layer. In this study we use the ordinary critical frequency data provided by the RB CADI to determine the background electron density maximum, Eq. (3.15). The result is used in Section 5.1 to investigate the effect of the electron density on occurrence of F-region echoes over RB.

3.2.2 Measuring convection (Hall drift) using CADI

In addition to the sweep-frequency measurements (ionograms), CADIs use the fixed frequency measurements to determine the Doppler shift, the angle of arrival and the echo power of individual reflectors in the ionosphere. The fixed-frequency measurements are done every 30 s at the frequency of ~3, 4, 5 and 6 MHz. The Doppler shift can be determined from the rate of change of the ACF phase by the same method described in Subsection 3.1.2. Angles of arrival are measured in two different directions. First one is the angle east of the north-south (N-S) meridian plane, θ_E, and the second one is the angle north of the east-west (E-W) vertical plane, θ_N. In other words, θ_N and θ_E are the off-zenith angles in the N-S and E-W directions. These angles can be measured by the interferometry technique that we described in Subsection 3.1.4. Angles of arrival and the measured Doppler shift for each reflector are plotted as a skymap. Figure 3.8a illustrates the principle of the Doppler shift measurements by CADI ionosondes. A sample of skymap from measurements of the angle of arrival and the Doppler shift is shown in Fig. 3.8b.

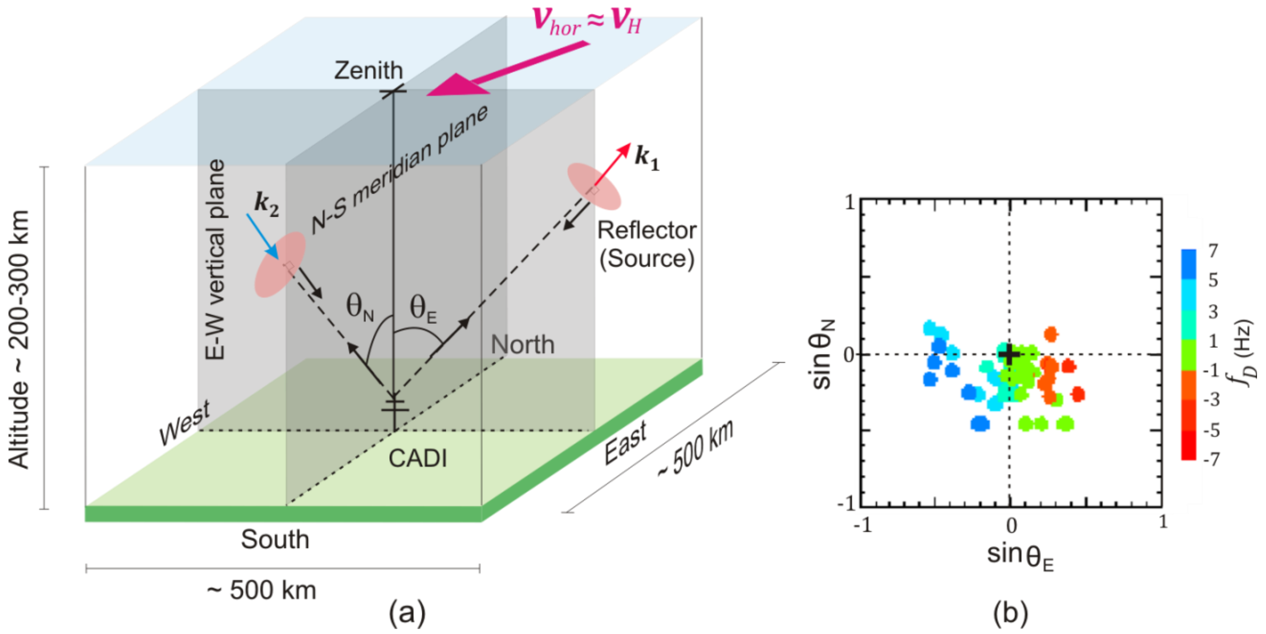

Figure 3.8: (a) The geometry of convection measurements by CADI ionosondes (b) RB CADI skymap on 01 January 2005 at 22:00 UT.

Information on angles of arrival is used to determine the exact arrival direction of the wave vector $\boldsymbol{k}$ that is oriented from each reflector toward or away from the ionosonde. Therefore three components (N-S, E-W and vertical) of the plasma velocity can be computed by minimizing the difference between measured and assumed velocity vector

$$\sum_{s=0}^{n}[w_s\left(f_{Ds}-\frac{\boldsymbol{v}_H\cdot\boldsymbol{k}_s}{\pi}\right)]^2 \tag{3.17}$$

where w is the echo power in logarithmic scale known as source weight, f_D is the Doppler shift, $\boldsymbol{v}_H$ is the assumed convection vector, $\boldsymbol{k}$ is the wave vector and the index s indicates the source number.

Since the vertical component of CADI velocity vector is almost along the equipotential magnetic field lines in the polar cap region, the values of this component are small and usually negligible. Therefore the convection velocity in the horizontal plane $\boldsymbol{v}_{hor}$ can be determined by combining the N-S and E-W components. The value of $\boldsymbol{v}_{hor}$ gives us the magnitude of the convection $v_H = E/B$. Finally, the electric field is computed by considering $B \approx 0.5\ \mathrm{G}$ (the typical strength of geomagnetic field at the F-region heights in the polar cap).

In Section 5.2 we will use the RB CADI measured electric fields to investigate the electric field as an irregularity production factor for HF echoes observed by the RKN PolarDARN radar.

CHAPTER 4

TRENDS IN OCCURRENCE OF F-REGION HF ECHOES IN THE AURORAL ZONE AND POLAR CAP

Our first task is to generally assess HF echo occurrence rates for several HF radars. We consider the Rankin Inlet (RKN) and Inuvik (INV) radars, the so called PolarDARN radars, monitoring the polar cap ionosphere and the auroral zone radars Saskatoon (SAS) and Prince George (PGR) monitoring much broader areas in the same sector of Arctic. Although all four radars are part of the SuperDARN initiative, for brevity, we will call the SAS and PGR radars as the SuperDARN radars in contrast to RKN and INV, the PolarDARN radars. All four radars are run by the University of Saskatchewan radar group, and this is one of the reasons we focus on these radars.

In studying echo occurrence rates we pursue two goals. First, we want just to learn more about this phenomenon. The second goal is to test some ideas on the reasons for occurrence of HF coherent echoes. We explained in Chapter 2 that the irregularity production factors and the radio wave propagation factors need to be considered to understand why HF echoes occur. The relative role of these factors for each individual radar or season is a formidable task since simultaneous measurements of many parameters in the radar FoVs are required. These are not available now and in near future. However, some conclusions can be reached in a statistical sense through investigation of the long-term echo occurrence trends (*Koustov et al.,* 2004) or by studying the relationship of echo occurrence with other phenomena such as magnetic storms (*Kumar et al.,* 2011). This is because the power of F-region coherent HF echoes is expected to depend upon the electric field and electron density in the scattering volume (Chapter 2). Both these ionospheric parameters experience seasonal change which should lead to a seasonal variation in echo occurrence as well.

In this Chapter we consider the F-region echo detection rates at various latitudes and magnetic local times. The thrust is on magnetic local time and seasonal trends in echo occurrence. At the end of the Chapter we consider solar cycle variation for the SAS radar, well suited for the task.

4.1 Data selection and approach to processing

The SuperDARN radars at SAS and PGR have been in operation for many years, since 1993 and 2000, respectively. The RKN and INV PolarDARN radars started regular observations in 2006 and 2008, respectively. Although we processed all data collected by the radars, here we present observations for some specific periods to be concise and more clearly articulate our conclusions.

4.1.1 Radar selection

Figure 4.1 shows the FoVs of the PolarDARN/SuperDARN radars in the Western Canadian sector. The RKN and INV radars monitor MLATs of ~75°-90° while the SAS and PGR radars detect echoes starting from MLAT of ~65°. We consider data only from the beams nearly perpendicular to the contours of equal magnetic latitude (beams 4-6 for PolarDARN, 2-3 for SAS and 12-13 for PGR). These selected beams are shown by shaded areas in Fig. 4.1. The meridionally-oriented beams were chosen to reduce the variability in echo occurrence due to different orientation of the beams with respect to the average convection pattern. We will illustrate differences between echo detection rates in various RKN beams later. To have a uniform data set, only observations in the standard operating mode (2-min or 1-min sequential 16-beam scans) were considered. In practice, there were usually ~15 days of measurements for each month.

For each of the radars, the echo occurrence rate was computed as a ratio of the number of registered echoes in every individual radar gate to the total number of observations in this gate over each month. A similar approach was undertaken by *Koustov et al.* (2004). Only ionospheric echoes stronger than 3 dB were counted. Ratios were averaged for each 10 minutes of observations and in 1° magnetic latitude bins. Magnetic local time was computed by taking into account the range and the universal time. In this way, the standard "MLT-magnetic latitude (Λ)" plots of echo occurrence were produced, similar to those reported by *Ruohoniemi* and *Greenwald* (1997).

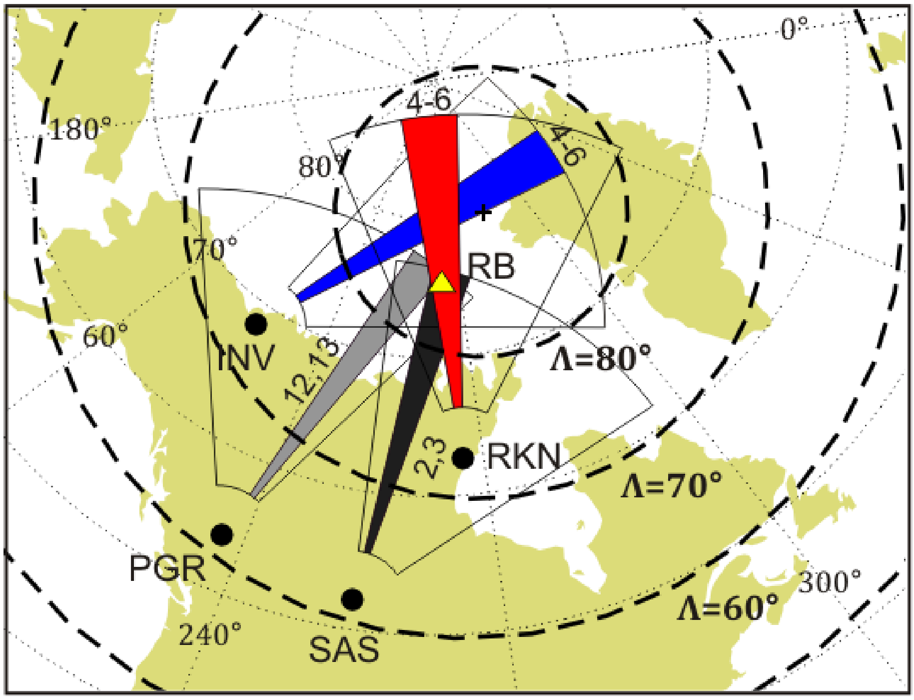

Figure 4.1: Fields of view of four Polar/SuperDARN radars run by the University of Saskatchewan in Western Canada. For each radar, beam positions selected for the analysis are shown by shading. Yellow triangle is the location of the RB CADI ionosonde.

4.1.2 Example of the magnetic local time-magnetic latitude plot

An example of a MLT-Λ plot for the echo occurrence of the PolarDARN radars in January 2010 is given in Fig. 4.2. One can notice similarity of RKN and INV patterns with higher occurrence in a ~6° "belt" of latitudes ~75°-80° and an additional "belt" at latitudes of 80°-85° on the dayside, between about 08:00 and 16:00 MLT. We note here that whenever we say a latitude of, say 80°, it actually means that the data were averaged over 1°-band, i.e. between 79.5° and 80.5°. There were not too many echoes on the nightside for the higher-latitude belt as indicated by uniform blue color on the diagrams. Absolute maxima of echo detection rate for both radars occur during pre-midnight hours of 22:00-23:00 MLT, and RKN shows another strong maximum during near-noon hours. An important feature of Fig. 4.2 is overall occurrence rates on the order of 0.3-0.4, which are significantly higher than what has been reported (for the solar minimum periods) for the auroral zone radars such the SAS radar (*Koustov et al.*, 2004).

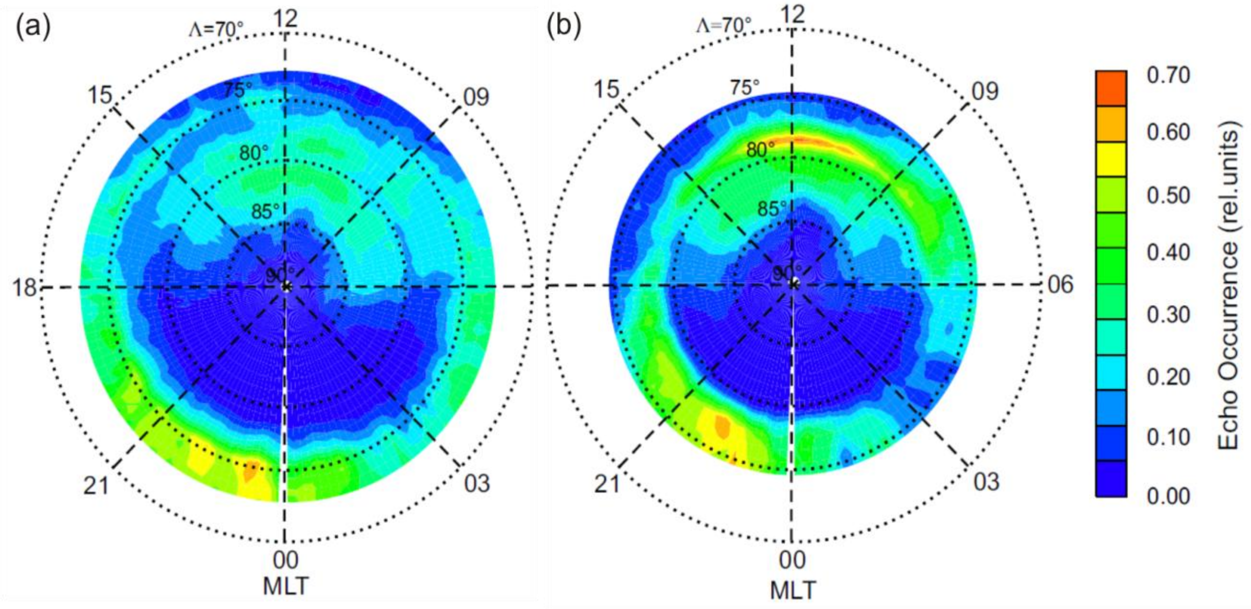

Figure 4.2: Echo occurrence rates (normalized to 1) at various magnetic latitudes and magnetic local times for (a) Inuvik and (b) Rankin Inlet for observations in January 2010. Data in roughly meridionally-oriented beams were considered.

4.1.3 Latitudinal (range) profiles of echo detection

Figure 4.2 indicates that the PolarDARN echoes in January 2010 were frequently detected starting from the shortest radar ranges at MLAT ≈ 75° on the nightside and at MLAT≈77° on the dayside. Since the geomagnetic latitude of the INV is ~1.5° lower than that of the RKN radar, the echo band near boundaries do not coincide implying that care must be taken in selection of the closest latitude of F-region echo detection. We note that at the closest magnetic latitudes one expects mostly E-region echoes, and transition to ranges with purely F-region echo detection is fuzzy; it is a general assumption that F-region echoes occur ~6° of MLAT (10 range gates) away from the radar location (e.g., *Makarevich*, 2010). This would correspond to MLAT=80° for RKN and MLAT=78° for INV.

To analyze the variation of echo occurrence with magnetic latitude, averaged values over 1°-belts of magnetic latitude and 24 hours of MLT were computed, Fig. 4.3. Figure 4.3 plots RKN (red) and INV (blue) echo occurrence rates for observations in January 2010. In Figure 4.2 (and all similar diagrams to follow) we do not show the standard deviation of the occurrence in each bin for clarity of the presentation. The typical standard deviation was 0.12 (0.093) for the RKN (INV) radar. In agreement with color plots of Fig. 4.2, one can see a strong peak in RKN occurrence at MLAT=78°, near the expected far edge of the E-region echo detection. The INV data do not show a sharp peak; instead, a more smooth in latitude distribution is seen with the maximum at MLAT=75°. For latitudes above 80° all the way up to ~90°, both radars detect F-region echoes at comparable rates and both show a steady decrease. For this reason, to compare occurrence rates for the two PolarDARN radars we assigned the latitudes of 80°-85° as the ones representing the ranges with high F-region echo detection rate. We note that MLAT=80° (85°) corresponds to the RKN range of ~900 (~1575) km. We believe most of the echoes at these latitudes are received through ½-hop propagation mode.

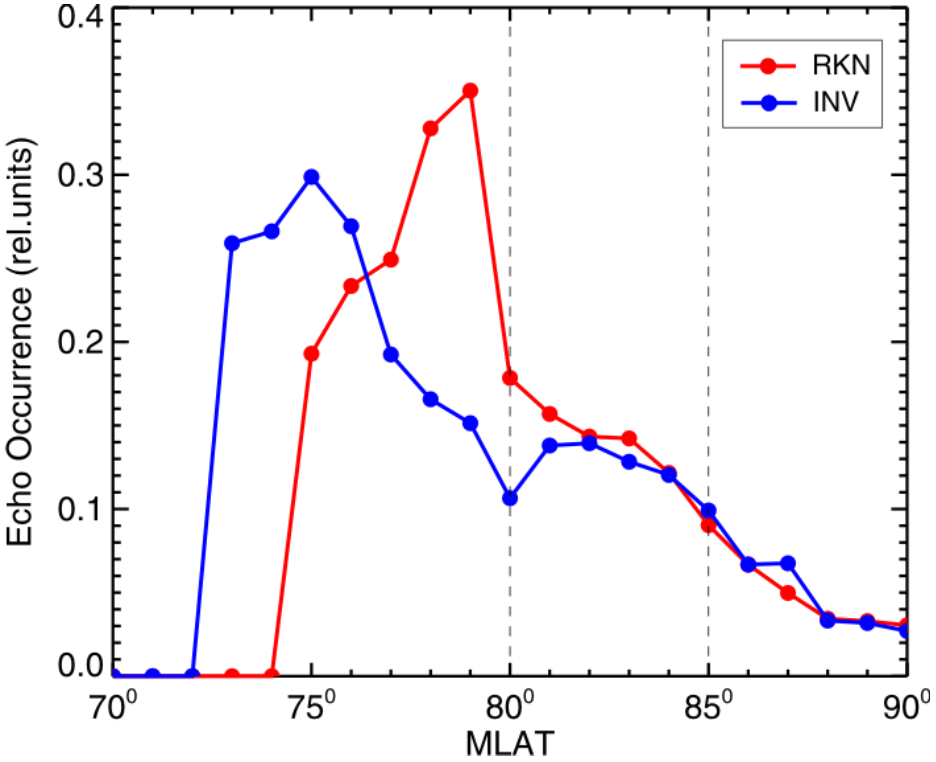

Figure 4.3: Averaged echo occurrence rates at various magnetic latitudes for the INV (blue) and RKN (red) PolarDARN radar observations in January 2010. Vertical dashed lines delineate the band of latitudes with highest F-region echo detection.

Table 4.1 shows average echo occurrence rates over three bands of latitudes (for the data presented in Fig. 4.3). First (second) column refers to RKN (INV) observations. The last column is the ratio of RKN occurrence rate to INV occurrence rate. One can see that in the first band, the RKN radar sees much more echoes but this happens mostly because of predominant E-region echo detection here. At farther ranges, the rates are more comparable, the ratios are closer to one.

Table 4.1: Average (over 24 hours) echo occurrence rates for the INV and RKN PolarDARN radars in January 2010 in three bands of MLATs.

MLAT	RKN	INV	RKN/INV
75º-80º	0.25	0.20	1.25
80º-85º	0.14	0.12	1.17
85º-90º	0.05	0.05	1.00

4.2 Seasonal change in overall echo occurrence

To quantify the occurrence rates for the PolarDARN radars for various seasons, we computed average rates for MLATs between 79.5°-85.5° (for brevity, we denote this as 80°-85°) over 24 MLT and for each month. Figure 4.4 presents obtained values (INV, blue line and RKN, red line) for the year 2010. For simplicity of presentation, here we consider data in 2010. It is notable that the observations in other years, 2007, 2008 and 2009, show the same features as the observations in 2010. The typical standard deviation was 0.057 (0.054) for the RKN (INV) radar. One can see that the average occurrence rates and the trends are remarkably similar. The rates are smallest during summer months and they increase up to maximum values for March and to near the maximum value for September. There is a decrease of the rates towards winter, from March to January, and the rates fluctuate around the September level for the October-December period. Roughly speaking, the difference in echo occurrence rates between summer and winter is a factor of ~2. We note that plots for other years of PolarDARN operation are very much similar to those presented in Fig. 4.4.

Figure 4.4 also shows the average occurrence rate for the auroral zone SuperDARN radars at SAS and PGR (SAS, solid line; PGR, dotted line). The rates were computed in the same way except that 6°-latitudinal bands were selected between 75° and 80°; these are the latitudes with maximum echo occurrence for these radars (*Liu*, 2010). The typical standard deviation was 0.057 (0.054) for the SAS (PGR) radar. The curves for the SAS and PGR radars have broad maxima centered near spring and fall equinoxes. The summer occurrence rates are about 2 times smaller than the rates at equinoxes. One can also realize that the PolarDARN radars detect much more echoes than the SuperDARN radars at SAS and PGR. It is notable that for MLATs=80°-85° the PolarDARN radars are in ½-hop propagation mode while for MLATs=75°-80° the SuperDARN SAS and PGR radars are in 1½-hop propagation mode.

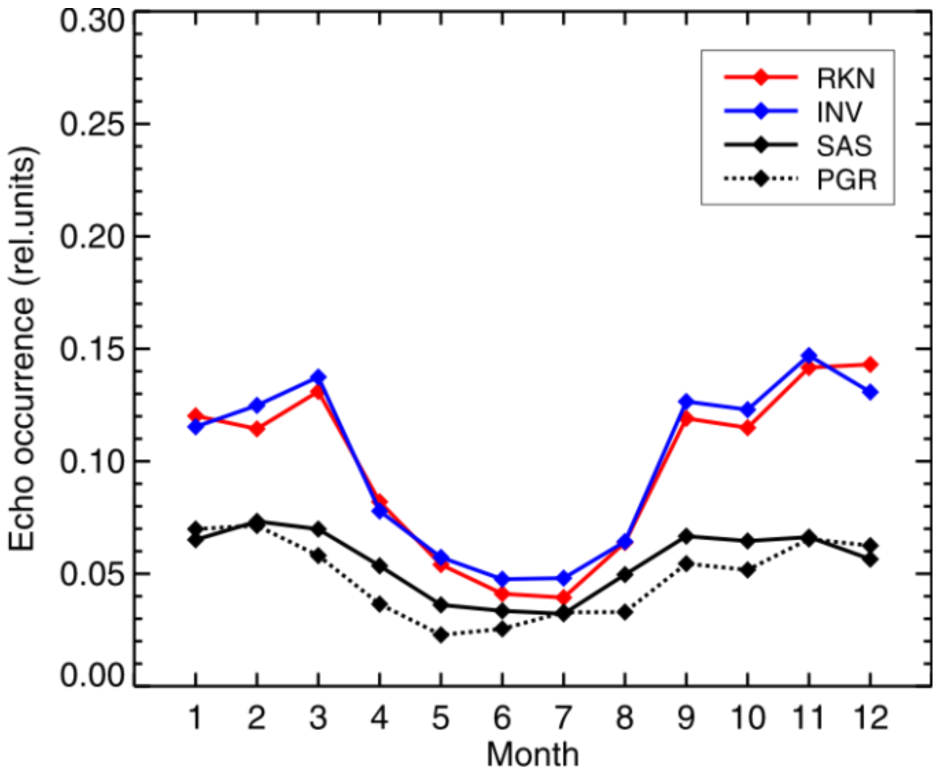

Figure 4.4: Monthly averaged echo occurrence rates over 24 hours between magnetic latitudes of 80° and 85° for the INV (blue) and RKN (red) PolarDARN radars and between magnetic latitudes of 75° and 80° for the SAS (solid line) and PGR (dotted line) SuperDARN radars. 2010 data collected in beams shown in Fig. 4.1 were considered.

To give a sense of differences, we computed average occurrence rates over four seasons, winter (December, January and February), spring equinox (March, April and May), summer (June, July and August) and fall equinox (September, October and November). The data for the SAS and RKN radar are presented in Table 4.2.

Table 4.2: Average (over 24 hours) echo occurrence rates for the RKN and SAS radars and their ratios in four seasons in bands of MLATs with the best echo detection (80°-85° for RKN and 75°-80° for SAS) and the same band of MLATs (80°-85° for both radars).

Season	RKN (80°-85°)	SAS (75°-80°)	SAS (80°-85°)	RKN/SAS (best MLATs)	RKN/SAS (same MLATs)
Winter	0.15	0.06	0.05	2.50	3.00
Spring	0.13	0.07	0.04	1.86	3.25
Summer	0.06	0.04	0.015	1.50	4.00
Fall	0.12	0.06	0.03	2.00	4.00

One can see that the ratio of the rates varies from 1.5 (summer) to 2.5 (winter). We also present in Table 4.2 the ratio of the SAS echo occurrence at magnetic latitudes of 80° and 85° and the RKN echo occurrence at these latitudes, i.e. the ratio for the echo occurrence within the same MLAT echo bands. The ratios here are larger, especially for equinox and summer, which indicates that the PolarDARN radars are more successful, overall, in monitoring echoes in the polar cap. One should notice that for the MLATs=80°-85° the RKN (SAS) radar is in ½- (1½-) hop propagation mode. For MLATs=75°-80° the SAS radar is also in 1½-hop propagation mode.

4.3 Equinoctial maxima in echo occurrence in various MLT sectors

The monthly-averaged data for the SuperDARN radars show the enhanced echo occurrence during equinoxes. This effect for the midnight sector of the auroral zone (SuperDARN radars) was reported by *Koustov et al.* (2004) and one should expect it for the polar cap (PolarDARN radars) as well. The PolarDARN data of Fig. 4.4 show some signatures of the effect but not clearly. This poses a question on the reason for such a difference. One of the potential reasons is that the PolarDARN radars do not show many echoes at MLATs > 80° in the midnight sector (e.g., Fig. 4.2).

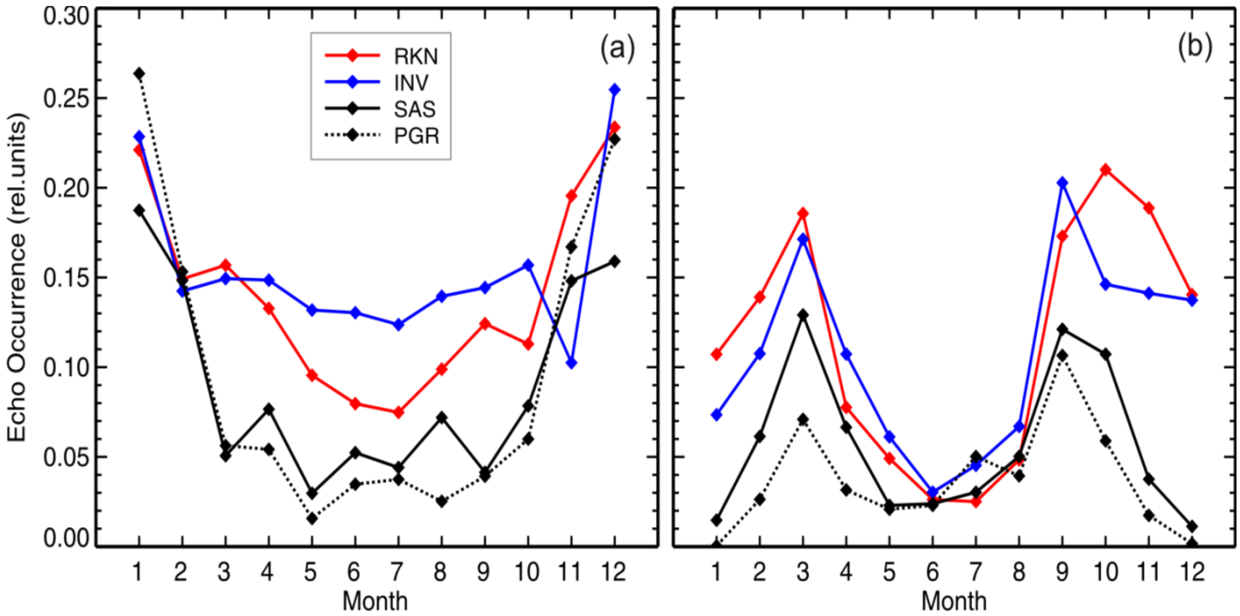

Figure 4.5: Occurrence rates of the PolarDARN INV (blue) and RKN (red) radars and SuperDARN SAS (solid line) and PGR (dotted line) radars for various months of 2010: (a) for the 11:00-13:00 MLT sector and (b) for the 17:00-19:00 MLT sector.

Figure 4.5 shows occurrence rates of the PolarDARN (INV, blue line and RKN, red line) radars and the SuperDARN (SAS, solid line and PGR, dotted line) radars for various months of 2010 in two time sectors, 11:00-13:00 MLT and 17:00-19:00 MLT. For simplicity of presentation, here we consider data in 2010. It is notable that the observations in other years, 2007, 2008 and 2009, show the same features as the observations in 2010. The typical standard deviations for individual bins in the plots here range from 0.015 to 0.026. The dayside data do not show any equinoctial maxima while the data for the dusk sector show them clearly, for all the radars considered. To quantify the strength of the equinoctial maxima effect we considered every 2-hour period of observations and introduced a parameter R:

$$R = \frac{1}{2}\left[\mathrm{OCC}_{\mathrm{EQUINOX}}/\mathrm{OCC}_{\mathrm{SUMMER}} + \mathrm{OCC}_{\mathrm{EQUINOX}}/\mathrm{OCC}_{\mathrm{WINTER}}\right] \tag{4.1}$$

where occurrence rates for various seasons were taken as average for March-April and September-October to represent equinox, June-July to represent summer and December-January to represent winter. This parameter would be largest for the curves that have strongest contrast between occurrence rates in equinox as compared to other seasons (like the ones shown in Fig. 4.4). In absence of the effect, *R* should be close to 1. The results of computations are presented in Table 4.3.

Table 4.3: Parameter R, characterizing the strength of the equinoctial maxima, for PolarDARN (RKN, INV) and SuperDARN (SAS, PGR) measurements in 2-hour periods of magnetic local time. 2010 observations in bands of MLATs with the best echo detection (80°-85° for PolarDARN and 75°-80° for SuperDARN) were considered.

MLT	RKN	INV	SAS	PGR
0-2	3.7	5.5	3.2	3.1
2-4	2.5	4.7	1.5	2.6
4-6	2.6	2.6	3.6	7.0
6-8	1.4	1.4	3.0	2.0
8-10	0.7	0.7	1.2	1.8
10-12	1.0	0.8	0.9	1.0
12-14	1.2	1.0	1.0	0.9
14-16	1.9	1.7	1.5	1.8
16-18	3.2	2.6	3.9	36.5
18-20	3.9	2.8	4.3	13.7
20-22	4.2	4.7	2.5	3.3
22-24	4.0	6.8	5.2	7.3

One can see that the maxima are not recognizable for observations between 06-12-16 MLT (dayside), $R < 2$, and they are obvious for observations between 18-24-06 MLT (nightside), $R > 2$. The large values of R for the PGR radar between 16-20 MLT are because of very low occurrence rates during winter observations.

4.4 Hourly occurrence rates for the Rankin Inlet and Saskatoon radars during the solar minimum period

Data of Fig. 4.2 indicate that occurrence rates depend on magnetic local time. Our next step is to investigate the seasonal and MLT effect in echo occurrence by considering hourly-averaged data, i.e. on a finer temporal scale. Only the RKN and SAS radar data will be presented here; the INV (PGR) data are consistent with RKN (SAS) tendencies to be discussed.

Figure 4.6 shows RKN and SAS echo occurrence rate versus MLT for observations in the period of solar minimum from 2007 to 2010. All the features discussed earlier are recognizable in Fig. 4.6. First, one can clearly see enhanced echo occurrence during winter time. The new feature visible here is predominant occurrence of winter echoes at near noon hours. It is important to realize that at ∼12:00 MLT the central beams of the RKN radar are orientated towards the Sun, i.e. they roughly correspond to the local solar noon. For an individual year, for example between summer of 2009 and summer of 2010 (middle part of the diagram), the March and September (equinox) noon maxima are not as strong as winter time and there are additional "dawn" and "dusk" maxima at ∼06:00 and 18:00 MLT. The pattern of high echo occurrence rate in Fig. 4.6 looks as a "cross" centered around winter noon, for both radars. As season progresses (April-May), the noon maximum weakens, while the dawn and dusk maxima continue to persist. During summer, however, the dawn and dusk maxima disappear so that only near noon echoes are detected by the RKN radar and almost no echoes are detected by the SAS radar. We note that the RKN near noon echo maximum is weakest during summer time. Figure 4.6 thus shows that while echoes are mostly detected for near noon hours during winter and summer months, they are often seen in other time sectors.

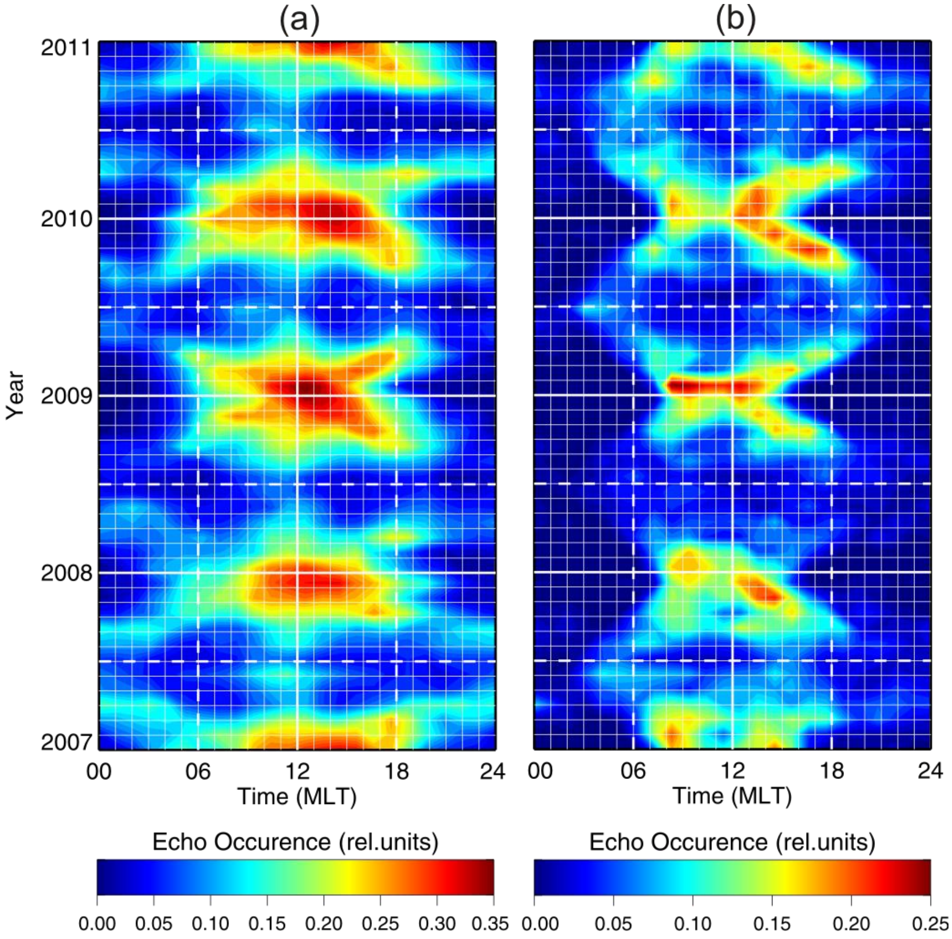

Figure 4.6: (a) RKN and (b) SAS echo occurrence rates versus MLT for various months of 2007-2010. Only data at the magnetic latitudes of best F-region echo detection (80°-85° for RKN and 75°-80° for SAS) were considered.

4.5 Near-noon "depression" in echo occurrence for the PolarDARN radars in December 2009

While investigating plots similar to the ones presented in Fig. 4.6 but for observations in 1° band of latitudes (i.e. on a finer latitudinal scale), we discovered a very interesting feature for observations at near noon winter hours. The effect is demonstrated in Fig. 4.7 where we show occurrence rate (versus MLT) for the RKN and SAS radars in December 2009. The typical standard deviations in individual bins here were 0.05-0.1 for both radars. One can see that around 12:00 MLT, the RKN occurrence rate experiences a minor "depression" at MLAT=83°. The depression lasts for several hours. The SAS occurrence rate, on the contrary, is at maximum during these hours so that the SAS radar, detecting echoes through 1½-hop propagation mode, observes more echoes than the RKN radar detecting echoes through the direct ½-hop propagation mode.

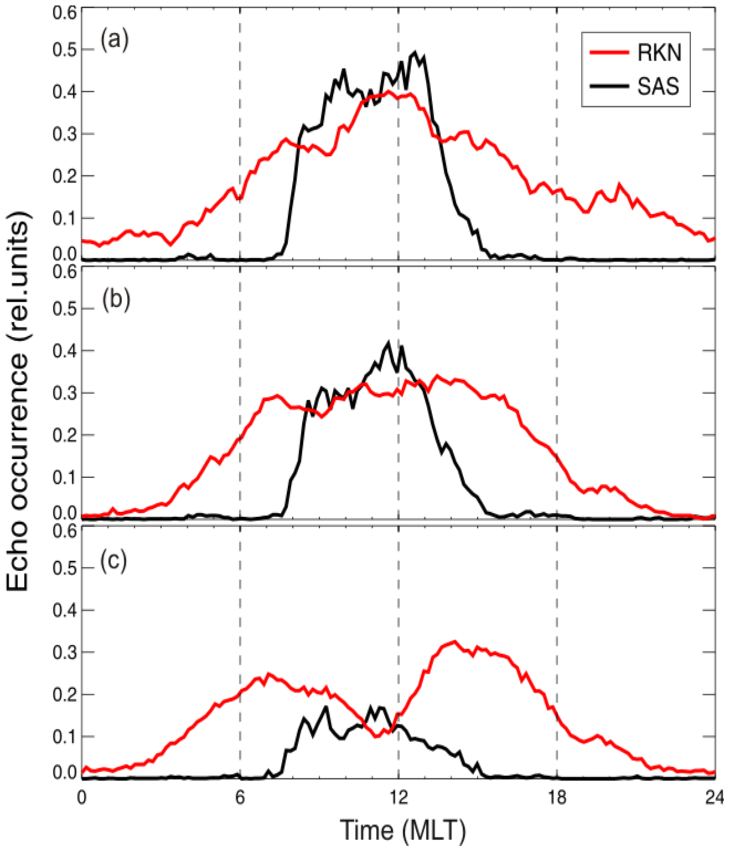

Figure 4.7: Occurrence rate of RKN (red) and SAS (black) echoes versus MLT at magnetic latitudes of (a) 79° (b) 81° and (c) 83° in December 2009.

4.6 Solar cycle effect on occurrence of Saskatoon F-region echoes

The data accumulated by the SAS radar since 1993 provide an opportunity to look at long-term trends in echo occurrence. An important feature of this radar is exceptionally diligent work in radar maintenance so that it has been consistently at the top of its capabilities in terms of hardware/electronics operation. We note that at certain point (~2001), the radar started working in the sounding mode with a search for the radar frequency with the best echo occurrence. This improvement has been kept ever since. Unfortunately, as we will show, it is difficult to assess quantitatively the impact of the improvement as the period of transmitting frequency search introduction coincided with the solar cycle maximum when the number of echoes was the largest due to geophysical reasons.

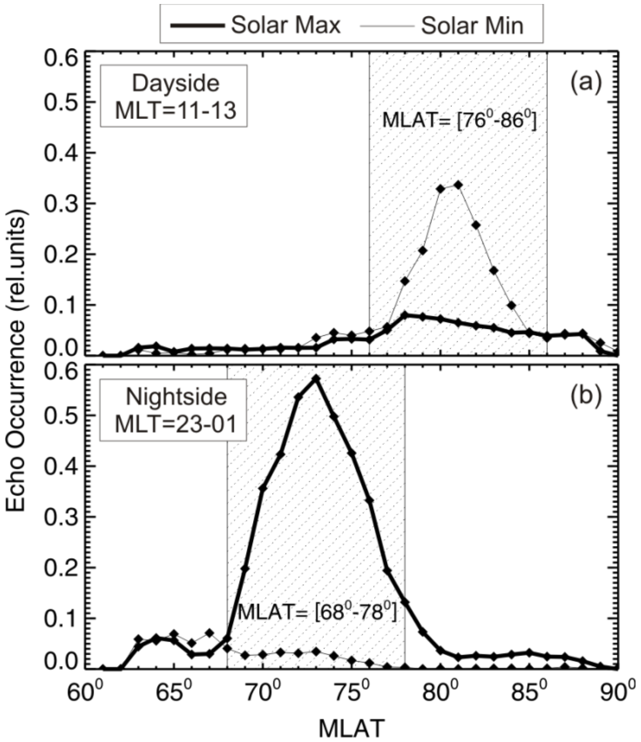

Figure 4.8: Monthly-averaged echo occurrence rates at various magnetic latitudes for the SAS radar observations in January 2002 (thick line) and January 2010 (thin line) during (a) near noon hours (11-13 MLT) and (b) near midnight hours (23-01 MLT). Vertical dashed lines delineate the band of latitudes with highest F-region echo detection. These bands have been considered for data averaging.

We computed the occurrence rates for the SAS radar similarly to the 2008-2010 data discussed above with one exception: we selected slightly different bands of echoes to be considered. The reason is that over the solar cycle, the band of F-region echoes shifts closer or away from the radar in accord with variations of the typical electron density in the ionosphere (*Danskin*, 2003). Figure 4.8 presents echo occurrence rates in January during near noon and midnight hours in January 2002 (solar maximum period) and 2010 (solar minimum period). One can see that for a fair assessment of the near noon data the latitudes should be 76°-86°, while for the midnight hours, the latitudes should be 68°-78°. These bands were adopted for the entire SAS data base. The selection of near noon and near midnight observations is not an arbitrary choice. We processed data in other MLT sectors and found that near noon and near midnight data are two extremes.

Figure 4.9 shows variations of the SAS echo occurrence rate for winter (blue line), spring equinox (solid black line), summer (red line) and fall equinox (black dotted line) for the period of 1994-2010. The selection of months for each season is as follows: December, January and

February for winter; March, April and May for spring equinox; June, July and August for summer and September, October and November for fall equinox. Each point in Fig. 4.9 is an average over season rate. We also show in Fig. 4.9a the 10.7-cm radio flux averaged over the same seasons. This panel indicates that the Sun's activity was highest (lowest) in 2000, 2001 and 2002 (1996 and 2008).

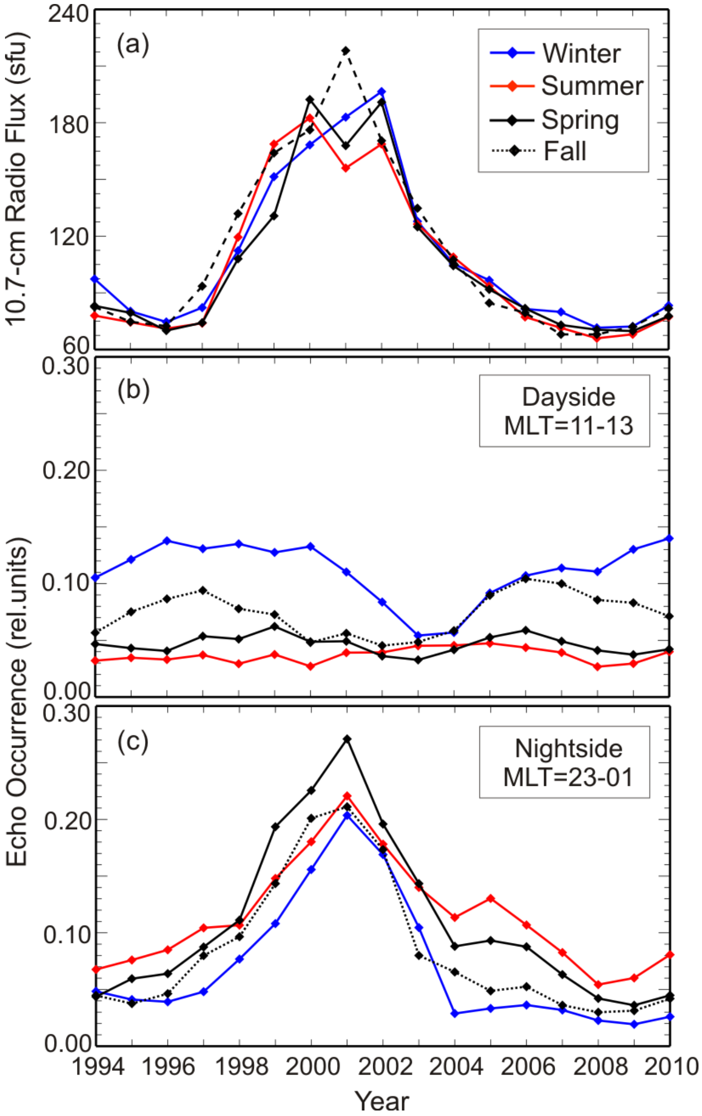

Figure 4.9: Season-averaged (a) 10.7-cm radio flux; (b) SAS radar echo occurrence for observations near noon hours (11-13 MLT); (c) SAS echoes near midnight hours (23-01 MLT). All data in the period of 1994-2010 were considered.

Observations on the dayside, Fig. 4.9b, show quite a different trend of winter data as compared to all other seasons. First of all, the winter values of occurrence (blue) are several times larger than other seasons. Secondly, the plot shows a strong decrease in winter echo occurrence with minimum in 2003 and 2004. This period is not exactly the maximum of the solar activity, but rather the declining phase of the solar cycle. Finally, occurrence rates for other seasons are comparable varying around 5%.

Observations on the nightside, Fig. 4.9c, show very clear maxima for all seasons coinciding with the period of the solar activity maximum. Largest rates were reached during equinoxes. Another feature of the data is that the summer curve (red) is well above black and blue curves away from the solar maximum periods. Thus the echo occurrence enhancement at the solar maximum (as compared to other years) is smallest for summer seasons, when the increase is about 3 times, and larger for other seasons, when it is on the order of 10. We note that although the increase in number of echoes for the solar maxima periods has been reported in the past, here we not only show the strength of the effect for various seasons, but also show that on the dayside there is not much of an enhancement and rather a "dip" was observed in 2003-2004. We processed data for the Prince George and Hankasalmi radars and found similar feature in their data. This implies that the dip is not an instrumental effect but rather real geophysical phenomenon that requires explanation.

4.7 Discussion

The presented data demonstrated once again that the occurrence of F-region echoes depends strongly on the radar location, season and time of the day. We showed that the INV and RKN PolarDARN radars, despite having difference in geographic locations (by 6°) but minor difference in magnetic location (by 1.5°) show similar trends and comparable echo occurrence rates. We found that the patterns of echo occurrence at certain latitude are similar for the RKN PolarDARN radar (½-hop propagation mode at MLATs=80°-85°) and the SAS auroral zone radar (1½-hop propagation mode at MLATs = 75°-80°). The difference was mostly in the occurrence magnitude, Fig. 4.6.

For SAS observations at magnetic latitudes of 80°-85°, the same band as for the RKN radar, despite the fact that the SAS radar detects echoes very likely through 1½-hop propagation mode, the pattern of occurrence (actual data were not presented) is somewhat similar to observations at lower magnetic latitudes with the maximum during winter noon hours and additional echo detection away from the noon (with much lower rates) for other months except of summer periods when very few echoes are observed. We note that, according to our analysis, for the periods of solar maximum, the SAS radar does not show an increase of near noon echoes, contrary to the midnight observations.

The contrast between the RKN and SAS radars in echo detection rates for the polar cap latitudes of 80°-85° is higher than for the best echo detection zones. This is not a surprise since for the auroral zone radars one need additionally satisfactory conditions for radio wave bending and reflection from the ground to reach these high latitudes. Summer time the HF radar wave bending is not a critical factor as the electron density is typically sufficiently high. There are fewer problems with the ground reflection conditions as well, contrary to winter when icy surfaces reflect poorly. One then would expect the strongest differences winter time, which is not the case according to Table 4.2. The reported difference in echo occurrence implies that besides refraction and reflection from the ground, additional factors control polar cap echo detection with the auroral zone radars; the irregularities do exist in the polar cap (according to PolarDARN) for much more extended periods but the auroral zone radar cannot simply detect them.

The observation that for the near noon winter time the SAS radar can see more echoes than the RKN radar is surprising (Fig. 4.7). It did not happen every December but closer number of echoes for the SAS and RKN radars around winter noon is a consistent feature of the data considered. If one recalls that the SAS echoes are received from much larger ranges (farther by ~ 1500 km), since the echo power is proportional to $1/r^3$ (*Walker et al.*, 1987), the result would seem even more astonishing. The implication of the effect is that the propagation factors are very important to keep in mind for the polar cap radars as well, especially during winter time when the ionosphere is depleted being in darkness over significant periods of time.

The discovered local decrease in number of dayside echoes on the declining phase of the solar cycle (2003-2005) is an unknown so far phenomenon. We cannot give explanation but one idea comes to our mind. We noticed that the critical frequencies of the Sodankyla ionosonde for these years of the solar cycle decline were decreasing much quicker as compared to other years of solar cycle, see Fig. 1.6. This effect points at a possibility that the ionosphere was less dense during these years, in a statistical sense, so that propagation conditions were often unsatisfactory.

4.8 Conclusions

In this study we investigated the F-region echo occurrence rates for four Canadian SuperDARN/PolarDARN radars over the solar minimum period of 2007-2010 and showed that at magnetic latitudes above 80°:

1) The INV and RKN PolarDARN radars show comparable rates all the time.
2) The RKN and INV PolarDARN radars detect 1.5-2.5 times more echoes through ½-hop propagation mode than the SAS and PGR SuperDARN radars through 1½-hop propagation mode, latitudes of 80°-85° for the PolarDARN and 75°-80° for the SuperDARN radars.
3) There is a strong seasonal variation in occurrence rates. On average over 24-hour periods, echoes are more frequent winter time; the occurrence decreases towards summer where it is ~2 times smaller. However, for dusk-midnight-dawn sector of 18-24-06 MLT, echoes are more frequent during equinoxes. The auroral zone radars (SAS and PGR) show similar equinoctial maxima.
4) There is a strong variation of echo occurrence with magnetic local time. The character of the variation depends on the season. For winter and summer, echoes are more frequent near noon. For equinox, additional maxima occur at dusk-midnight-dawn and occurrence of echoes during these periods lead to equinoctial maxima in overall echo occurrence.

Additionally, we investigated the near noon and near midnight echo occurrence rates for the Saskatoon radar over the period of 1994-2010 and showed that

5) There is a strong, by a factor of 10, increase in SAS nightside echo occurrence towards solar maximum for all seasons. The effect does not exist for the dayside echoes; moreover, a decrease in number of echoes, by a factor of ~2 in winter, was discovered for the declining phase of the solar cycle.

CHAPTER 5

ELECTRIC FIELD AND ELECTRON DENSITY AS FACTORS CONTROLLING OCCURRENCE OF F-REGION HF ECHOES

Our second task is an assessment of factors that control HF echo occurrence. We investigate potential role of two factors, electric field magnitude and F-region electron density in the scattering volume.

For such a work, an independent instrument measuring these parameters within one of the SuperDARN radar FoVs is required. In the Canadian sector of Arctic, the CADI ionosonde at Resolute Bay (MLAT=83°) has been operational for a number of years (*Jayachandran et al.*, 2009). CADI measures the plasma drift in the zenith of the station as described in Subsection 3.2.2. CADI also measures electron density in the ionosphere by recording ionograms as explained in Subsection 3.2.1. The RB CADI ionosonde is located in the middle of the RKN FoV close to its beam 5 and gates 26-27 and thus the RB CADI is convenient for comparison with RKN data.

Since CADI data are for a localized area of the ionosphere, a direct point-by-point comparison between the radar and ionosonde data would be the natural approach to address the problem. Such an approach, however, makes very complex scatter plots that are difficult to interpret and arrive to a certain conclusion. For this reason, we attack the problem differently, namely we consider seasonal and MLT variations in occurrence of echoes and compare them with similar variations in the ionospheric electric field and electron density. Our analysis thus is not a direct one but it still involves information on the parameters in the scattering volume and thus it is a step forward as compared to the previous studies in the field that we reviewed in Chapter 2.

5.1 Effect of electric field on echo detection

The power of coherent backscatter is proportional to the mean square of electron density fluctuations $\langle |\delta n_e|^2 \rangle$, Eq. (2.25), which might depend on electric field. For the case of E-region electrojet irregularities the dependence is of a quadratic type (e.g., *Uspensky et al.*, 2001). For the GDI in the F region, the character of the dependence is not known. However, as we discussed in Section 2.2, the growth rate of the GDI is proportional to electric field (Eq. 2.15). Since the GDI is the main mechanism of plasma irregularity formation, one can think of the electric field as irregularity production factor affecting HF echo detection. This is a starting point in our study of correlation between variations in the occurrence rates of HF radio echoes for different seasons and electric field variations in the ionosphere.

5.1.1 Statistics of electric field over RB according to CADI measurements

Figure 5.1 gives histogram distributions of the measured electric field (median value) for every MLT hour and four seasons in 2010. The seasons were selected as follows: winter - December, January and February; summer - June, July and August; spring equinox - March, April and May; fall equinox - September, October and November. For simplicity of presentation, here we consider data for one full year of CADI observations in 2010. It is notable that the CADI observations in other years, 2008 and 2009, show the same features as the observations in 2010. The data show maxima for every season; the median values over all MLTs are in between ∼16 and ∼18 mV/m with the standard deviation from the mean of ∼2-3 mV/m. Winter (blue line) data, Fig. 5.1, show broad enhancement between ∼2 and ∼8 MLT, corresponding to late-evening/midnight sectors. Summer (red line) and equinox data show more distinct near-noon maxima between 9:00 and 14:00 MLT. The data presented indicate that, despite dramatic variations in echo occurrence versus MLT (Chapter 4), the average electric field does not change strongly.

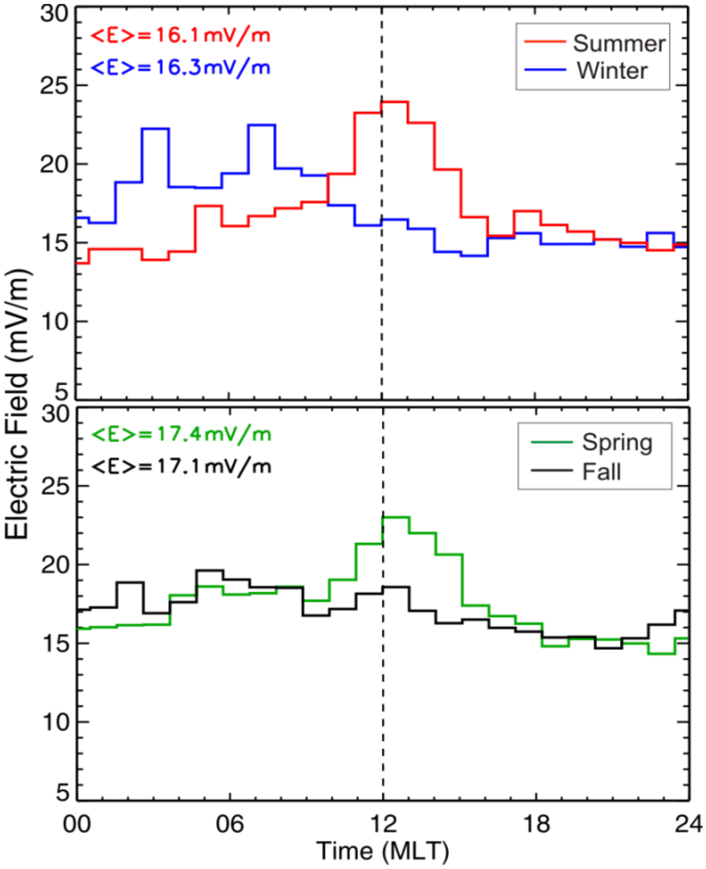

Figure 5.1: Histogram distribution of the hourly-median electric field magnitude measured by the Resolute Bay CADI as a function of MLT in different seasons of 2010. The averaged values of electric field magnitude over 24 hours in every season are shown in the upper left hand corner.

5.1.2 RKN echo occurrence rate and CADI electric field over RB

We first show data for the RKN echo occurrence at the magnetic latitude of Resolute Bay, Λ =83°, Fig. 5.2. Here measurements in RKN beams 4-6 were considered. One can easily recognize the "cross" pattern of echo occurrence discussed with respect to the data of Fig. 4.6a. For observations at 83°, summer noon echo enhancement looks stronger, and another feature is more frequent echo occurrence during post-noon hours. The winter near noon depression in echo occurrence discussed in Section 4.5 is recognizable for the December 2009 - January 2010 data. For convenience of future discussion, we indicate in Fig. 5.2 the time for the local sunrise and sunset by dashed line. One should notice that the difference between local time (LT) and MLT for central beams 4-6 of RKN radar is as small as 20 minutes.

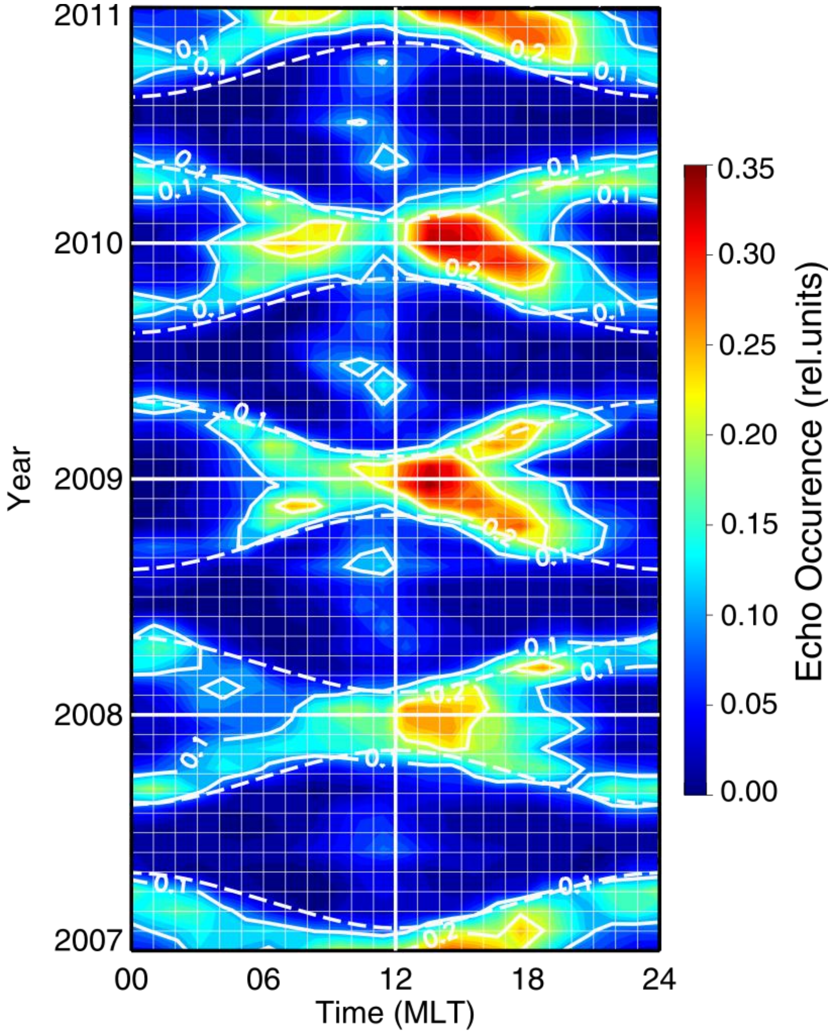

Figure 5.2: RKN echo occurrence rate versus MLT for various months of 2007-2010. Data at magnetic latitudes of 83° (over Resolute Bay) were only considered. Overlaid white contours correspond to the echo occurrence of 0.1 and 0.2. Dashed lines represent the sunrise and sunset time over Resolute Bay.

Figure 5.3a plots electric field magnitude versus MLT for three years, 2008-2010. We note that the RB CADI electric field data base is quite extensive as for most of hours we had about 70 individual measurements. The pattern of areas with enhanced electric field is the same of all the data; there is a strong enhancement around 06:00 MLT winter time and around 12:00 MLT summer time. In addition to electric field data in Fig. 5.3a, the contours of RKN echo occurrence over RB with the rate of 0.1 and 0.2 are presented. The shape of the contours is the same as in Fig. 5.2. The near-noon electric field enhancement correlates with small "blobs" of echo occurrence during summer. The dawn-side enhancements of electric field correspond to the edge of the area with enhanced echo detection rate.

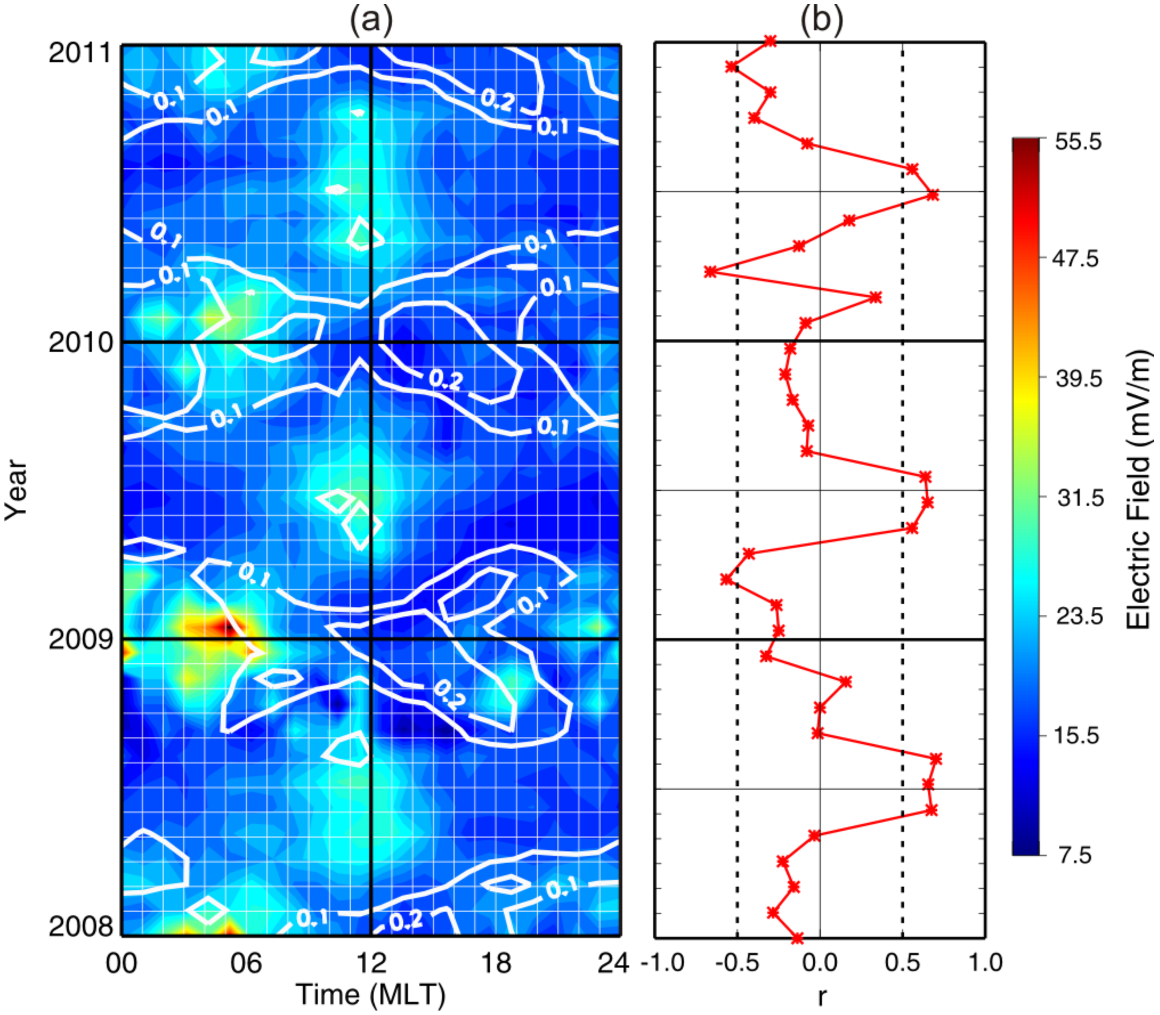

Figure 5.3: (a) Electric field according to Resolute Bay CADI plotted as a function of MLT for various months of 2008-2010. Overlaid white contours correspond to the RKN echo occurrence over Resolute Bay of 0.1 and 0.2 (compare with Fig. 5.2). (b) Linear Pearson correlation coefficients (r) between MLT variations of RKN echo occurrence over Resolute Bay and electric field variations (shown in (a)) for various months of 2008-2010.

To quantify the effect of the electric field in occurrence of RKN echoes, we computed linear correlation coefficients between the echo occurrence rates and electric field for various MLT times. The inferred correlation coefficients for each month are presented in Fig. 5.3b. The correlation is fairly reasonable during summer months and it quickly deteriorates for other months with the worst result during winter periods. The numerical values of correlation coefficient between echo occurrence and electric field in January and July of 2008-2010 are listed in the third column of Table 5.1. The correlation values vary between 0.62-0.67 (with confidence level values of 0.73-0.75) for the summer months while there is no correlation for winter months.

Table 5.1: Linear Pearson correlation coefficient (r) for the variation of echo occurrence rate versus electric field and electron density. Winter and summer months (January and July) of 2010 were considered.

Year	Month	r (OCC - E field)	r (OCC - NmF2)
2008	January	-0.14	0.88
	July	0.67	0.42
2009	January	-0.24	0.89
	July	0.64	0.42
2010	January	-0.09	0.83
	July	0.62	0.33

5.2 Effect of electron density on echo detection

As we discussed in Section 2.3, it is expected that the backscattered power of HF echoes might depend on the background electron density. In this Section we show the dependence of HF backscattered power on electron density from observations and investigate correlation between HF echo occurrence rates at different times of year and variations of the electron density.

5.2.1 Statistics of F2 peak electron density over RB from ionograms data

Resolute Bay CADI regularly produces ionograms, typically with 5-min dwelling time. The scaling of the Resolute Bay ionograms has been started recently, and we present here data for the critical frequency of F2 layer available for the period of 2008-2010. For simplicity of presentation, here we consider data for one full year of CADI observations in 2010. It is notable that the CADI observations in other years, 2008 and 2009, show the same features as the observations in 2010. The ionogram scaling work has been done by *D. Themens* (University of New Brunswick). The procedure of inferring the electron density of F2 peak from ionograms was described in Subsection 3.2.1. We note that to achieve complete coverage of the electron density plot, the RB CADI ionograms were scaled for at least 5 days a month, covering the beginning, middle and end of each month. Typically, for an individual day, data were available for every 5-min. For some months, 1-min data were available; these were usually periods of special experiments.

Figure 5.4 gives a histogram distribution of the electron density versus MLT for four seasons. The seasons were selected in the same way as for the electric field measurements (described in previous Section). As expected, densities are at maximum near magnetic (and solar) noon (12 MLT) for all seasons at the time of the ionosphere being under strongest Sun illumination. It is notable that the difference between LT and MLT for central beams 4-6 of RKN radar is as small as 20 minutes.

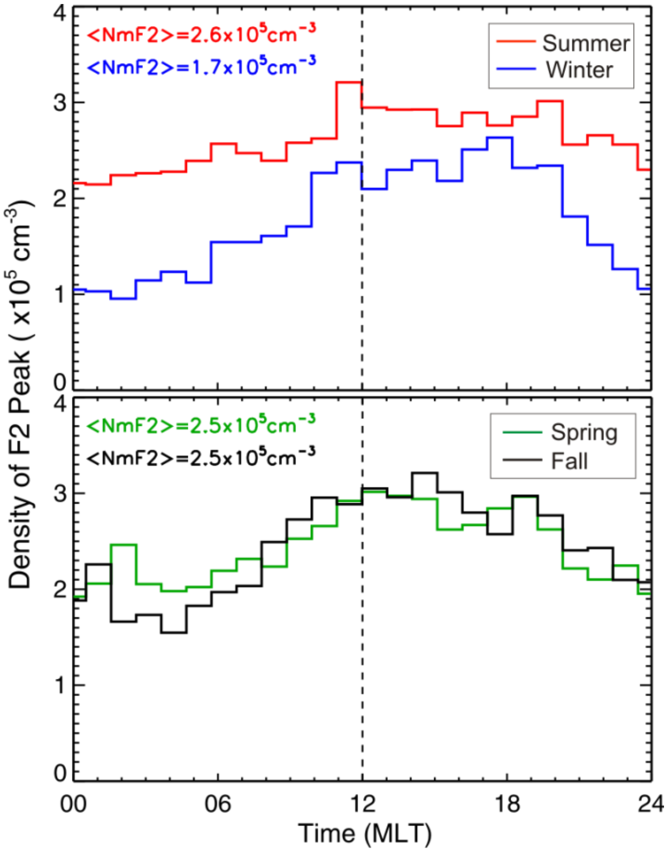

Figure 5.4: Histogram distribution of the hourly-medianF2 peak electron density (NmF2) inferred from the Resolute Bay CADI ionograms as a function MLT time. Data in different seasons of 2010 were considered. The averaged values of NmF2 over 24 hours in every season are shown in the upper left hand corner.

Densities for summer time (Fig. 5.4, red line) are above 2.2×10^5 cm^{-3} all day long with a median value of 2.6×10^5 cm^{-3} (above the threshold of 2.5×10^5 cm^{-3} in echo detection, *Danskin et al.*, 2002) so that one would expect no problems with reaching the orthogonality at any time. Near noon density enhancements are seen during winter (Fig. 5.4, blue line), but closer toward midnight sector, density significantly decreases to as low as 1.0×10^5 cm^{-3}. The median value of density during winter is 1.7×10^5 cm^{-3}. During equinoxes, near noon density reaches values of 3.0×10^5 cm^{-3} which is comparable with summer values. The smallest densities occur in the midnight sector between 00:00 and 05:00 MLT and 21:00 and 24:00 MLT during equinoxes. The median value of density during equinoctial months is 2.5×10^5 cm^{-3} which is close to the median of density during summer months. In terms of the seasonal and MLT trends, the data of Fig. 5.4 are consistent with density measurements by the incoherent scatter radar at Svalbard, at ~5° lower geomagnetic latitude (*Cai et al*., 2007). However, the ISR data refer to the period of maximum solar activity, and this is, very likely, the reason why the density magnitudes were larger by ~1.5 times in that study.

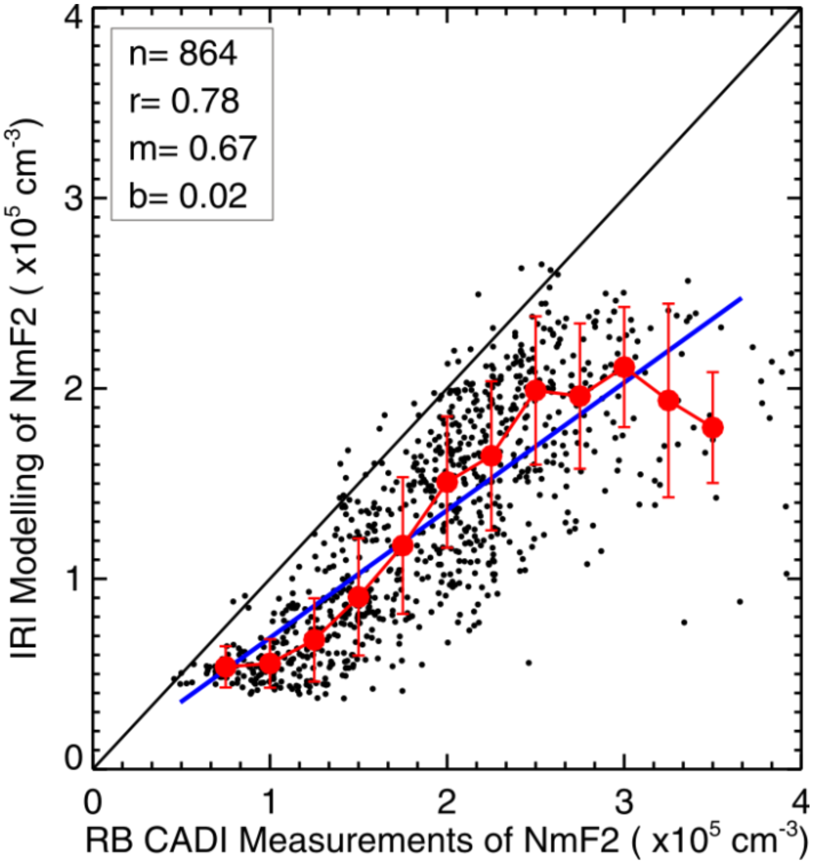

Figure 5.5: Scatterplot of monthly-median values of NmF2 according to RB CADI measurements and density values taken from the IRI model for the RB magnetic latitude. Data trends are shown by binned values (red dots, bins of 0.25×10^5 cm^{-3}) and a linear fit (blue line). Vertical lines illustrate standard deviation in each bin. Total number of points involved (n), linear Pearson correlation coefficient (r) and parameters of linear fit (the slope of the line (m) and the line's y-intercept (b)) are shown in the upper left hand corner. All data for 2008-2010 were considered.

In Figure 5.5 we compare F2 peak electron density (NmF2) values obtained from the RB CADI ionosonde and from the IRI model. We considered IRI density values at MLAT=83° for every MLT hour and month of 2008-2010. One can notice a general consistency of the data in terms of a tendency for the IRI values to be smaller than the CADI values. The model and CADI values are fairly correlated with the linear Pearson correlation coefficient of $r = 0.78$. The slope of the linear trend is 0.67. This implies that the IRI values of NmF2 are underestimated by ~30%.

5.2.2 Dependence of HF backscatter power on electron density for the period of solar minimum 2008-2010

Having the F2 peak electron density inferred from ionogram data with 1- or -5 minute resolution for about 5 days per month (available resolution of Resolute Bay CADI measurements) allows us to test an expectation that the backscattered power of F-region HF echoes increases with the electron density in the ionosphere (Section 2.3). For presentation here, we considered 36 months of joint RKN radar - CADI ionosonde observations over Resolute Bay for the years of minimum solar activity, 2008-2010. We compare the simultaneous measurements of the power by the RKN radar and F2 peak electron density by the CADI ionosonde over Resolute Bay in Fig. 5.6.

Figure 5.6 shows that the cloud of points is quite spread although one can recognize a tendency for the echo power to increase with the electron density in the range of CADI values of $(0.5 - 1.2) \times 10^5\ \text{cm}^{-3}$. This is more evident if one looks at the binned values of the power, red dots in Fig. 5.6. For CADI densities greater than about $1.3 \times 10^5\ \text{cm}^{-3}$, the power seems to go down. These tendencies are similar to the ones reported by *Danskin* (2003), his Fig. 4.17. He considered the Hankasalmi radar observations over the EISCAT spot of electron density measurements.

The effect of the power decrease at relatively large electron densities can be explained by the fact that for the denser ionosphere, the ionospheric refraction would shift the band of HF echo detection to shorter ranges. As a result, at a fixed range (e.g., over Resolute Bay) the power of backscattered signal would decrease for relatively large values of the electron density (*Uspensky et al.*, 1994).

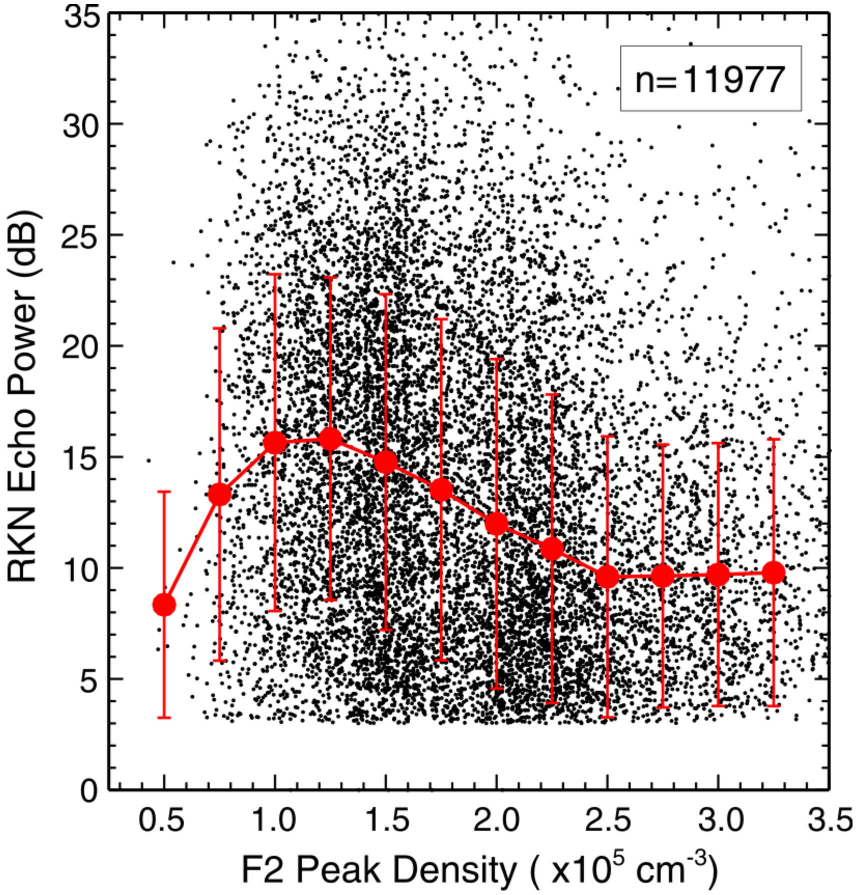

Figure 5.6: Scatterplot of power of RKN echoes over RB versus electron density of the F2 peak (according to the RB CADI ionosonde) based on point-by-point analysis. Data trends are shown by binned values (red dots, bins of 0.25×10^5 cm^{-3}). Vertical lines illustrate standard deviation in each bin. Total number of points involved (n) is shown in the upper right hand corner. All data for 2008-2010 were considered.

5.2.3 RKN echo occurrence and CADI electron density over RB

Figure 5.7a is a contour plot of electron density at the F2-layer peak versus magnetic local time for three years, 2008-2010. The shape of the contours is the same as in Figs. 5.2 and 5.3a. In Figure 5.7a the electron density is enhanced during near-noon summer periods. The overall density is larger in 2010 as compared to 2008 and 2009 and there is a tendency for the maximum to shift towards the fall equinox in 2009 and 2010. The sunrise/sunset lines (dashed curves) separate clearly the periods of enhanced/decreased electron density from the periods of weak density. In addition to the electron density data in Fig. 5.7a the contours of RKN echo occurrence over RB with the rate of 0.1 and 0.2 are presented. Contours of the echo occurrence overlap significantly with the areas of the enhanced electron density.

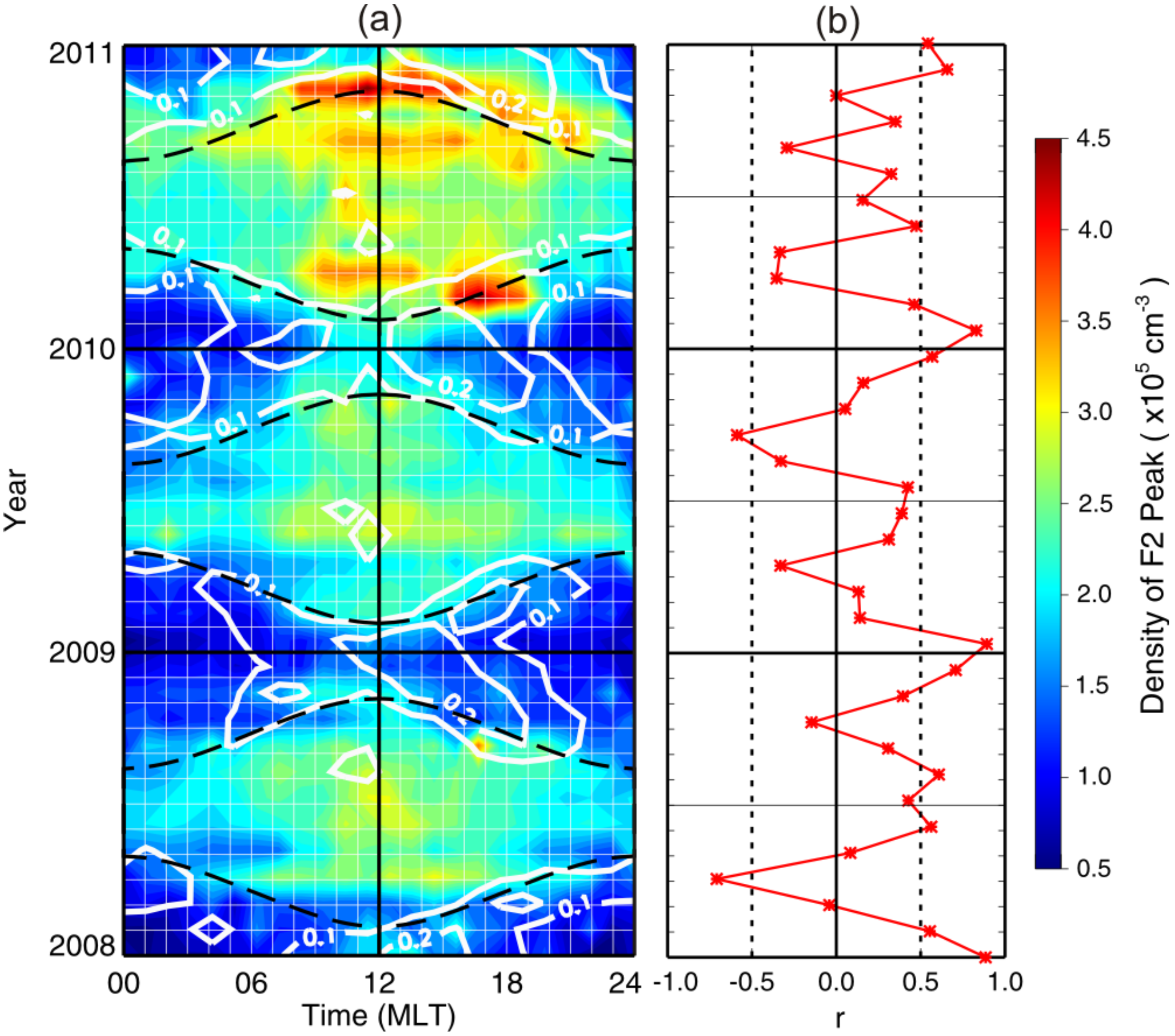

Figure 5.7: (a) F2 peak electron density according to Resolute Bay CADI as a function of MLT for various months of 2008-2010. Overlaid white contours correspond to the RKN echo occurrence over Resolute Bay of 0.1 and 0.2 (compare with Fig. 5.2). Dashed lines represent the sunrise and sunset time over Resolute Bay. (b) Linear Pearson correlation coefficients (r) between variations (versus MLT) of the RKN echo occurrence over Resolute Bay and corresponding variations of the electron density (shown in (a)) for various months of 2008-2010.

To quantify the effect of the electron density in occurrence of RKN echoes, we computed linear regression coefficients between variations of the echo occurrence and the squared electron density. The inferred correlation coefficients for each month are presented in Fig. 5.7b. One can see that correlation is fairly reasonable during summer and winter months. The correlation is lowest (sometimes does not exist at all) for equinoctial periods. The numerical values of correlation coefficient between echo occurrence and electron density in January and July of

2008-2010 are listed in the fourth column of Table 5.1. There is a strong correlation of the order of 0.83-0.89 (with confidence level values of 0.78-079) for the winter month of January in all three years. However, in summer month of July the correlation decreases to 0.33-0.42 (with confidence level values of 0.54-0.63).

5.3 Discussion

Koustov et al. (2004) studied the solar cycle and seasonal variations in echo occurrence of the SAS radar on the nightside and concluded that the major factor responsible for an increase in echo occurrence toward solar cycle maximum and during equinoxes is due to enhanced electric fields and more frequent occurrence of strong plasma gradients, in other words, the irregularity production factors.

The data presented in this study do not lend significant support for the electric field factor. Comparison of RKN echo occurrence over RB with CADI electric field measurements over RB showed that indeed electric fields are somewhat enhanced during summer noon hours and there is correlation in echo occurrence and electric field changes over a day for this season. This hints on the potential role of electric field, the irregularity production factor. On the other hand, during winter time electric fields were strongest in the dawn sector while the amount of echoes was much smaller here than near the noon. The equinoctial observations are of special interest because the electric field seems to be about the same all day long (the same blue color in Fig. 5.3a) while the echoes were mostly observed (with comparable rates) between ~06:00 and 18:00 MLT, i.e. roughly for the sunlit conditions. In addition, according to Fig. 5.3a, the electric field during equinoxes is not stronger, on average, as compared to other seasons while the occurrence of echoes (mostly on the dawn and dusk sides) is increased for the equinoxes. Additionally, as we reported in Section 4.6, the SAS radar shows decrease of near noon winter echoes during declining phase of maximum solar activity (2003-2005), but close to its maximum. Since one would expect stronger near noon electric fields during solar maximum (stronger interplanetary electric fields that are mapped into the high-latitude ionosphere), the effect can imply that electric field is not the major factor affecting occurrence of the polar cap F-region echoes. One can conclude that, although enhanced electric field is needed to produce F-region irregularities, other factors are more important for detection of F-region echoes.

Previous publications are inconclusive whether a strong electric field is required to detect F-region echoes. *Milan et al.* (1999), *Danskin et al.* (2002) and *Danskin* (2003) presented several examples of HF echo observations from an area where the electric field was monitored by the EISCAT incoherent scatter radar (direct propagation mode, ranges ~900 km). It was found that the F-region echoes can occur at electric fields as low as several mV/m though the electric field typically was stronger than 5 mV/m. The presence of very strong electric fields did not guarantee that HF echoes were detected. Furthermore, when the echoes were observed, their power was not necessarily enhanced. This conclusion is in line with findings of *Fukumoto et al.* (1999, 2000), who showed that there is only a slight correlation of the F-region echo power with the HF Doppler velocity (which in turn is proportional to the $\boldsymbol{E} \times \boldsymbol{B}$ drift).

The reported PolarDARN data trends and comparisons with ionosonde electron density data point at stronger importance of the propagation factors and electron density for the polar cap echo detection. The electron density affects HF echo detection in several ways. The one, that is very difficult to investigate, is the attenuation of HF radio waves in the D region. D-region electron density is sensitive to the sunlight so that fewer echoes are expected during daytime. However, under sunlight, there is (simultaneously with the D-region creation) an increase in the F-region density which produces stronger refraction and improves chances to get echoes. One would generally expect stronger D-region absorption summer time, and not surprisingly, echo detection rates are lowest summer time, Figs. 4.4, 4.6 and 5.2, although there is another important effect, smoothing out density gradients, which will be discussed later. Another way of arguing for the D-region attenuation as a factor is the fact that winter echo occurrence rates are highest for the PolarDARN radar FoVs being in the dark ionosphere.

If D-region attenuation is indeed important factor for HF echo detection, the number of PolarDARN echoes would decrease with the approach to the solar cycle maximum, and one might not see such a contrast between the PolarDARN and SuperDARN echo occurrence rates. On the other hand, more frequent structured precipitations typical for solar maximum periods might provide additional irregularity production and the effect of additional attenuation would be compensated.

During winter (December), the RKN radar FoV at short ranges of < 500 km emerges out of the darkness near local noon and is sunlit while the FoV at far ranges is still in darkness. Sunlight might produce additional D-region radio wave attenuation while the irregularity production is not affected by the sun for this period and this can explain, at least partially, the RKN echo occurrence depression for near noon winter observations, Fig. 4.7.

Another way the electron density affects the detection of HF echoes is directly, because the electron density in the scattering volume enters the equation for HF echo power directly as a density squared term, Section 2.3, (*Uspensky et al.*, 1994; *Ponomarenko et al*., 2009). *Milan et al*. (1999) and *Danskin et al.* (2002) estimated that an electron density of $\sim 2 \times 10^5\ \mathrm{cm}^{-3}$ is needed for the optimum F-region echo reception for the Hankasalmi radar (located at magnetic latitude of $\Lambda \approx 67°$). For the Canadian radars, optimal densities should be somewhat (but not much) larger since the aspect angle conditions here are worse than in the European sector and stronger radar wave bending is needed here to achieve orthogonality with the Earth's magnetic flux lines. Comparison of contours for the echo occurrence and density in Fig. 5.6a gives an estimate for the threshold density of $\sim 2.5 \times 10^5\ \mathrm{cm}^{-3}$, which is consistent with expectations. This value characterizes a cumulative effect of both propagation and production factors.

While working with the RKN data, we discovered another feature in echo occurrence that can be linked to the electron density effect. In attempt to find a RKN beam with "preferential" echo occurrence, we realized that while over 24-hour periods, the echoes were more frequent in the central beams, during dusk and dawn, the echoes were clearly more frequent in beams (4,5) and (10,11), respectively. The effect is illustrated in Fig. 5.8 where observations in September 2010 were considered.

The line plot indicates a shift of the best echo detection direction towards the sunlit (noon) ionosphere with enhanced electron density. The shift in the "preferential" beam toward sunlit ionosphere was strongest during equinoxes and did not happen in the noon and midnight sectors where there is no (statistically speaking) preferential beam orientation with enhanced electron density. It is interesting that for the McMurdo (MCM) radar in the southern hemisphere (June 2010) the echo occurrence rate is significantly increased (decreased) whenever the radar FoV is coming out (into) of darkness (the MCM data are not presented here, but the effect can be recognized in data presented by *Bristow et al.* (2011), their Fig. 6b).

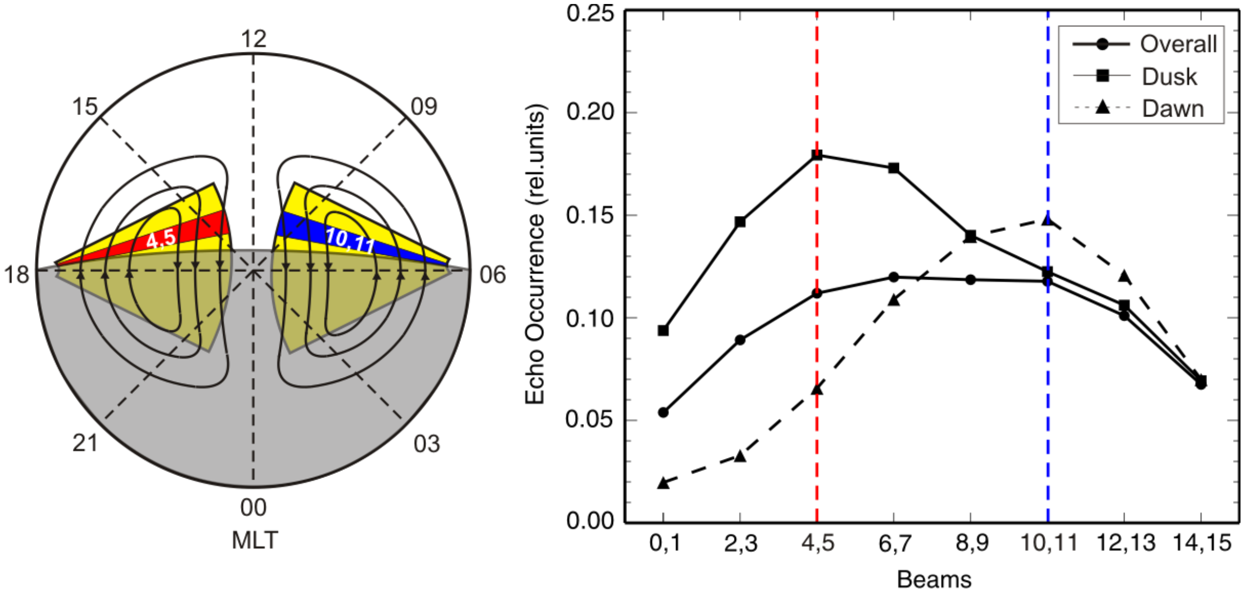

Figure 5.8: RKN echo occurrence rates at magnetic latitudes of 80°-85° for various pairs of beams. Observations in September 2010 were considered. The position of beams with best echo occurrence rates is shown in the schematic cartoon on the left.

Reasonable correlation of the electron density and echo occurrence over a day for winter and equinox (Fig. 5.7a) signifies the importance of the electron density, either through providing refraction or through direct impact. In this respect, it is interesting that the amount of refraction is sufficient during most of a day during summer, and the echo detection is expected to be controlled by irregularity production factors (enhanced electric field) and D-region attenuation. It is not a surprise that although the electron density increases by a factor of 1.5-2 from winter to summer (Fig. 5.7a), the occurrence rates changes by a factor of 3. This implies that other factors also contribute.

The electron density distribution in the ionosphere can affect the echo detection not only through propagation conditions but also through altering the conditions for the excitation of plasma irregularities. This is because the GDI in plasma (*Tsunoda*, 1988) requires the presence of background plasma density gradient perpendicular to the Earth's magnetic field. Unfortunately, plasma density gradients, especially of scales smaller than ~1-10 km, are very difficult to measure and such measurements were not available for our observations. For this reason, we limit ourselves here by commenting on the potential role of sun's radiation that smooth out the gradients. *Ruohoniemi and Greenwald* (1997) argued that this is the most likely reason for significantly decreased echo detection during summer months. This argument is equally applicable to our case and can explain our data presented in Figs. 4.4, 4.6 and 5.2. It is interesting that in June the echo occurrence maximizes in the pre-noon sector, at ~10-12 MLT, Fig. 5.2, while there is almost no darkness over the RKN FoV. Thus, the summer echo occurrence maximum cannot be linked to the sun-illumination effect but rather to other factors important for the pre-noon sector. We believe this factor is enhanced electric field as discussed earlier.

Away from summer time, April or August, the RKN FoV is getting less and less sun illumination, and the number of echoes increases, as compared to summer periods. This feature is perhaps another evidence of the harmful effect of the solar radiation on irregularity production (the absolute values of the electron density are sufficient for proper refraction during these periods, as densities do not decrease significantly during equinox as compared to summer time, Fig. 5.7a. Near equinox (March) the RKN radar detects most of dawn and dusk echoes as compared to other seasons. This happens, very likely, not only because of absence of the sunlight but also because the electron density magnitudes are still reasonably high, Fig. 5.7a. The situation changes in winter when the densities are strong enough only during near noon time and not many echoes are seen away from the noon. It seems that decrease in the solar radiation smoothing effect in combination with the relatively strong electron densities during equinox are the factors providing equinoctial maxima in echo detection.

5.4 Conclusions

By comparing CADI ionosonde data and RKN echo occurrence rates over Resolute Bay in 2008-2010, we showed that:

1) Winter-noon maximum of echo occurrence correlates well with the enhanced electron density as inferred from ionosonde data. The RB CADI shows a minor electric field depression for near noon winter hours.
2) Summer-noon maximum of echo occurrence correlates with enhanced electric fields as seen by the RB CADI. Electron densities stay reasonably high all the time as inferred from ionosonde data.

3) During dusk-midnight-dawn hours of the equinoxes, the electron density is reasonably high and electric fields are strong so that both factors contribute to the increased echo detection. During equinoxes, the electron density stays enhanced for many hours away from the magnetic noon. The echoes are observed at later MLT hours and for longer hours away from the noon in the dusk sector as compared to the dawn sector.
4) The electron density for the periods of the RKN echo detection stays above 2.5×10^5 cm^{-3}, in agreement with the electron density threshold for HF echo detection reported by *Milan et al.* (1997) and *Danskin et al.* (2002).
5) There is no obvious electric field threshold effect for F-region echo occurrence over RB. The near-noon echo occurrence during summer correlates with enhanced electric fields but, generally, echoes were detected for electric field $>$10 mV/m.

CHAPTER 6

SUMMARY AND PLANS FOR FUTURE RESEARCH

In this thesis we assessed the solar cycle, seasonal and diurnal (MLT) variations in occurrence of F-region HF echoes observed by several northern hemisphere SuperDARN HF radars. We considered two auroral zone radars, SAS and PGR, and two polar cap radars, RKN and INV. Our major findings can be summarized as follows.

6.1 Occurrence rates

6.1.1 Solar cycle effect

In terms of the solar cycle effect, we confirmed previous results and found several new features. We demonstrated that the auroral zone radars, such as the PGR and SAS radars, showed consistently similar tendencies. This is not a surprise as the radars' observational conditions are similar. Data for the PolarDARN radars are not available to study the solar cycle variations. This needs to be done in future.

For SAS observations on the nightside, we confirmed that the occurrence of F-region echoes correlates strongly with the solar cycle with the occurrence rates being strongest during years of maximum of solar activity and smallest during years of minimum of solar activity. The differences in occurrence rates are as large as a factor of 10. The solar cycle effect is less pronounced for summer. It is important to note that the majority of nighttime SAS echoes were very likely received through the direct (half-hop) propagation mode.

For SAS observations on the dayside, no solar cycle effect was found for all seasons but winter. For winter observations, the surprising and new finding is that there is limited in time (the years 2003-2005) decrease of echo occurrence on the declining phase of the solar cycle. As discussed, the effect could be related to the fact that ionosphere was not dense enough during these years, the phenomenon, to the best of our knowledge, that has not been reported. It is important to note that the majority of daytime SAS (and PGR) echoes were very likely received through 1½-hop propagation mode.

6.1.2 Seasonal variation

Both the auroral zone radars considered showed seasonal variations in echo occurrence. Averaged over 24 hours occurrence rates are largest during equinoxes. The effect, however, depends on the magnetic local time of observations. The equinoctial maxima are well seen for the midnight echoes, weaker for the dusk/dawn sector and there are none for the dayside, near noon sector. The equinoctial maxima seen by the auroral zone SAS and PGR radars seem to be less pronounced as compared to the equinoctial maxima for the PolarDARN radars. Previously the equinoctial maxima in F-region echo occurrence were reported for observations in the auroral zone so that our study finds the presence of the effect at polar cap latitudes.

By considering data from the PolarDARN radars we showed that overall these radars see ~2 times more echoes than the auroral zone radars if one considers echo occurrence at ranges of best echo detection for each radar separately. This difference is less significant during summer time. If one considers echo detection at the same higher latitudes, we specifically looked at ranges 80°-85°, then the differences are larger.

One surprising discovery is that during winter near noon hours, the RKN radar can detect fewer echoes in the polar cap than the SAS radar despite the fact that the SAS radar detects echoes through 1½-hop propagation mode while the RKN radar detects them directly through ½-hop propagation mode.

6.1.3 Diurnal variation

The patterns of echo occurrence for the SAS and PGR radars in the season - MLT plane are similar: winter time echoes occur mostly during near noon hours. During equinoxes, more and more echoes are seen in the dusk and dawn sectors (this leads to more echoes during equinoxes). Summer time echoes are more frequent at nighttime. One clear difference of the PolarDARN radars is that they show additional maximum of echo occurrence during summer near noon hours.

6.2 Electric field and electron density in the ionosphere as factors affecting echo occurrence

Our comparison of the F-region maximum electron density (inferred from CADI critical frequencies of the layer) with RKN echo occurrence rates over Resolute Bay showed that more echoes occur for enhanced electron density: there is a correlation in changes of occurrence and electron density changes a) over a day and b) over a season. Such correlation was demonstrated for 3 years of radar-ionosonde joint operation. Our finding is in line with previously published results for the auroral zone radars where data statistics was not as good as in our case. We found that the echoes seem to occur for $n_e > 2.5 \times 10^5$ cm^{-3}.

Our comparison of RKN data and CADI ionosonde electric field measurements over Resolute Bay showed that periods of enhanced echo occurrence correlate with periods of enhanced electric field. This effect is of particular importance for the summer observations when the amount of radio wave absorption is significant and enhanced fluctuation amplitude of ionospheric irregularities (due to enhanced electric field) can provide a possibility to detect echoes.

6.3 Suggestions for future research

The work undertaken can be expanded in several directions:

1) The level of HF radio wave attenuation due to D-region collisional absorption is one of the crucial factors in getting signal returned from the ionosphere (e.g., *Danskin et al.*, 2002). This is especially true during periods of strong energetic particle precipitations. This issue has not been addressed in this thesis. One can estimate the HF radio wave attenuation by investigating riometer data at frequencies of >30 MHz. In the Canadian sector, the convenient arrangement would be Rankin Inlet and Taloyak (TALO) riometers for the Rankin Inlet radar. For the Saskatoon radar some data from Rabbit Lake can be considered. However, these data are largely raw records. For estimates of the absorption, they require de-spiking, base line computations and mass processing. Technically this is a feasible project. However, even if the data are processed, there would be additional concerns because the riometer location is not optimal; they are not underneath of the radar rays entry point into the D region. For the RKN radar the ranges are either 0 km (RKN) or 900 km (TALO) while for the SAS radar they are

$\sim$700 km. More convenient configuration would be Hankasalmi radar and Oulu-Rovaniemi riometers, Finland. The radar-riometers distances are $\sim$450 and 600 km, respectively.

2) Recently, the McMurdo radar started operation in Antarctica. The radar is located at high geomagnetic latitude of $\Lambda =$ -80°, so that it can easily detect echoes over the magnetic Pole. The radar indeed detects numerous echoes over the Pole. This implies that the F region at these large magnetic latitudes is filled with irregularities and the RKN radar simply cannot detect them because of propagation conditions. It is interesting that the RKN and MCM radar have "conjugate", partially overlapping FoVs (MCM monitors higher MLATs). Thus, conjugacy in echo occurrence for short-range MCM and far range RKN echoes can be investigated. One of possible reasons for yet to be discovered differences is the fact that the solar terminator line passes differently the FoVs of these radars.

3) The thesis gives an impression that electric field is a minor factor in echo detection; as long as one has some electric field of several mV/m, the echo can be detected. Since SuperDARN convection maps are available for many years, it would be interesting to find out trends in the electric field magnitude changes vs. solar cycle at various latitudes and whether this has some correlation with echo occurrence. The obtained in this thesis results imply that the amplitude of F-region echoes should not depend strongly on the $\boldsymbol{E} \times \boldsymbol{B}$ drift magnitude contrary to the case of E-region decameter irregularities (e.g., *Markarevitch et al.*, 2001; *Makarevitch*, 2003). It would be interesting to plot power of HF echoes vs. $\boldsymbol{E} \times \boldsymbol{B}$. Since RB ionosonde data are limited, one can consider RNK and INV joint data. Preliminary analysis supports the notion of independence but more extensive analysis is required. On the other hand, previous work indicated that number of echoes increases whenever the IMF B_z becomes negative (*Ballatore et al., 2001*). With B_z getting more negative, IMF reconnection conditions are getting more favorable and thus electric fields in the ionosphere are expected to be larger, overall. There is also some increase in a number of echoes prior to substorms when electric field is somewhat enhanced (*Wild and Gorocott*, 2008). One hardly can expect great changes in the propagation conditions. Why then we do have the effect? Again, one can think that electric fields are contributing factor. These two facts tell us that one cannot ignore electric fields as a factor controlling HF echo occurrence. This is in addition to our finding that the RKN summer echo occurrence correlates well with the electric field magnitudes. It well might be that the effect of

electric field is better recognizable for nighttime observations in quiet conditions when other factors are at reasonable and stable levels. It is then highly desirable to isolate such observations in the entire data base. Work with RISR-C incoherent scatter radar would be very interesting in this respect, especially in view that its FoV is towards the RKN and INV radars so that chances to receive common data sets are higher than the current configuration with the RISR-N radar.

4) Seasonal variation with equinoctial maxima seems to be a common feature of SuperDARN radar occurrence pattern. It occurs mostly because of "addition" of dawn-dusk echoes to regularly detection of midnight echoes or near noon echoes. One interesting question is how different is the effect for various radars of the network. The amount of refraction needed vary from one radar to another. If seasonal variation is simply propagation effect, one would expect certain differences between various radars of the network.

5) Another interesting question is why some beams have preference in terms of echo detection. Propagation conditions seem to be the major factor. Extensive computer modeling for various configurations might give some clues. Upcoming e-POP mission would be extremely useful to address this issue.

6) One of very unexpected results of this thesis is better (at least comparable) winter echo detection of the near noon-hour echoes with the auroral zone SAS radar (via 1½-hop propagation mode) as compared to the polar cap RKN radar (via ½-hop propagation mode). It is important to realize that the SAS ground scatter occurs roughly at latitudes on the RKN radar location so that radar rays for both systems propagate through the polar cap ionosphere (1/3 portion of SAS ray paths) along paths with very similar ionospheric conditions. We tried a hypothesis that some SAS echoes were misidentified ground scattered echoes and did not find support for this hypothesis. We do not see another way of addressing the issue, but we feel that resolving it would be an important step towards understanding the reasons for occurrence of coherent HF echoes.

REFERENCES

Baggaley, W. J. (1970), Backscatter observations of F-region field-aligned irregularities during I.Q.S.Y., *J. Geophys. Res.,* 75, 152-158.

Ballatore, P., J.-P. Villain, N. Vilmer, and M. Pick (2001), The influence of the interplanetary medium on SuperDARN radar scattering occurrence, *Ann. Geophys.,* 18, 1576-1583.

Bates, H. F. (1960), Direct HF backscatter from the F region, *J. Geophys. Res.,* 65, 1993-2002.

Bates, H. F., and P. R. Albee (1970), Aspect sensitivity of F-layer HF backscatter echoes, *J. Geophys. Res.,* 75, 165-170.

Baumjohann, W., and R. A. Treumann (1997), *Basic Space Plasma Physics*, Imperial College Press, London, UK.

Booker, H. G. (1956), A theory of scattering by nonisotropic irregularities with application to radar reflections from the aurora, *J. Atmos. Sol.-Terr. Phys.,* 8, 204-221.

Bristow, W. A., J. Spaleta, and R. T. Parris (2011), First observations of ionospheric irregularities and flows over thesouth geomagnetic pole from the Super Dual Auroral Radar Network (SuperDARN) HF radar at McMurdo Station, Antarctica, *J. Geophys. Res.,* 116, A12325, doi:10.1029/2011JA016834.

Cai, H. T., S. Y. Ma, Y. Fan, Y. C. Liu, and K. Schlegel (2007), Climatological features of electron density in the polar ionosphere from long-term observations of EISCAT/ESR radar, *Ann. Geophys.*, 25, 2561-2569.

Carter, B. A. (2011), HF radar observations of E-region plasma waves in the sub-auroral, auroral and polar regions, Ph.D Thesis, Latrobe University, Melbourne, Australia.

Carter, B. A., and R. A. Makarevich (2010), On the diurnal variation of the E-region coherent HF echo occurrence, *J. Atmos. Sol.-Terr. Phys.*, 72, 570-582.

Danskin, D. W. (2003), HF auroral backscatter from the E and F regions, Ph.D Thesis, University of Saskatchewan, Saskatoon, Canada.

Danskin, D. W., A. V. Koustov, T. Ogawa, S. Nozawa, N. Nishitani, S. Milan, M. Lester, and D. André (2002), On the factors controlling the occurrence of F-region coherent echoes, *Ann. Geophys.*, 20, 1399-1413.

Dungey, J. W. (1961), Interplanetary magnetic field and the auroral zones, *Phys. Res. Lett.,* 6, 47-49.

Fiori, R. A. D., A. V. Koustov, D. Boteler, and R. A. Makarevich (2009), PCN magnetic index and average convection velocity in the polar cap inferred from SuperDARN radar measurements, *J. Geophys. Res.*, 114, A07225, doi:10.1029/2008JA013964.

Fukumoto, M., N. Nishitani, T. Ogawa, N. Sato, H. Yamagishi, and A. S. Yukimatu (1999), Statistical analysis of echo power, Doppler velocity and spectral width obtained with the Syowa South HF radar, *Adv. Polar Upper Atmos. Res.*, 13, 37-47.

Fukumoto, M., N. Nishitani, T. Ogawa, N. Sato, H. Yamagishi, and A. S. Yukimatu (2000), Statistical study of Doppler velocity and echo power around 75° magnetic latitude with the Syowa East HF radar, *Adv. Polar Upper Atmos. Res.*, 14, 93-102.

Gondarenko, N. A., and P. N. Guzdar (2004), Plasma patch structuring by the nonlinear evolution of the gradient drift instability in the high-latitude ionosphere, *J. Geophys. Res.*, 109, A09301, doi:10.1029/2004JA010504.

Greenwald, R. A., K. B. Baker, J. R. Dudeney, M. Pinnock, T. B. Jones, E. C. Thomas, J.-P. Villain, J.-C.Cerisier, C. Senior, C. Hanuise, R. D. Hunsuker, G. Sofko, J. Koehler, E. Nielsen, R. Pellinen, A. D. M. Walker, N. Sato, and H. Yamagishi (1995), DARN/SUPERDARN, A global view of the dynamics of high-latitude convection, *Space Sci. Rev.*, 71, 761-796.

Greenwald, R. A., K. Oksavik, P. J. Erickson, F. D. Lind, J. M. Ruohoniemi, J. B. H. Baker, and J. W. Gjerloev (2006), Identification of the temperature gradient instability as the source of decameter-scale ionospheric irregularities on plasmapause field lines, *Geophys. Res. Lett.*, 33, L18105, doi:10.1029/2006GL026581.

Hargreaves, J. K. (1992), *The Solar-Terrestrial Environment*, Cambridge University Press, Cambridge, UK.

Hosokawa, K., and N. Nishitani (2010), Plasma irregularities in the dusksidesubauroral ionosphere as observed with midlatitude SuperDARN radar in Hokkaido, Japan, *Radio Sci.*, 45, RS4003, doi:10.1029/2009RS004244.

Hosokawa, K., T. Iyemori, A. S. Yukimatu, and N. Sato (2001), Source of field-aligned irregularities in the subauroral F region as observed by the SuperDARN radars, *J. Geophys. Res.*, 106, 24713–24731.

Hosokawa, K., M. Sugino, M. Lester, N. Sato, A. S. Yukimatu, and T. Iyemori (2002), Simultaneous measurement of dusksidesubauroral irregularities from the CUTLASS Finland radar and EISCAT UHF system, *J. Geophys. Res.*, 107, A12, 1457, doi:10.1029/2002JA009416.

Hower, G. L., D. M. Ranz, and C. L. Allison (1966), Comparison of HF radar echoes and high latitude spread-F measurements, *J. Geophys. Res.*, 71, 3215-3221.

Huber, M. (1999), HF radar echo statistics and spectral studies using SuperDARN, M.Sc. Thesis, University of Saskatchewan, Saskatoon, Canada.

Hunsucker, R. D., J. K. Hargreaves (2003), *The High-Latitude Ionosphere and its effects on Radio Propagation*, Cambridge University Press, Cambridge, UK.

Jayachandran, P. T., R. B. Langley, J. W. MacDougall, S. C. Mushini, D. Pokhotelov, A. M. Hamza, I. R. Mann, D. K. Milling, Z. C. Kale, R. Chadwick, T. Kelly, D. W. Danskin, and C. S. Carrano (2009), The Canadian high arctic ionospheric network (CHAIN), *Radio Sci.*, 44, RS0A03, doi:10.1029/2008RS004046.

Kelley, M. C. (1989), *The Earth's Ionosphere: Plasma Physics and Electrodynamics*, Academic Press, San Diego, California, US.

Kelley, M. C., F. S. Mozer (1973), Electric field and plasma density oscillations due to the high frequency Hall current two stream instability in the auroral E region, *J. Geophys. Res.*, 78, 13, 2214-2221.

Keskinen, M. J., Ossakow, S. L. (1983), Nonlinear evolution of convecting plasma enhancements in the auroral ionosphere, 2. small scale irregularities, *J. Geophys. Res.,* 88, A1, 474-482.

Kivelson, M. G., and C. T. Russell (1995), *Introduction to Space Physics*, Cambridge University Press, Cambridge, UK.

Koustov, A. V., N. Nishitani, Y. Ebihara, T. Kikuchi, M. R. Hairston, and D. André (2008b), Subauroral polarization streams: Observations with the Hokkaido and King Salmon SuperDARN radars and modeling, *Ann. Geophys.*, 26, 3317–3327.

Koustov, A. V., G. J. Sofko, D. André, D. W. Danskin, and L. V. Benkevitch (2004), Seasonal variation of HF radar F region echo occurrence in the midnight sector, *J. Geophys. Res.*, 109, A06305, doi:10.1029/2003JA010337.

Koustov, A. V., R. A. Drayton, R. A. Makarevich, K. A. McWilliams, J.-P. St.-Maurice, T. Kikuchi, and H. U. Frey (2006), Observations of high-velocity SAPS-like flows with the King Salmon SuperDARN radar, *Ann. Geophys.*, 24, 1591-1608.

Kumar, V. V., R. A. Makarevich, T. A. Kane, H. Ye, J. C. Devlin, and P. L. Dyson (2011), On the spatiotemporal evolution of the ionospheric backscatter during magnetically disturbed periods as observed by the TIGER Bruny Island HF radar, *J. Atmos. Sol.-Terr. Phys.*, 73, 1940-1952.

Liu, H. (2010), Study of the high-latitude ionosphere with the Rankin Inlet PolarDARN radar, M.Sc. Thesis, University of Saskatchewan, Saskatoon, Canada.

Makarevitch, R. A. (2003), Formation of small-scale irregularities in the auroral E region, Ph.D Thesis, University of Saskatchewan, Saskatoon, Canada.

Makarevitch, R. A., T. Ogawa, K. Igarashi, A. V. Koustov, N. Sato, K. Ohtaka , H. Yamagishi, and A. Yukimatu (2001), On the power-velocity relationship for 12- and 50-MHz auroral coherent echoes, *J. Geophys. Res.*, 106, 15455-15469.

Makarevich, R. A., A. V. Koustov, K. Igarashi, N. Sato, T. Ogawa, K. Ohtaka, H. Yamagishi, and A. S. Yukimatu (2002), Comparison of flow angle variations of E-region echo characteristics at VHF and HF, *Adv. Polar Upper Atm. Res.*, 16, 59-83.

Makarevich, R. A. (2010), On the occurrence of high-velocity E-region echoes in SuperDARN observations, *J. Geophys. Res.*, 115, A07302, doi:10.1029/2009JA014698.

Makarevich, R. A., F. Honary, V. S. C. Howells, A. V. Koustov, P. Janhunen, S. E. Milan, J. A. Davies, A. Senior, I. W. McCrea, A. Viljanen (2006), A first comparison of irregularity and ion drift velocity measurements in the E region, *Ann. Geophys*., 24, 2375-2389.

Milan, S. E., T. K. Yeoman, M. Lester, E.C. Thomas, and T. B. Jones (1997), Initial backscatter occurrence statistics for the CUTLASS HF radars, *Ann. Geophys.*, 15, 703-718.

Milan, S. E., J. A. Davies, and M. Lester (1999), Coherent HF radar backscatter characteristics associated with auroral forms identified by incoherent radar techniques: A comparison of CUTLASS and EISCAT observations, *J. Geophys. Res.*,104, 22591-22604.

Möller, N. G. (1974), Backscatter results from Lindau-II. The movement of curtains of intense irregularities in the polar F-layer, *J. Atmos. Terr. Phys.*, 38, 1487-1501.

Ogawa, T., H. Mori, and S. Miyasaki (1976), Rocket observations of electron density irregularities in the Antarctic auroral E region, *J. Geophys. Res.*, 81, 22, 4013-4015.

Parker, E. N. (1958), Dynamics of the interplanetary gas and magnetic fields, *Astrophys. J.*, 128, 664-676.

Parkinson, M. L., J. C. Devlin, H. Ye, C. J. Waters, P. L. Dyson, A. M. Breed, and R. J. Morris (2003), On the occurrence and motion of decameter-scale irregularities in the sub-auroral, auroral, and polar cap ionosphere, *Ann. Geophys.*, 21, 1847-1868.

Peterson, A. M., O. G. Villard, Jr., R. L. Leadabrand, and P. B. Gallagher (1955), Regularly observable aspect-sensitive radio reflections from ionization aligned with the earth's magnetic field and located within the ionospheric layers at middle latitudes, *J. Geophys. Res.*, 60, 497-512.

Ponomarenko, P. V., J.-P. St. Maurice, G. C. Hussey, and A. V. Koustov (2010), HF ground scatter from the polar cap: Ionospheric propagation and ground surface effects, *J. Geophys. Res.*, 115, A10310, doi:10.1029/2010JA015828.

Ponomarenko, P. V., A. V. Koustov, J.-P. St.-Maurice, and J. Wiid (2011), Monitoring the F-region peak electron density using HF backscatter interferometry, *Geophys. Res. Lett.*, 38, L21102, doi:10.1029/2011GL049675.

Ponomarenko, P. V., J.-P. St-Maurice, C. L.Waters, R. G. Gillies, and A. V. Koustov (2009), Refractive index effects on the scatter volume location and Doppler velocity estimates of ionospheric HF backscatter echoes, *Ann. Geophys.*, 27, 4207-4219.

Prikryl, P., P. T. Jayachandran, S. C. Mushini, D. Pokhotelov, J.W. MacDougall, E. Donovan, E. Spanswick, and J.-P. St.-Maurice (2010), GPS TEC, scintillation and cycle slips observed at high latitudes during solar minimum, *Ann. Geophys.*, 28, 1307-1316.

Ruohoniemi, M., and K. B. Baker (1998), Large-scale imaging of high-latitude convection with Super Dual Auroral Radar Network HF radar observations, *J. Geophys. Res.*, 103, 20797-20811.

Ruohoniemi, J. M., and R. A. Greenwald (1997), Rates of scattering occurrence in routine HF radar observations during solar cycle maximum, *Radio Sci.*, 32, 1051-1070.

Ruohoniemi, J. M., R. A. Greenwald, J.-P. Villain, K. B. Baker, P. T. Newell, and C.-I. Meng (1988), Coherent HF radar backscatter from small-scale irregularities in the dusk sector of the subauroral ionosphere, *J. Geophys. Res.*, 93, 12871-12882.

Schiffler, A. (1996), SuperDARN measurements of double-peaked velocity spectra, M.Sc. Thesis, University of Saskatchewan, Saskatoon, Canada.

Schlegel, K. (1992), Measurements of electron density fluctuations during the ROSE rocket flights, *J. Atmos. Terr. Phys.*, 54, 715-723.

Schunk, R. W., and A. F. Nagy (2000), *Ionospheres: Physics, Plasma Physics, and Chemistry*, Cambridge University Press, Cambridge, UK.

Tsunoda, R. T. (1988), High latitude irregularities: A review and synthesis, *Rev. Geophys.*, 26, 719-760.

Turunen, T., and J. Oksman, On the relative location of the plasmapause and the HF backscatter curtains, *J. Atmos. Terr. Phys.*, 41, 345-350.

Uspensky, M. V., A. V. Kustov, E. Nielsen, A. Huskonen, and J. Kangas (1988), Estimates of electron density in the auroral E region based on STARE data. *Geomagn. Aeron.*, 28, 589-591.

Uspensky, M. V., A. V. Kustov, G. J. Sofko, J. A. Koehler, J. P. Villain, C. Hanuise, J. M. Ruohoniemi, and P. J. S. Williams (1994), Ionospheric refraction effects in slant range profiles of auroral HF coherent echoes, *Radio Sci.*, 29, 503-517, doi:10.1029/93RS03256.

Uspensky, M. V., A. V. Koustov, P. Eglitis, A. Huuskonen, S. E. Milan, T. Pulkkinen, and R. Pirjola (2001), CUTLASS HF radar observations of high-velocity E-region echoes, *Ann. Geophys.*, 19,411-424.

Vickrey, J. F., and J. D. Kelley (1982), The effects of a conducting E layer on classical F region cross-field plasma diffusion, *J. Geophys. Res.*, 87, 4461-4468.

Villain, J. P., R. A. Greenwald, K. B. Baker, and J. M. Ruohoniemi (1987), HF radar observations of E region plasma irregularities produced by oblique electron streaming, *J. Geophys. Res.*, 92, 12,327-12,342.

Villain, J. P., R. Andre, C. Hanuise, and D. Gresillon (1996), Observations of the high-latitude ionosphere by HF radars: Interpretation in terms of collective wave scattering and characterization of turbulence, *J. Atmos. Terr. Phys.*, 58, 943-958.

Walker, A. D. M., R. A. Greenwald, and K. B. Baker (1987), Determination of the fluctuation level of ionospheric irregularities from radar backscatter measurements*,* *Radio Sci.*, 22, 689-705.

Weaver, P. F. (1965), Backscatter echoes from field-aligned irregularities in the F region, *J. Geophys. Res.*, 70, 5425-5432.

Wild, J. A., and A. Grocott (2008), The influence of magnetospheric substorms on SuperDARN radar backscatter, *J. Geophys. Res.*, 113, A04308, doi:10.1029/2007JA012910.

Williams, P. J. S., B. Jones, A. V. Koustov, and M. V. Uspensky (1999), The relationship between E-region electron density and the power of auroral coherent echoes at 45 MHz, *Radio Sci.*, 34, 449-457.